




## Nuclear Physics Mid Term Plan at LNGS

R. Buompane<sup>1,2</sup>, F. Cavanna<sup>3</sup>, C. Curceanu<sup>4,5</sup>, A. D'Onofrio<sup>1,2</sup>, A. Di Leva<sup>2,6,a</sup> , A. Formicola<sup>7,b</sup>, L. Gialanella<sup>1,2</sup>, C. Gustavino<sup>7</sup>, G. Imbriani<sup>2,6</sup>, M. Junker<sup>8</sup>, A. Marciano<sup>4,9</sup>, F. Marzaioli<sup>1,2</sup>, R. Nania<sup>10</sup>, F. Napolitano<sup>4</sup>, K. Piscicchia<sup>4,11</sup>, O. Straniero<sup>7,12</sup>, C. Abia<sup>13</sup>, M. Aliotta<sup>14</sup>, D. Bemmerer<sup>15</sup>, A. Best<sup>2,6</sup>, A. Boeltzig<sup>15</sup>, C. Bruno<sup>14</sup>, A. Cacioli<sup>16,17</sup>, A. Chieffi<sup>18</sup>, G. Ciani<sup>19,20</sup>, G. D'Agata<sup>21</sup>, R. J. deBoer<sup>22</sup>, M. De Cesare<sup>2,23</sup>, D. Dell'Aquila<sup>2,6</sup>, R. Depalo<sup>24,25</sup>, I. Dominguez<sup>13</sup>, F. Ferraro<sup>8</sup>, J. Garcia Duarte<sup>26</sup>, A. Guglielmetti<sup>24,25</sup>, Gy. Gyürky<sup>27</sup>, S. Hayakawa<sup>28</sup>, M. La Cognata<sup>21</sup>, L. Lamia<sup>21,29</sup>, L. E. Marcucci<sup>30,31</sup>, E. Masha<sup>15</sup>, M. Mazzocco<sup>16,17</sup>, E. L. Morales-Gallegos<sup>1,2</sup>, S. Palmerini<sup>32,33</sup>, I. Passariello<sup>1,2</sup>, A. Petraglia<sup>1</sup>, D. Piatti<sup>16,17</sup>, M. Pignatari<sup>34,35</sup>, R. G. Pizzone<sup>21,29</sup>, G. Porzio<sup>1,2</sup>, D. Rapagnani<sup>2,6</sup>, G. G. Rapisarda<sup>21,29</sup>, S. Romano<sup>21,29,36</sup>, M. Rubino<sup>1,2</sup>, C. Santonastaso<sup>1,2</sup>, M. L. Sergi<sup>21,29</sup>, J. Skowronski<sup>16,17</sup>, R. Sparta<sup>21,37</sup>, F. Terrasi<sup>1</sup>, A. Tumino<sup>21,37</sup>, S. Turkat<sup>15</sup>, M. Wiescher<sup>22</sup>, S. Zavatarelli<sup>38,39</sup>

- <sup>1</sup> Dipartimento di Matematica e Fisica, Università della Campania "L. Vanvitelli", 81100 Caserta, Italy
- <sup>2</sup> Sezione di Napoli, Istituto Nazionale di Fisica Nucleare, 80126 Naples, Italy
- <sup>3</sup> Sezione di Torino, Istituto Nazionale di Fisica Nucleare, 10125 Turin, Italy
- <sup>4</sup> Laboratori Nazionali di Frascati, Istituto Nazionale di Fisica Nucleare, 00044 Frascati, Italy
- <sup>5</sup> Institutul National pentru Fizica si Inginerie Nucleara "Horia Hulubei", 077125 Bucharest-Magurele, Romania
- <sup>6</sup> Dipartimento di Fisica "E. Pancini", Università di Napoli "Federico II", 80126 Naples, Italy
- <sup>7</sup> Sezione di Roma, Istituto Nazionale di Fisica Nucleare, 00185 Roma, Italy
- <sup>8</sup> Laboratori Nazionali del Gran Sasso, Istituto Nazionale di Fisica Nucleare, 67100 Assergi L'Aquila, Italy
- <sup>9</sup> Department of Physics (Jiangwan Campus), Fudan University, 200438 Shanghai, China
- <sup>10</sup> Sezione di Bologna, Istituto Nazionale di Fisica Nucleare, 40127 Bologna, Italy
- <sup>11</sup> Museo Storico della Fisica e Centro Studi e Ricerche "Enrico Fermi", Centro Ricerche Enrico Fermi, 00184 Roma, Italy
- <sup>12</sup> Osservatorio Astronomico d'Abruzzo, Istituto Nazionale di Astrofisica, 64100 Teramo, Italy
- <sup>13</sup> Dpto. Física Teórica y del Cosmos, Universidad de Granada, 18071 Granada, Spain
- <sup>14</sup> School of Physics and Astronomy, University of Edinburgh, Edinburgh, UK
- <sup>15</sup> Helmholtz-Zentrum Dresden-Rossendorf, D-01328 Dresden, Germany
- <sup>16</sup> Dipartimento di Fisica e Astronomia, Università degli Studi di Padova, 35131 Padua, Italy
- <sup>17</sup> Sezione di Padova, Istituto Nazionale di Fisica Nucleare, 35131 Padua, Italy
- <sup>18</sup> Osservatorio Astronomico di Roma, Istituto Nazionale di Astrofisica, 00078 Monte Porzio Catone, Italy
- <sup>19</sup> Dipartimento di Fisica "M. Merlin", Università degli Studi di Bari, 70125 Bari, Italy
- <sup>20</sup> Sezione di Bari, Istituto Nazionale di Fisica Nucleare, 70125 Bari, Italy
- <sup>21</sup> Laboratori Nazionali del Sud, Istituto Nazionale di Fisica Nucleare, 95123 Catania, Italy
- <sup>22</sup> Department of Physics and the Joint Institute for Nuclear Astrophysics, University of Notre Dame, Notre Dame, IN 46556, USA
- <sup>23</sup> Centro Italiano di Ricerche Aerospaziali, 81043 Capua, Italy
- <sup>24</sup> Dipartimento di Fisica, Università degli Studi di Milano, 20133 Milan, Italy
- <sup>25</sup> Sezione di Milano, Istituto Nazionale di Fisica Nucleare, 20133 Milan, Italy
- <sup>26</sup> Nuclear and Particle Physics Group, Lawrence Livermore National Laboratory, Livermore, CA 94550, USA
- <sup>27</sup> Institute for Nuclear Research (ATOMKI), H-4001 Debrecen, Hungary
- <sup>28</sup> RIKEN Campus, Center for Nuclear Study, University of Tokyo, Wakō, Saitama 351-0198, Japan
- <sup>29</sup> Dipartimento di Fisica e Astronomia "E. Majorana", Università degli Studi di Catania, 95123 Catania, Italy
- <sup>30</sup> Dipartimento di Fisica, Università degli Studi di Pisa, 56127 Pisa, Italy
- <sup>31</sup> Sezione di Pisa, Istituto Nazionale di Fisica Nucleare, 56127 Pisa, Italy
- <sup>32</sup> Dipartimento di Fisica e Geologia, Università degli Studi di Perugia, 06123 Perugia, Italy
- <sup>33</sup> Sezione di Perugia, Istituto Nazionale di Fisica Nucleare, 06123 Perugia, Italy
- <sup>34</sup> Konkoly Observatory, H-1121 Budapest, Hungary
- <sup>35</sup> E. A. Milne Centre for Astrophysics, University of Hull, Hull HU6 7RX, UK
- <sup>36</sup> Facoltà di Ingegneria e Architettura, Università degli Studi di Enna "Kore", 94100 Enna, Italy
- <sup>37</sup> Centro Siciliano di Fisica Nucleare e Struttura della Materia, 95123 Catania, Italy
- <sup>38</sup> Sezione di Genova, Istituto Nazionale di Fisica Nucleare, 16146 genoa, Italy
- <sup>39</sup> Dipartimento di Fisica, Università degli Studi di Genova, 16146 genoa, Italy

Received: 31 October 2023 / Accepted: 26 December 2023  
© The Author(s) 2024

**Abstract** The Istituto Nazionale di Fisica Nucleare—Laboratori Nazionali del Gran Sasso (LNGS) is one of the largest underground physics laboratory, a very peculiar environment suited for experiments in Astroparticle Physics, Nuclear Physics and Fundamental

<sup>a</sup> e-mail: [antonino.dileva@unina.it](mailto:antonino.dileva@unina.it) (corresponding author)

<sup>b</sup> e-mail: [alba.formicola@roma1.infn.it](mailto:alba.formicola@roma1.infn.it) (corresponding author)

Symmetries. The newly established Bellotti Ion Beam facility represents a major advance in the possibilities of studying nuclear processes in an underground environment. A workshop was organized at LNGS in the framework of the Nuclear Physics Mid Term Plan in Italy, an initiative of the Nuclear Physics Division of the Istituto Nazionale di Fisica Nucleare to discuss the opportunities that will be possible to study in the near future by employing state-of-the-art detection systems. In this report, a detailed discussion of the outcome of the workshop is presented.

### List of symbols

$L_{\odot}$	Solar luminosity
$M_{\odot}$	Solar mass
AGB	Asymptotic giant branch
AMS	Accelerator mass spectrometry
BEGe	Broad Energy Germanium Detector
BBN	Big Bang Nucleosynthesis
CNN	Convolutional neural network
CNO	Carbon–nitrogen–oxygen
CSL	Continuous spontaneous localization
DD	Direct decay
DP	Diósi–Penrose
DSSSD	Double-sided silicon strip detector
EC	Electron capture
ERDA	Elastic recoil detection analysis
HPGe	High-purity germanium detector
IBA	Ion beam analysis
LUNA	Laboratory underground for nuclear astrophysics
MC-ICP-MS	Multicollector inductively coupled plasma mass spectrometry
MGS	Messiah–Greenberg superselection
NCQG	Non-commutative quantum gravity
NME	Nuclear matrix element
NRA	Nuclear reaction analysis
PEP	Pauli exclusion principle
PSD	Pulse shape discrimination
QM	Quantum mechanics
RBS	Rutherford backscattering
RI	Radioactive ion
RMS	Recoil mass separator
SD	Sequential decay
SDD	Silicon drift detectors
SF-ICP-MS	Sector field inductively coupled plasma mass spectrometry
SIRMS	Stable isotope ratio mass spectrometry
SM	Standard model
SN	Supernova
SPE	Solar proton events
SSD	Silicon strip detector
THM	Trojan Horse method
TIMS	Thermal ionization mass spectrometry
TP	Thermal pulse
TPS	Thermal protection system

### 1 Executive summary

The Laboratori Nazionali del Gran Sasso (LNGS) of the Istituto Nazionale di Fisica Nucleare (INFN) is one of the largest underground physics laboratory devoted to fundamental research programs in Astroparticle Physics, Nuclear Physics and Fundamental Symmetries [1]. The rock overburden (3800 m of water equivalent) makes the LNGS a very peculiar environment suited for the study of “rare” processes. The reduction of the cosmic ray flux is of great advantage for measurements where background suppression plays a

crucial role [2–4]. At present LNGS hosts activities in Fundamental Symmetries and Nuclear Astrophysics, funded and supervised by the Nuclear Physics Division (CSN3) of INFN.

Among other laboratories having tight connections with LNGS, there is the Center for Isotopic Research on Cultural and Environmental heritage (CIRCE) of the Department of Mathematics and Physics, University of Campania, Caserta, Italy [5], where a wide range of applied nuclear physics and interdisciplinary activities are routinely conducted, together with INFN-CSN3-related researches mainly in nuclear astrophysics.

In the framework of CSN3 scientific activities, there were already a few occasions to put together the large variety of expertises present and are summarized in [6, 7]. Following these successful initiatives, the Nuclear Physics Mid Term Plan in Italy [8] was organized by the CSN3 to allow the experimental and theoretical nuclear physics community to meet and plan a scientific vision for the near future in Italy, as presented in the introductory paper of this Focus issue [9].

As for the Laboratori Nazionali di Legnaro (LNL) [10] and Laboratori Nazionali del Sud (LNS) [11], and later the Laboratori Nazionali di Frascati (LNF) [12], the LNGS Session [13] has given the occasion to survey the opportunities that the community gathering around the INFN-CSN3 funded projects can exploit in the next years. It also aims at strengthening and exploring further synergies between LNGS and other laboratories.

### 1.1 Fundamental symmetries

The fundamental symmetries play a crucial role in quantum mechanics (QM), arising from very few, general assumptions, and are incorporated directly in the theoretical framework of the Standard Model (SM). In this context, high-precision experiments testing theories and models beyond the standard QM and SM may pave the road toward a new theory, where the open questions may be fully clarified.

At LNGS, fundamental symmetries and their relation to QM and SM are investigated from different directions and perspectives within the VIP Collaboration, searching for possible violations of the Pauli Exclusion Principle (PEP), deeply connected to CPT and Lorentz symmetry, but also quantum gravity.

As midterm plan, from a theoretical standpoint, a series of activities are foreseen, aiming to connect, and cross-fertilize various developments in non-commutative quantum gravity (NCQG), leading to the PEP violations. In this context, we also plan to seek new phenomenological connections between the quantization schemes of NCQG and the wave function collapse and investigate their experimental signatures. The experimental activity is divided in Open Systems (where a new state is introduced from outside) and Closed Systems (where the state was already present) experiments. In the former, the VIP-2 apparatus, currently in operation for direct searches of PEP-violating atomic transitions, will be upgraded in the upcoming years, with focus on new, more efficient detectors and targets, and optimizations of the critical setup parameters to increase the sensitivity. In the latter, a dedicated data taking using a Broad Energy Germanium (BEGe) Detector will investigate new aspects and effects in PEP violation predicted by quantum gravity, such as signal anisotropy, and to explore the connection with CPT and Lorentz symmetries. Finally, we plan to develop and run new dedicated apparatuses based on germanium detectors, to search for the patterns of the spontaneous radiation predicted by refined dissipative and non-Markovian collapse models and study their interplay with gravity.

### 1.2 Direct measurements for nuclear astrophysics

Since more than three decades, accelerators are in use in the underground halls of LNGS. After the pioneering measurements with the 50 kV accelerator [14], in 2000 the LUNA 400 kV accelerator was installed and it is still in operation. More recently with the installation of the 3.5 MV accelerator of the Bellotti Ion Beam Facility (BIBF) started its operation. The availability of these two accelerators provides great opportunities for the direct measurements of nuclear reactions of astrophysical interest, possibly directly reaching the energies corresponding to stellar environments. The most compelling cases will be presented in Sect. 4.1. The experimental opportunities envisioned at LNGS and CIRCE will be thoroughly discussed in Sect. 4.2. A summary, including the needed main upgrades and a gross estimate of the time to deployment, is given in Tables 1 and 2 for LNGS and CIRCE, respectively.

### 1.3 Applied nuclear physics

The development of nuclear astrophysics experiments at CIRCE has led to a fruitful interchange between basic and applied research activities. Indeed, conventional and accelerator-based mass spectrometry has been used for studies processes of astrophysical interest by means of isotopic ratio measurements in terrestrial as well as in meteoritic materials. Similarly, some technical developments needed in nuclear physics experiments, especially in ion beam production, detectors and related equipment, have led to applications in various fields. The very intense  ${}^7\text{Be}$  beam developed for the measurement of the  ${}^7\text{Be}(p, \gamma){}^8\text{B}$  cross section is now used in wear studies of materials for several applications, including aerospace. Mass spectrometry and other ion beam analysis techniques are routinely applied for the characterization of materials used in detector development, among which the water diffusion and related micro-leaks in the KM3NeT deep-sea neutrino telescope equipment were studied.

## 2 Introduction

The Laboratori Nazionali del Gran Sasso (LNGS) of the Istituto Nazionale di Fisica Nucleare (INFN) is one of the largest underground physics laboratory devoted to fundamental research programs in Astroparticle Physics, Nuclear Physics and Fundamental Symmetries [1]. At present, among activities funded and supervised by INFN-CSN3, LNGS hosts experiments in Fundamental Symmetries and Nuclear Astrophysics.

Therefore, the Nuclear Physics Mid Term Plan in Italy—LNGS Session [13] was the opportunity to discuss the present and near future prospects in these two main activities, with an outlook going beyond the state of the art.

In the context of Fundamental Symmetries, a consolidated experimental activity, the Violation of Pauli exclusion principle (VIP) and VIP-2 experiments, aims at improving the limit on the probability of violation of the Pauli Exclusion Principle (PEP) and in parallel conducts high-sensitivity tests of quantum collapse models of the wave function.

LNGS has been for a long time a unique infrastructure hosting an accelerator devoted to Nuclear Astrophysics, the Laboratory for Underground Nuclear Astrophysics (LUNA). The LUNA 400 kV accelerator, in almost two decades, produced a wealth of high-precision cross sections, that significantly advanced our knowledge on nuclear processes occurring inside stars and other astrophysical objects. A new 3.5 MV accelerator, the Bellotti Ion Beam Facility (BIBF), has been recently installed, that is able to deliver very intense proton, helium and carbon beams. It is for the Nuclear Astrophysics community the opportunity to extend the measurements to elusive reactions occurring in advanced stellar burning stages and offers to a wider Nuclear Physics community a potential to be identified and exploited.

Underground measurements are often complemented with overground measurements, either to extend the energy range, for ancillary measurements or specific R & D tailored toward the low-activity environment. Among other laboratories having tight connections with LNGS, there is the Center for Isotopic Research on Cultural and Environmental heritage (CIRCE), of the Department of Mathematics and Physics, University of Campania, Caserta, Italy, where the European Recoil separator for Nuclear Astrophysics (ERNA) is located, and hosts also other INFN-CSN3-related research [5].

### 2.1 LNGS

The rock overburden (3800 m of water equivalent) makes the LNGS a very peculiar environment suited for the study of “rare” processes. The reduction of the cosmic ray flux is of great advantage for measurements where background suppression plays a crucial role [3, 4, 15].

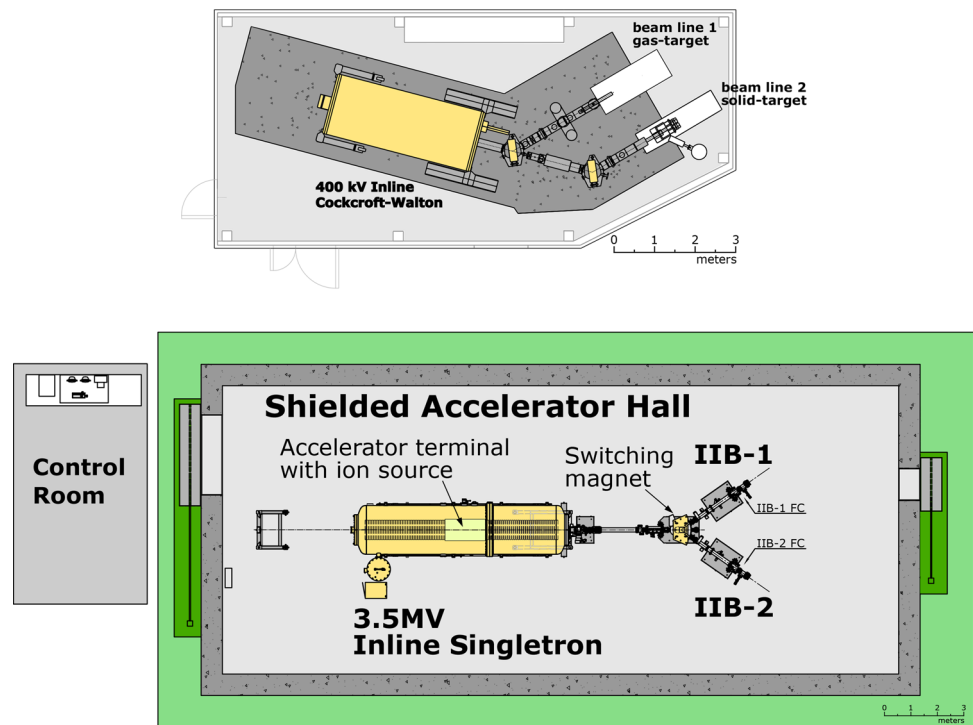
Direct cross section measurements typically require accelerators providing high-intensity beams, ultra-pure stable targets and the highest possible detection efficiency. Moreover, when approaching the astrophysically relevant energy range, the counting rate from a nuclear fusion reaction signal may become much smaller than the environmental background produced by cosmic radiation and naturally occurring radioactive elements. To overcome this problem, the Laboratory for Underground Nuclear Astrophysics (LUNA) was built at LNGS in the early 90’s, hosting a 400 kV Inline-Cockcroft-Walton electrostatic accelerator produced by High Voltage Engineering Europa (HVEE); see Fig. 1 top panel. The accelerator has a HV-ripple of 30 Vpp and a reproducibility as well as long-term stability of the HV of 20 Vpp at 400 kV over several days. The radiofrequency ion source—mounted directly on the accelerator tube—provides ion beams of 1 mA hydrogen (75% H<sup>+</sup>) and 500  $\mu$ A He<sup>+</sup> over a continuous operating time of about 40 days [16]. Alternatively, the ion beam can be guided through the 0° port of the magnet, going to the first beam line equipped with a gas target, and a second 45° magnet (identical to the first magnet) into an additional beam line with a solid target station. Thanks to this accelerator, several crucial reactions for hydrogen, helium burning and Big Bang Nucleosynthesis were studied.

The LNGS has recently established the “Bellotti Ion Beam Facility” by building a new infrastructure in Hall B to host a 3.5 MV Singletron machine designed and built by HVEE [17]. This was possible also through a special funding of the Italian Ministry of Research (Progetto Premiale “LUNAMV”) awarded to the LUNA Collaboration. The accelerator is equipped with two independent beam lines (see Fig. 1 bottom panel) and can deliver proton, helium and carbon beams with maximum intensity of 1, 0.5 and 0.15 mA, respectively. The start of scientific exploitation is foreseen by second half of 2023.

#### 2.1.1 Resident instrumentation for nuclear physics

- VIP-2 detector [18]: based on the experience of the VIP experiment, the apparatus makes use of cutting edge radiation silicon drift detectors (SDDs) developed in collaboration with the Stefan Meyer Institute (SMI) of the Austrian Academy of Sciences, Politecnico di Milano and the Fondazione Bruno Kessler. The SDDs are employed as ideal X-ray detectors due to their excellent spectroscopic response and high resolution of approximately 190 eV (FWHM) at 8 keV. The SDD cells possess large geometrical acceptance, an overall active area of 0.64 cm<sup>2</sup>, a thickness of 450  $\mu$ m and an efficiency of 99% at 8 keV, surpassing charge coupled devices used in VIP. The experiment setup includes a copper target consisting of copper strips for direct current circulation, with each strip measuring 71 mm in length, 20 mm in height and 25  $\mu$ m in thickness, where a direct current up to 180 A can be circulated. To maintain a low temperature, a cooling pad is placed between the strips and a closed chiller circuit is employed. Two parallel arrays of SDD cells, each containing 2  $\times$  4 cells, are positioned on both sides of the copper strips and operated at – 90 °C. The vacuum chamber, maintained at a pressure of 10<sup>–5</sup> mbar, houses the detectors, their front-end electronics and an

**Fig. 1** Layout of the LUNA 400 kV (top) and the 3.5 MV Inline Singletron (bottom) accelerators installed at the Laboratori Nazionali del Gran Sasso (drawings have different scales)



in situ calibration  $^{55}\text{Fe}$  radioactive source. Externally, a passive shield composed of copper and lead bricks provides additional protection against the residual environmental radiation present in the laboratory halls.

- **Solid target:** vacuum chambers with different geometries are available to host different solid targets or serve different purposes. Immediately prior to entering the target chamber, the beam passes through a liquid nitrogen ( $\text{LN}_2$ )-cooled copper tube that serves to reduce rest gas contaminants and prevents the build-up of carbon on the target surface. The target flange is isolated from all other beam line components and acts as a Faraday cup to determine the total charge accumulated in the course of a measurement. The electron suppression is provided by a negative voltage applied to the copper tube. The target is typically water-cooled with de/ionized water.

In addition, the target preparation laboratory is equipped with an apparatus to produce solid oxygen targets by anodic oxidation of tantalum backings in isotopically enriched water, a technique known to produce targets with highly uniform stoichiometry and homogeneous thicknesses [19].

- **Windowless gas target [20]:** the LUNA 400 kV accelerator is also equipped with a windowless gas target. The use of a gas target provides the advantage of isotopical purity and high stability over prolonged periods. The differentially pumped gas target consists of three pumping stages and the interaction chamber, separated from each other with flux collimators which also serve as beam collimators. The sequence of pumping stages generates a pressure gradient from  $10^{-6}$  mbar, the typical accelerator tube pressure, to the interaction chamber pressure in the order of a few mbar. The pumping system is remotely controlled through a LabVIEW program. The gas coming out from the first and the second pumping stages can be collected and sent to an industrial purifier (MonoTorr II) to be cleaned and then recirculated. The target pressure is kept stable with an automated system controlling the inlet flux, using an active feedback from the pressure reading. Several gases have been used as targets, e.g., D,  $^3\text{He}$ , N, Ne. The beam stop in the interaction chamber serves as a calorimeter to measure beam intensity.
- **HPGe detectors:** high-purity germanium (HPGe) detectors are used by the VIP collaboration for studies on the foundations of quantum mechanics [21]. The experimental setup consisted of a coaxial p-type high-purity germanium detector surrounded by a complex shielding structure, with the outer part made of pure lead and the inner part made of electrolytic copper. The germanium crystal is characterized by a diameter of 8.0 cm and a length of 8.0 cm, with an inactive layer of 0.075 mm of lithium-doped germanium all around the crystal. The active germanium volume of the detector is  $375 \text{ cm}^3$ . The outer part of the passive shielding of the high-purity germanium detector consists of lead (30 cm from the bottom and 25 cm from the sides). The inner layer of the shielding (5 cm) is composed of electrolytic copper. The sample chamber has a volume of about 15 l ( $250 \text{ mm} \times 250 \text{ mm} \times 240 \text{ mm}$ ). The shield together with the cryostat is enclosed in an air-tight steel housing of 1 mm thickness, which is continuously flushed with boil-off nitrogen from a liquid nitrogen storage tank, in order to reduce the contact with external air (and thus radon) to a minimum. Additionally, the VIP-GATOR collaboration employs the Gator [22] facility and its 2.2 kg HPGe with 100.5% relative efficiency<sup>1</sup> in the context of searches for PEP-violating transitions at higher Z target materials.

<sup>1</sup> The efficiency of HPGe detectors is usually reported relative to the efficiency of a  $3 \times 3$  NaI scintillator at 25 cm source to detector distance.

The LUNA Collaboration utilizes four ultra-low-background HPGe detectors mainly for prompt  $\gamma$ -ray measurements. Relative efficiencies range from 90% to 140%. An electromechanical cooling system is available and can be used with two of the smaller detectors, in order to avoid the use, and periodic filling, of LN<sub>2</sub> and also to exploit more compact measurement setup configurations. The detectors can be coupled with various massive lead shielding described below.

- A segmented and highly efficient BGO detector [23, 24]: it is made of an array of six prismatic crystals, each 28 cm long arranged around a cylindrical borehole of 6 cm diameter each covering an azimuthal angle of 60°. The radial thickness of the segments is at least 7 cm. The crystals are optically insulated and coupled to Hamamatsu R1847-07 photomultipliers (PMTs). The target chamber fit in the central borehole and for the solid target at the center of the detector, a close to  $4\pi$  solid angle coverage is achieved. The detector features an energy resolution of about 11% FWHM at 1.33 MeV.
- Neutron detectors [25]: at LUNA a detector array containing eighteen <sup>3</sup>He filled proportional counters with stainless steel housing is available. The <sup>3</sup>He tubes are embedded in a high-density polyethylene (PE) for neutron moderation. The counters are arranged in two concentric rings around the target chamber: twelve counters of 40 cm active length are located at a radius of 11 cm, and six counters of 25 cm active length are located at 6 cm radius. This configuration allows for a nearly  $4\pi$  solid angle coverage around the target.
- Massive shielding for  $\gamma$ -ray detection [23, 24, 26, 27]: to further reduce environmental backgrounds in experiments at the solid or gas target setup at LUNA 400 kV, several shieldings have been designed for use with either the BGO or the HPGe detectors. A movable and compact lead shielding [23] used at the solid target beam line of the LUNA 400 kV accelerator, allows for a minimum thickness of 10 cm for the BGO detector and 15 cm for the HPGe detector. The BGO detector can be placed at the center of the shielding, while the HPGe detector can either be mounted at 0° or at a 55° angle with respect to beam direction, the latter is convenient to reduce the influence of unknown angular distributions.

Since in a typical experiment using solid targets they have to be replaced frequently, the shielding is sectioned in several parts mounted on rails that can be easily slid for easy access, or for concurrent use of different detectors.

In the case of the gas target beam line of the LUNA 400 kV accelerator is available a lead shielding composed of lead bricks for a total volume of 0.5 m<sup>3</sup> (80 × 70 cm<sup>2</sup> of base and 95 cm of height). It allows to surround up to two HPGe detectors with 25 cm thickness of lead [26]. The shielding includes as innermost layer oxygen free copper of 4 cm thickness with a very low intrinsic radioactivity. The achieved reduction of the environmental background is of a factor 10<sup>-5</sup> for  $\gamma$ -rays below 2 MeV. The shielding can be enclosed in a plastic box (radon box) that can be filled with N<sub>2</sub> gas to reduce at minimum the radon to get in contact with the detectors.

### 2.1.2 New instrumentation for nuclear physics

- VIP-3 experiment: the experimental effort of the VIP-2 experiment will be extended in depth and range to violations of the PEP in transitions on targets with higher *Z* materials. To this aim, the upgraded experiment VIP-3 will make use of 64 SDD cells in a larger vacuum chamber, doubling the active area. The calibration system will be upgraded as well as the target cooling systems, which will allow the maximum direct current to reach 400 A. Additionally, the VIP-3 setup will be equipped in a later stage with 1 mm thick SDDs improving the reach to higher *Z* material and enhancing the quantum efficiency of the detectors.
- New massive shielding for  $\gamma$ -rays detection: to measure the <sup>12</sup>C+<sup>12</sup>C fusion cross section, detecting the two low-energy  $\gamma$ -rays from the de-excitation of <sup>20</sup>Ne and <sup>23</sup>Na, the LUNA Collaboration is developing a setup composed by a lead (25cm) and copper (1cm) shielding to suppress the environmental  $\gamma$ -ray background. The  $\gamma$ -rays detection setup comprises a HPGe detector (150% relative efficiency) installed at 0° with respect to beam direction (in close geometry to the target to maximize the signal to noise ratio) and 8 NaI scintillator detectors surrounding both the target and the HPGe to reduce the Compton background and to enhance detection efficiency (see Sect. 4.2.6). The finalization of this setup is supported by the Italian Ministry of Research through the funding action PRIN2022.
- The assembly of a recirculating gas target and neutron as well as  $\gamma$ -ray detection systems is underway and has received funding from the ERC and the Italian Ministry of Research, respectively. The neutron detection system consists of a coupled array of liquid scintillators and <sup>3</sup>He counters (see Fig. 2 for the setup). Through capture-gating and coincidence/anticoincidence between the two detector types, energy sensitivity is achieved, which allows to remove unwanted beam-induced background from ( $\alpha$ , n) reactions on contaminants like boron or carbon.

**Fig. 2** Drawing of the gas target and detector configuration for the  $^{22}\text{Ne}(\alpha, n)^{25}\text{Mg}$  measurement

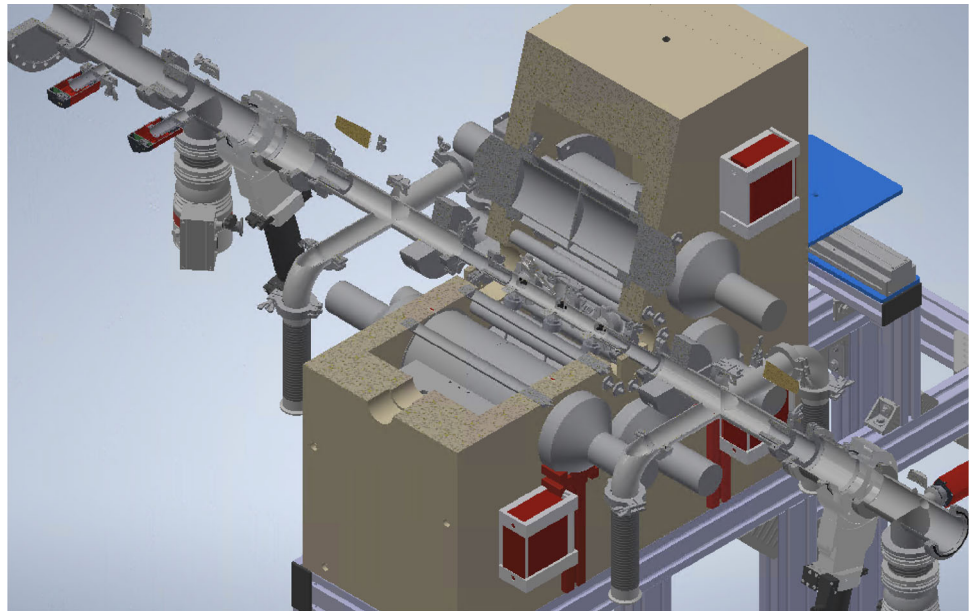
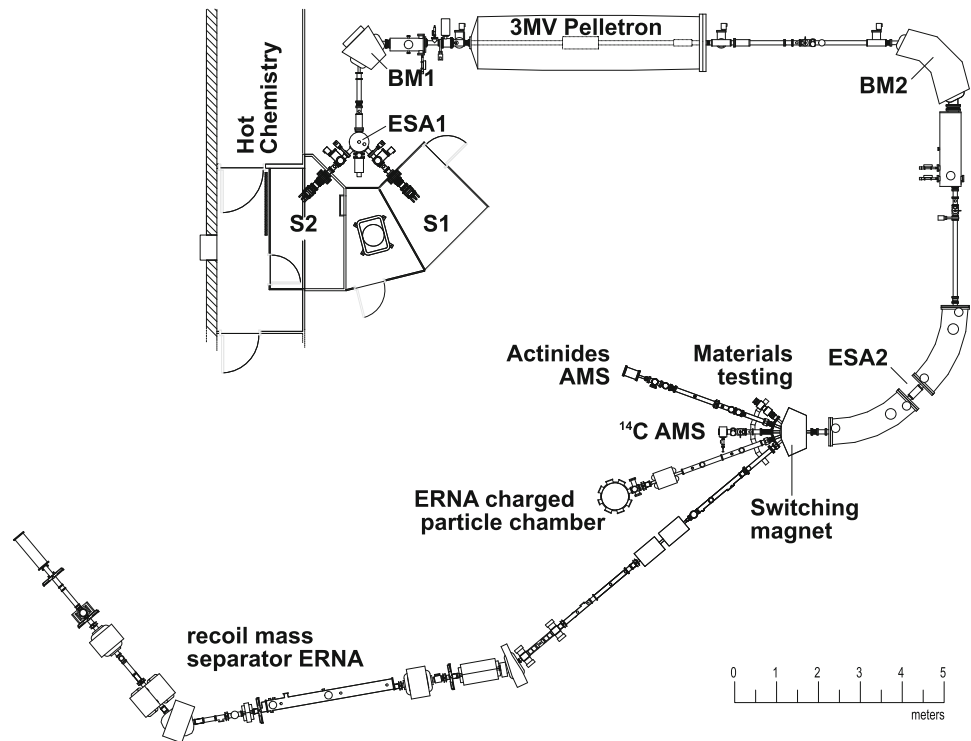


**Fig. 3** The layout of CIRCE Tandem Accelerator Laboratory



## 2.2 CIRCE

The Center for Isotopic Research on Cultural and Environmental heritage is a complex of laboratories of the University of Campania “L. Vanvitelli”, located in San Nicola la Strada (Caserta), Italy. The Tandem Accelerator Laboratory, shown in Fig. 3, hosts a 3.0 MV NEC 9SDH-2 Pelletron accelerator [28].

The accelerator is equipped with two 40-sample MC-SNICS Cs-sputter negative ion sources. One is used for the production of stable ion beams (e.g., C up to  $100\ \mu\text{A}$ , H up to  $10\ \mu\text{A}$ , depending on energy) and accelerator mass spectrometry (AMS) measurements. The second ion source is dedicated to the production of offline radioactive ion (RI) beams, in particular  $^7\text{Be}$  [29, 30].

The addition of an RF charge exchange ion source (Alphatross) will allow the production of  $\text{He}^-$ , as well as  $\text{H}^-$ ,  $\text{NH}^-$  and  $\text{O}^-$  beams with intensities up to several  $\mu\text{A}$ .

These sources give the opportunity to investigate processes with stable and RI beams in both fundamental research and applications.

### 2.2.1 Resident instrumentation for nuclear physics

The main instrumentation present at CIRCE for fundamental Nuclear Physics studies is tailored for Nuclear Astrophysics. Most of the equipment is developed and maintained by the ERNA Collaboration:

- ERNA recoil mass separator (RMS) is one of the few recoil mass separators devoted to the measurement of nuclear cross section of astrophysical interest. The ERNA RMS has two options for the target system: an extended windowless gas target [31] and a gas jet target [32, 33]. Different end detectors are available: a two-stage ionization chamber used as  $\Delta E - E_{\text{res}}$  telescope [34] and a position sensitive ToF-E detector capable of charge and mass identification, respectively, of the detected particles. An array of 18 NaI detectors can surround the jet target in a geometry optimized to measure angular distributions. The coincidence condition with recoils in the end detector provides almost background free  $\gamma$ -ray spectra.
- GASTLY: a dedicated beam line for the study of nuclear reactions relevant for astrophysics with charged particle spectroscopy is active since 2014. It is equipped with a large chamber hosting an array of  $\Delta E - E_{\text{res}}$  detectors, named GASTLY, optimized for low energy proton and  $\alpha$  particle discrimination [35]. Each GASTLY module houses in an aluminum pyramidal case, a detector telescope consisting of an ionization chamber (IC) for the  $\Delta E$  signal, and immediately behind the IC, a large area silicon strip detector (SSD) acting as the  $E_{\text{res}}$ . The array is presently mounted at backward angles,  $\theta_{\text{Lab}} \sim 96^\circ$  to  $163^\circ$ , each SSD strip subtends about  $1^\circ$ . The array can be rotated as a whole in  $90^\circ$  steps around the vertical axis. This detection setup has been successfully used for the measurement of the  $^{12}\text{C} + ^{12}\text{C}$  cross section [36].

### 2.2.2 Infrastructures and instrumentation for applied physics

The CIRCE Laboratory offers different opportunities with accelerated ion beams and hosts “State of the art” mass spectrometers routinely devoted to the measurement of stable and radioactive isotope ratios:

- Ion beam analysis with RBS and NRA is presently performed at CIRCE with different beams and setups. The ion beam is produced by the tandem accelerator and is purified by the AMS system, then is focused on target by means of a quadrupole magnet triplets. Targets can be mounted on a multi-sample holder. A new dedicated scattering chamber with a motorized five-axis target holder is being installed, in order to expand the available analysis techniques to Channeling-RBS and ERDA.
- SIRMS: stable isotope ratio mass spectrometry measurements for light elements (i.e., H, C, N, O and S) are performed by means of 2 Thermo Fisher Delta V mass spectrometers equipped with one dual inlet injection system for measurement of gaseous samples and two continuous flow interfaces with different peripherals (elemental analyzer (EA), thermal conversion/elemental analysis (TC/EA), gas chromatograph coupled with combustion or TC and gas bench) allowing for the measurement of different matrices (solid, liquids and gases) in automated mode.
- MC-ICP-MS: stable isotope ratio mass spectrometry measurements for other than light elements are performed by Thermo Fisher Neptune Plus multicollector (MC) inductively coupled plasma (ICP) mass spectrometer (MS) allowing the simultaneous measurement of different isotope signals with interferent (up to 10 different movable Faraday cups are present) also with the possibility of using a single electron multiplier to expand the measurement dynamic range.
- Multisource evaporation machine: this device allows the production of thin films, possibly multi-layered, to realize targets or coatings. It is equipped with an electron beam source and a plasma magnetron RF sputtering source. The possibility of producing layers of controlled thickness deposited on several materials is open to new applications. At present, the machine is used to produce metallic layers on polymeric material for the windows production for gas detector used in nuclear physics application like the ERNA final detector [34]. The RF can be moved from the magnetron sputtering source to the sample holder, by changing its polarization, in order to change the site of sputtering process and clean the backings’ surface just before the evaporation. The liquid-cooled multitarget holder can host up to 10 samples. A glovebox, with a gas purging system with inert gases, Ar or N, and a dedicated window for samples loading, is connected to the evaporation machine. This allows to avoid contamination by contact with ambient air and preserve purity of the evaporated samples.

In the study of nuclear reactions, the production of pure, stable and uniform target is of paramount importance. The target production with this evaporator allows, right at the end of the production process, for a complete characterization of thickness, composition and uniformity. These measurements are performed with the IBA techniques (NRA, RBS and ERDA). The target analysis can be also complemented by energy-dispersive X-ray spectroscopy using a scanning electron microscope (EDX-SEM) that allow the analysis of surface uniformity and the damage of the target.

## 3 Fundamental symmetries

The experimental search for possible violations of the Pauli Exclusion Principle (PEP) and the investigation of the foundational aspects of quantum mechanics (QM), including the collapse of the wave function, are fueling the VIP collaboration’s activities. These topics are interwoven and characterized by theoretical and experimental cross-fertilizations. On the one side, the VIP experiment challenges those phenomenological spin-statistics violation models, like the quon model, which require experimental verification



to constrain the free parameter of the theory. VIP provided the strongest bounds on this class of models, constantly improving the PEP violation probability, fulfilling the Messiah–Greenberg superselection (MGS) rule, to which they are subject. On the other side, non-commutative space-time, as a class of universality to investigate quantum gravity models, provides the suitable framework for the investigation of both fundamental symmetries and quantum collapse. Space-time non-commutativity induces spin-statistics violations at the fundamental level, not subject to the MGS rule. At the same time, it is connected to the possibility of recovering phenomenological models for the collapse of the wave function, while unveiling the measurement problem in QM. Indeed, phenomenological models of (gravitational) collapse of the wave functions can be derived from a theoretical top-down approach to the quantization of geometry. Moreover, recent phenomenological investigations by VIP offer, for the first time, the possibility to experimentally unveil the mechanism which is responsible for the collapse. At the same time, both fundamental symmetries and quantum foundations can be experimentally falsified resorting to ultra-high-sensitivity probes, and in particular to atomic transitions, by the VIP collaboration at LNGS.

VIP recently excluded the  $\theta$ -Poincaré model [37, 38], one of the most commonly adopted non-commutative quantum gravity (NCQG) models, for non-vanishing electric-like components of the theta tensor. The case in which the electric-like components are taken to be zero has been excluded up to almost one tenth of the Planck scale. Consequently, the collaboration has arrived, by running a high-precision experiment and developing a phenomenological and theoretical interpretation, to test quantum gravity, and other theories beyond the standard model (SM), with a very high precision that is still impossible to achieve at present day using accelerators in direct experiments.

On the other hand, the experimental studies carried out by the collaboration on wave function collapse models, contribute to shed light on the measurement problem in QM, and consequently on its foundational aspects. VIP demonstrated that high-sensitivity X- and gamma-ray tests, looking for the collapse induced spontaneous radiation emission, are the most sensitive probes of these models. Experimental efforts and phenomenological analyses carried out by the VIP collaboration in this context enabled to falsify, e.g., the Diósi–Penrose model [21] in its original cutoff-less version, and set stringent limits in its present formulation. The analysis of a novel geometric method for the stochastic quantization of fields that has been useful to bridge top-down theories of quantum gravity to the gravitational collapse of the wave function is now under scrutiny [39].

The main objectives of the midterm planned activities at experimental, phenomenological and theoretical level are:

1. To develop and investigate possible violations of the PEP in atomic transitions, focusing on several theoretical approaches: phenomenological [40], different classes of universality models of quantum gravity [41], considering various theoretical possibilities [37, 38], including the deformation/violation of fundamental symmetries [42], the emergence of non-locality effects at high-energy scales [43], claimed departures from unitarity [44] as well as the emergence of effects manifesting the existence of extra-dimensions;
2. To fully exploit the ultra-sensitivity on a broad energy range and directionality capability in the detection of electromagnetic radiation that will be probed by the collaboration, hence making the difference, with respect to similar attempts in the literature, in constraining very tightly the parameter space of the examined models;
3. To connect classes of universality of quantum gravity models that have been distinguished according to their possible implications to the fate of the PEP, as well as further classes of universality of quantum gravity models added to phenomenologically account for the collapse of the wave function, to the possibility of testing foundational aspects of QM, through the experimental data available on the measurement problem;
4. To recover a solid theoretical link between models of quantum gravity (and related universality classes) and their impact on the foundational aspects of QM that can be experimentally falsified, hence prospecting a new way to develop quantum gravity phenomenology.

In Sect. 3.1 a theoretical overview on the symmetries, theories and models which will be developed in the midterm future is provided (T1). Section 3.2 focuses on experimental activities planned to investigate the possible violation of the PEP (T2), while Sect. 3.3 provides a similar plan for experiments devoted to quantum collapse models (T3). Figure 4 reports the overall plan, see caption for details.

### 3.1 Pauli Exclusion Principle violation experimental studies

The search for possible violations of the PEP has hitherto enabled the VIP collaboration to exclude several scenarios of non-commutative space-time [37, 38] that represent different classes of universality for models of quantum gravity. This result has been achieved by considering PEP-violating atomic transitions, probed by the VIP-2 experiment, to arise from the deformation of the space-time symmetries that eventually would induce deformations of the spin-statistics theorem.

From the experimental side, this scenario can be further investigated by improving the statistics of the data acquired within the next upgrades of the experiment and searching for the presence of background directional effects arising from the eventual non-commutative structure of space-time. From a theoretical perspective, either departures from unitarity or non-locality, proper to some attempts of quantum gravity models, or the possible imprinting of extra-dimensions at “our dimensions”, or the deformation of the symplectic structures of the theory that may result in a generalization of the Heisenberg uncertainty principle, might as well be responsible for PEP-violating atomic transitions.

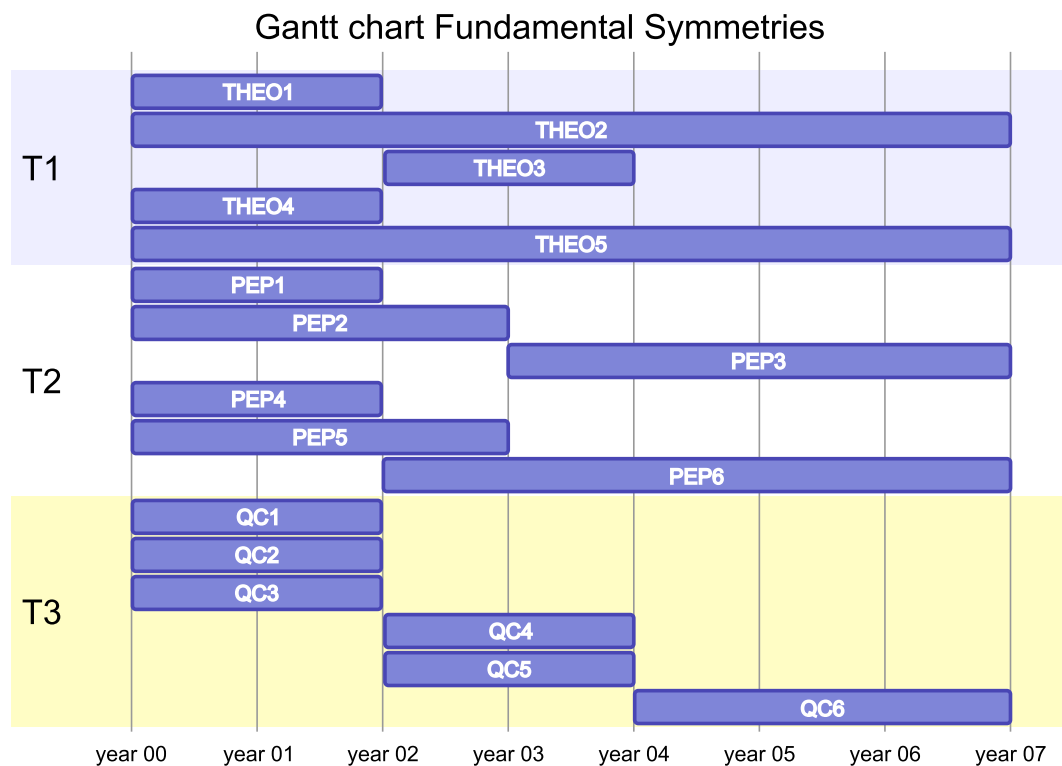


**Fig. 4** GANTT chart of the activities for the midterm future of WG1. T1 are the planned activities of Sect. 3.1, T2 of Sect. 3.2, and T3 of Sect. 3.3. In T1, THEO1 refers to the task “Explore of symmetries for PEP violations on Open Systems”, THEO2 to “Inhomogeneity and anisotropy of the geometry ground state”, THEO3 to “Generalized Uncertainty Principle as a class of universality”, THEO4 to “Extend falsification of quantum gravity models”, and THEO5 to “CPT violation and quantum decoherence, and the role of gravity”. For T2 the PEP1 refers to “Open-System data taking with the VIP-2 Experiment”, PEP2 to “Open-System experimental activity with the VIP-3 upgrade”, PEP3 to “Open-System activity with the 1 mm layers Silicon Drift Detectors”, PEP4 to “Open-System activity with the GATOR Setup”, PEP5 to “Closed-System activity with the Broad Energy Germanium Detector”, PEP6 to “Closed-System setup with anisotropy detection”. For T3, QC1 refers to the task “Extension of the Collapse Models”, QC2 to “Study of cancellation effects”, QC3 to “Study of the dynamics of the spontaneous radiation at low energy”, QC4 to “Upgrade of the low-noise electronics”, QC5 to “Study of dependence on target atomic number”, and QC6 to “Realization of a dedicated setup”

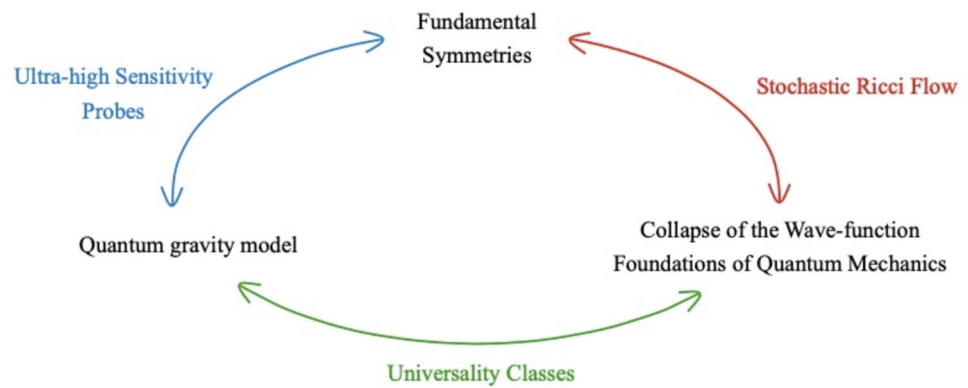
Top-down approaches in high-energy quantum field theory have been also developed to connect models for the gravitationally induced collapse of the wave function to quantum gravity theories, hence seeking to disentangle a long-standing issue in foundations of QM, such as the measurement problem. Among several models existing in the literature, interesting theoretical and phenomenological developments have been achieved in connection to the non-relativistic limit of the stochastic Ricci flow approach [39]. This is related to the notable model for the (gravitationally induced) collapse of the wave function that goes under the names of Diosi and Penrose [45–48]. The stochastic Ricci flow approach involves the breakdown of the fundamental symmetries of space-time and is consequently inextricably interwoven to the previous discussed topics of investigation of the fundamental space-time symmetries. Indeed, the decohering effect of the stochastic gravitational noise is at the base of both the collapse of the wave function, as driven by the Ricci drift term, as well as the breakdown of the space-time symmetries in out-of-equilibrium configurations.

The midterm aim of the collaboration is to further develop the phenomenology of fundamental symmetries, including discrete and continuous space-time symmetries, and to study the foundational aspects of QM, including the measurement problems and related studies on the collapse of the wave function of quantum systems, as basis of future experimental upgrades. These latter include electromagnetic radiation spectra in the keV-MeV energy range, as well as related measurements of atomic transitions. More specifically, we plan:

1. To enhance the understanding of physics at the Planck scale, while testing a fundamental principle of nature such as the PEP, with very high precision and at microscopic scales hitherto inaccessible;
2. To solve long-standing issues related to the interpretation of the measurement process in QM, from a statistical mechanics and complex system perspective that is relevant to quantum many-body systems and quantum information theory. This is related to decoherence of entangled quantum systems and to the appearance of stochastic noise of gravitational origin in the out-of-equilibrium dynamics.

We then aim at unveiling the ultimate consequences of quantum space-time fuzziness, modeled as stochastic noise, to the out-of-equilibrium dynamics of quantum many-body systems, then to the decohering effects and the collapse of the wave functions of the systems experimentally under scrutiny.

**Fig. 5** Main objective of the midterm plan in fundamental symmetries



The outcomes of these combined experiment, phenomenological analyses and theoretical investigations will then either unveil a first signal of physics beyond the SM, or rule out entire classes of quantum gravity models, with related consequences for the quantum measurement problem and models of collapse of the wave function, thus representing a milestone in the investigation of the fundamental symmetries and of the foundational aspects of QM.

Resorting to its consolidated expertise on this matter, the collaboration intends to develop detailed phenomenological analyses of the consequences of the constraints recovered by the future upgrades of the experimental apparatus on the atomic transitions that violate the PEP. These limits will be used to constrain the parameter spaces of several models of quantum gravity, using universality classes of non-commutative space-time, as well as stochastic models of quantization of gravity and concrete realizations of quantum gravity scenarios that either violate non-locality or deform the symplectic symmetry structure of the theory.

Therefore, the main objectives inspiring the program of the midterm group activities provide a circular feedback, intertwining experiment, phenomenology and theory, as shown in Fig. 5.

In particular, the activities in the midterm plan for T1 are as follows.

The THEO1 activity will focus on the exploration of symmetries for PEP violations on Open Systems (year 1–year 2). The collaboration will continue developing a detailed phenomenology of non-commutative space-time models, investigated as a class of universality of quantum gravity.

Tighter constraints on these universality classes will be disentangled from the stronger limits experimentally recovered, while information about directionality of the electromagnetic radiation emitted will enable to test possible quantum non-commutative background anisotropies that have been predicted THEO2 (year 1–year 7).

In this area, another class of universality worth of investigation is represented by those models that break/deform the symplectic symmetry, which will allow not only to connect PEP violations to space-time non-commutativity, but also more in general to possible subsequent (THEO3, year 3–year 4) generalizations of the Heisenberg uncertainty principle, allowing to falsify numerous theoretical models yielding prediction on this.

In the THEO4 activity (year 1–year 2), an extension of falsification of quantum gravity models will also be done. The class of universality of non-local quantum field theories will be addressed in great detail. Specifically, a connection between non-local quantum field theory approaches to the quantization of gravity—in particular super-renormalizable theories of gravity, the non-locality of which is induced by the introduction in the action of the theory of form factors expressed by transcendental functions—and possible breakdown/deformation of the spin-statistic theorem, will be investigated in order to derive falsifications of this universality class of quantum gravity models, in which also specific realizations of string theory and causal triangulations fall.

The stochastic Ricci flow is a tool for the stochastic quantization of the gravitational field that is complemented with the conformal transformations generated by the classical Ricci (minus the matter Ricci target) drift term—in other words, the Einstein equations reached classically at equilibrium. This general scheme was introduced over the last four years by a member of the collaboration, in light of the possible implications for quantum cosmology, in order to go beyond the frozen-time formalism, and more in general for the renormalization group flow of the gravitational field. Nonetheless, the same framework has been proved to have profound consequences for the very foundations of QM, for both the deep and intimate link of the stochastic quantization approach to Nelsonian models of QM [49–52] and the phenomenological models for the gravitationally induced collapse of the wave function of quantum systems. While the collaboration aims at clarifying the possible observational signatures of the dynamical relaxation toward the fundamental symmetries at equilibrium, as predicted by the stochastic Ricci flow scheme, it will be also relevant for this research line of our planned activities to achieve a solid establishment of the link between this geometric stochastic quantization method, seen as a class of universality of quantum gravity models, and the phenomenological models of wave function collapse (THEO5, year 1–year 7).

This will open the pathway to a novel direction to test quantum gravity models through the tight constraints that will be derived experimentally on the models of wave function collapse from the limits on the accompanying electromagnetic radiation that is supposed to be emitted.

### 3.2 Quantum gravity, CPT and Lorentz symmetries and the Pauli Exclusion Principle violation

The experimental investigation of fundamental symmetries, through high-sensitivity tests of Spin-Statistics violation/deformation, follows two parallel lines which are named VIP Open Systems and VIP Closed Systems, as a direct consequence of the two distinct classes of theoretical models which embed Spin-Statistics violation/deformation. For both VIP Open Systems and VIP Closed Systems the searched new-physics experimental signature is represented by PEP-violating atomic transitions to the fundamental level, when this is eventually already filled by two electrons. The energy of this transition is expected at a different energy with respect to the standard one. The calculation of the Pauli-forbidden radiative-transition energies is independent—at the first order—from the specific model and is performed by using the MCDFGME numerical code [53]. This program solves the multiconfiguration Dirac–Fock equations self-consistently, taking into account relativistic effects (see [54, 55, and references therein]).

Attempts of formulating theoretical models which violate the statistics of identical particles were pioneered by Fermi [56, 57], who discussed the implications of an even tiny non-identity of electrons. Gentile introduced an intermediate statistics [58], while a parastatistics was developed by Green [59]. Ignatiev and Kuzmin presented a model consisting in a deformation of the standard Fermi oscillator [60–62], also discussed by Okun [55]. In this approach, a three-level Fermi oscillator is considered, in which the additional level can be accessed with a probability  $\beta^2/2$ .  $\beta$  is still currently used in this research field to represent the amplitude of a PEP-violating transition. Rahal and Campa investigated the consequences of small PEP violations on the thermodynamic properties of matter [63]. Greenberg and Mohapatra [64, 65] formulated a local quantum field theory embedding PEP violation, named *quon model*. We refer to Ref. [66] for a more detailed review. The experimental investigation of the above-mentioned theories is strongly demanded to constraint the free parameter of the models, but is complicated by a stringent condition known as the MGS rule [67]: the transition amplitude between two different symmetry states is zero. VIP Open Systems set the most stringent bounds on  $\beta$  respecting MGS [18], by checking the newly formed symmetry state, which follows the introduction of new fermions in a given system of identical fermions, according to a suggestion by Greenberg and Mohapatra [64]. The present status and results of the VIP-2 Open Systems experiment are outlined in Sect. 3.2.1.

More recent is the prediction of spin-statistics deformation related to the space-time non-commutativity [40, 44, 68, 69], common to several quantum gravity frameworks (the two main classes of NCQG are  $\kappa$ -Poincaré and  $\theta$ -Poincaré) or connected to CPT deformation [70]. This class of models predicts PEP violation, not constrained by the MGS. Depending on the specific model, the PEP violation probability  $\delta^2$  is a function of the energies involved in the transition under study. It depends on the characteristic energy scale of new-physics emergence and can be subject to not isotropic corrections. The present status and results of the VIP Closed Systems experiment, which is investigating this rich new phenomenology, are described in Sect. 3.2.2.

#### 3.2.1 VIP-2 Open Systems, present status and results

The goal of the ongoing VIP-2 experiment is to improve by at least two orders of magnitude the result obtained by VIP ( $\beta^2/2 < 4.7 \times 10^{-29}$  [71, 72]).

The main improvements of the experimental apparatus (see Refs. [54, 73] for a detailed description) consist in: *a*) the replacement of the charged coupled devices for the X-rays detection, with state-of-the-art, 450  $\mu\text{m}$  thick, silicon drift detectors (SDDs), characterized by a higher energy resolution (190 eV (FWHM) at 8 keV), large geometrical acceptance and an efficiency of 99% at 8 keV, *b*) a more compact and thinner target ensuring higher acceptance and efficiency, *c*) a new target cooling system which allows an enhanced circulating current (with a peak value of 180 A with respect to the 40 A of VIP). After an exploratory data taking run (2016–2017) [54, 73] exploiting two arrays of  $1 \times 3$  SDDs, the fully upgraded setup was completed (2018–2019), by mounting four arrays of  $2 \times 4$  SDDs cells and the external passive shielding complex (an outer lead layer surrounding an internal copper layer), aimed to provide further suppression of the environmental background radioactivity. The VIP-2 experiment has been operating in its final configuration since May 2019, by alternating data taking periods with current flowing to periods without current, which provide the reference background spectrum.

The sensitivity of the VIP-2 experiment was demonstrated by a progressive approach of the  $\beta^2/2$  limit to the foreseen goal [54, 73, 74]. The strongest bound on the PEP violation probability, consistent with the MG superselection rule (see Ref. [18]), was recently achieved by VIP-2, from the analysis of the data corresponding to about six months of experiment operation in its final configuration. Two analysis frameworks were followed, a Bayesian statistical model and a frequentist Confidence Levels ( $\text{CL}_s$ ) approach, which share the same spectral shape description for the signal and the control spectra. The obtained limits are found to be well consistent within one sigma. The analyses yield:

$$\beta^2/2 \leq 8.6 \times 10^{-31} \text{ (Bayesian)} \quad \beta^2/2 \leq 8.9 \times 10^{-31} \text{ (CL}_s\text{)}, \quad (1)$$

when the electron propagation in the target is described by means of an electron diffusion model [75], i.e., the number of electron–atom interactions is obtained from the ratio of the target length and the electrons scattering length in copper. According to more realistic diffusion models [76, 77], on which we are recently working, electron–atom interactions in copper occur over a characteristic time

$\tau = 3.3 \times 10^{-17}$  s, therefore significantly increasing the number of independent PEP tests performed by each current electron, leading to the enhanced limits:

$$\beta^2/2 \leq 6.8 \times 10^{-43} \text{ (Bayesian)} \quad \beta^2/2 \leq 7.1 \times 10^{-43} \text{ (CL}_s\text{)}. \quad (2)$$

### 3.2.2 VIP Closed Systems, present status and results

The analysis of the total data set collected by the VIP Closed System experiment recently provided the strongest (atomic transitions) experimental test of the  $\theta$ -Poincaré NCQG model [37, 38], looking for anomalous atomic transitions in the X-ray domain.

The experimental setup is based on a coaxial p-type HPGe detector, about 2 kg in mass. The detector is surrounded by a target, consisting of three 5 cm thick cylindrical sections of radio-pure Roman lead, for a total mass of about 22 kg (see Ref. [66] for a detailed description of the apparatus and the acquisition system).

The first phenomenological analysis was performed, which accounts for the predicted energy dependence of the PEP violation probability. Upper limits are set on the expected signal of PEP-violating  $K_\alpha$  and  $K_\beta$  transitions, generated in the target, by means of a Bayesian comparison of the measured spectrum with the violating K complex shape predicted by the  $\theta$ -Poincaré model.

The analysis yields stringent bounds on the non-commutativity energy scale, which exclude  $\theta$ -Poincaré up to  $2.6 \times 10^2$  Planck scales when the “electric-like” components of the  $\theta_{\mu\nu}$  tensor are different from zero, and up to  $6.9 \times 10^{-2}$  Planck scales if they vanish.

### 3.2.3 VIP Open Systems future plans

The midterm plans for T2 on VIP Open System research line over year 1 to year 2 aims at concluding the data taking with the VIP-2 detector (PEP1) and preparing for the experimental upgrade.

The future of the research for MG allowed PEP violation, demands for a scan of the PEP violation probability—with sensitivity comparable to VIP-2—as a function of the atomic number. The importance of “such tests, over the entire periodic table” was outlined, e.g., in Ref. [55]. The main technical challenge to be faced, when testing PEP-violating atomic transitions for metals characterized by a higher atomic number than copper, is represented by the SDD detectors quantum efficiency decrease, as a function of the increasing energy to be detected. The scan will be performed by means of the VIP-3 apparatus, using innovative 1 mm thick SDD detectors, till atomic numbers as high as  $Z \sim 50$  as described in the following. Intermediate atomic number materials will be tested exploiting a layered architecture of 1 mm thick SDDs (see Sect. 3.2.3). The higher  $Z$  range will be explored by the VIP-GATOR collaboration using the low-background GATOR germanium counting facility [22], with the implementation of dedicated ultra-pure target systems (see Sect. 3.2.3).

*The VIP-3 experiment* The VIP-3 represents the WG effort on T2 for the year 1 to year 3 (PEP2). Our group is presently developing new cutting edge SDD detectors in collaboration with Fondazione Bruno Kessler (FBK, Italy) and Politecnico di Milano (PoliMi, Italy). The new technology is characterized by double thickness, with respect to the standard detectors used in the VIP-2 experiment (1 mm versus 0.45 mm). We have already demonstrated (see Fig. 6) that the quantum efficiency of the new SDDs, in the energy range 20–25 keV, is roughly double with respect to the standard detectors, keeping constant the energy resolution. This will allow to investigate eventual PEP violation induced deviations from the standard  $K_\alpha$  transitions, in palladium, silver and tin (see also Ref. [78]). As an example, in silver the PEP-violating  $K_{\alpha 1}$  transition is shifted of 482 eV with respect to the standard line, the corresponding shift for the  $K_{\alpha 2}$  is 478 eV. Comparable shifts are found in palladium and tin.

The production of the new SDD devices is presently under finalization. The new system is characterized by pixel dimensions of 7.9 mm  $\times$  7.9 mm, and the width of the last ring was extended in order to improve collection at the border of the active area. The total chip dimensions are 35.6 mm  $\times$  19.8 mm, i.e., about 2 mm wider than the previous chips. The geometry of the SDD arrays will consist of a 2  $\times$  4 matrix, whose anode side is shown in Fig. 7. Among the main improvements characterizing the new detector system, we want to mention the introduction of a layout solution on the window-side, to reduce the charge sharing effect; moreover, the robustness of the bonding pads was enhanced [78].

During PEP2, the activity will proceed with the finalization of the setup. More in detail the layout of the compact targets-SDD detectors system is shown in Ref. [78]. The planned configuration consists of 8 SDD arrays, facing two target strips, where the direct current will be circulated. With respect to the 4 SDD arrays presently arranged in the VIP-2 setup, VIP-3 will exploit a total of 64 SDD cells, for a double active area of about 41 cm<sup>2</sup>, in order to increase the geometrical efficiency. A new calibration system will be developed; moreover, a new thermal contact between the cold-finger and the SDD detectors, and a new target cooling system will be built, both in OHFC ultra-pure copper, to minimize the natural copper radio-contamination. The improved thermal conductivity, with respect to the steel thermal contact and cooling system presently used in VIP-2, will reduce the detectors working temperature (improving the energy and timing resolution) and will also increase the applicable maximum current circulating in the target (from the 180 A peak current of VIP-2 up to 400 A). The design of the new vacuum chamber is also shown in Ref. [78].

This will be followed by assembly, testing, debugging and mounting of the setup and of an upgraded shielding, implementing a further inner polyethylene tier, at LNGS.

**Fig. 6** The figure, from [78], shows the simulated quantum efficiency as a function of the energy, for SDD devices of various thicknesses. The black curve corresponds to the detectors currently used in VIP-2, and the green curve shows the efficiency achievable with the new 1 mm thick SDDs which we are presently developing for the VIP-3 experiment

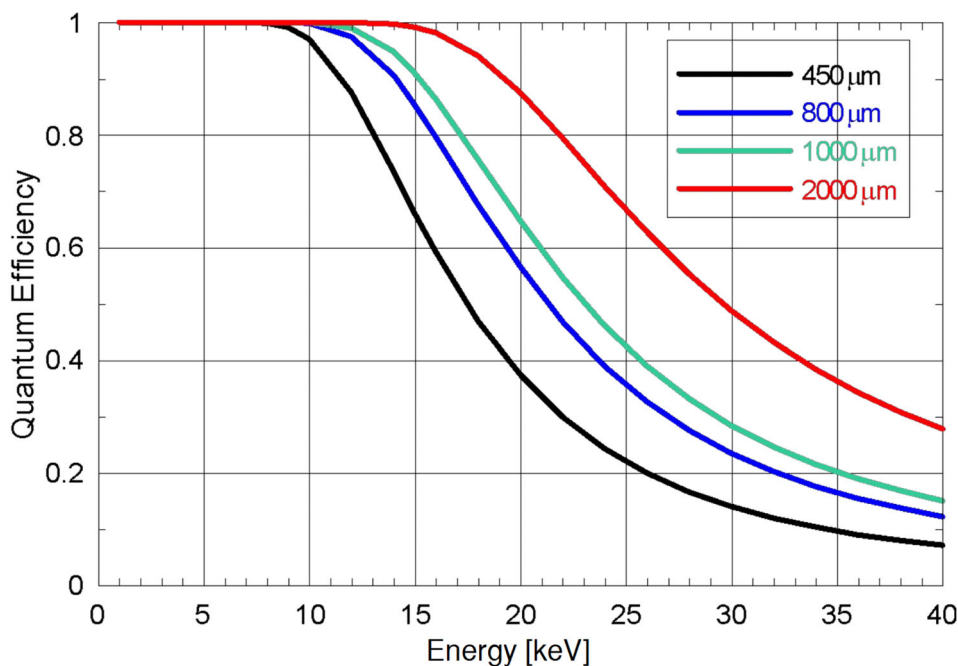
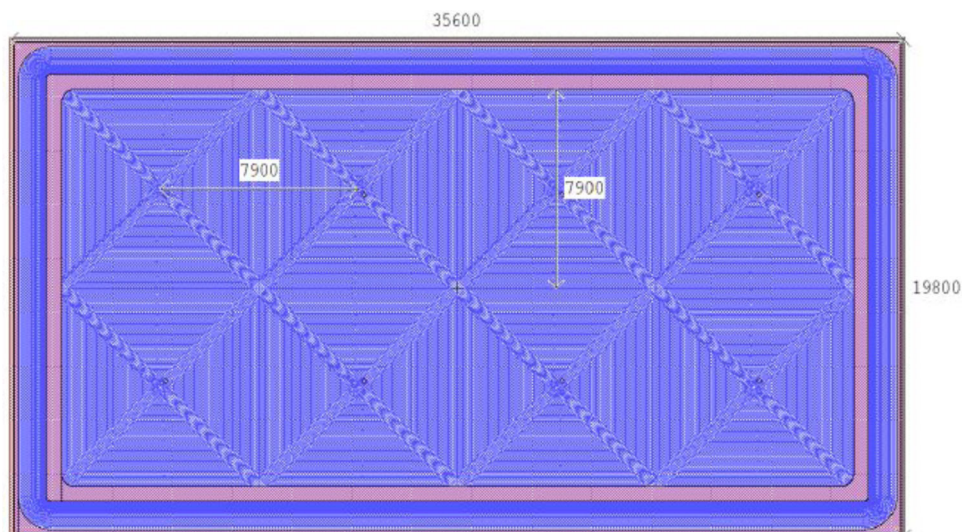


**Fig. 7** The figure, from [78], shows as seen from the anode side, the layout of the main SDDs array being produced for the VIP-3 experiment

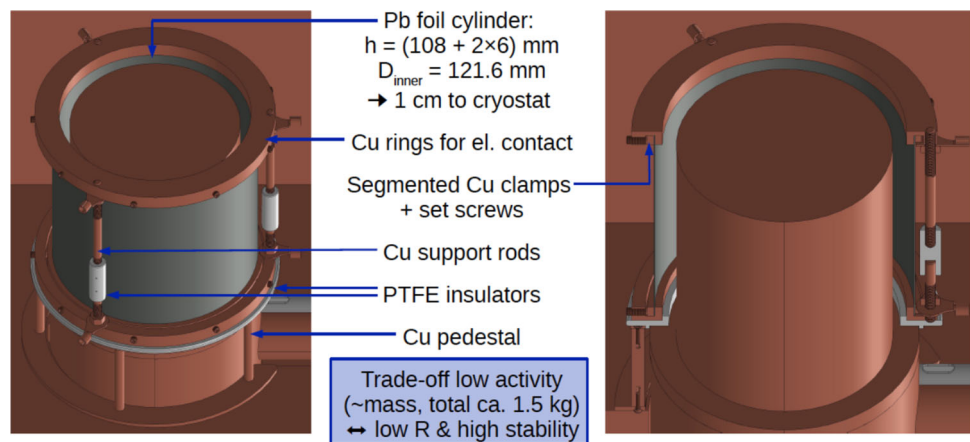


The introduced improvements listed above compensate the quantum efficiency reduction for increasing the energy from 8 keV up to 25 keV, thus keeping at least constant the sensitivity of the experiment.

The next 3-year period will be dedicated to data taking, alternating runs with and without current, and to the analysis of the collected data.

**Beyond VIP-3: 1 mm thick SDDs** After the experimental upgrade VIP-3 (PEP2), from year 4 to year 7, the Open System activities will focus on the 1 mm thick SDDs (PEP3). In fact, the search for PEP-violating atomic transitions for elements characterized by intermediate atomic numbers ( $Z \sim 60$ ), with sensitivity comparable to VIP-2, requires a further improvement in the quantum efficiency of the detectors. This will be obtained by means of the development of layered structures of 1 mm thick SDDs. For higher  $Z$  elements the shift of the violating  $K_{\alpha}$  lines, with respect to the standard transition, becomes comparable or larger than the HPGe detectors energy resolution, hence an HPGe based setup becomes preferable (see Sect. 3.2.3).

**Fig. 8** Design of the optimized inner configuration of the VIP-GATOR experiment detector system, figure courtesy of Alexander Bismark



Research activity on a layered architecture of 1 mm thick SDDs (where two SDDs are placed one above the other) will be performed during year 3. The period year 6 to year 7 will be dedicated to the development of the layered structures of 1 mm thick SDDs, to the design and realization of the improved experimental apparatus (new SDDs system cooling block, new vacuum flange connectors (more pins) to bring the signals out to the DAQ, etc.). We then plan a data taking period of three years, alternating periods with current circulating in the targets to periods without current, energy calibration runs and continuous maintenance of the VIP laboratory space and of the setup.

*VIP-GATOR: Open Systems test for high Z elements* During 2022 a joint effort started between the VIP collaboration and the ETH Zurich group (lead by Prof. Laura Baudis) aimed at the realization of high-sensitivity measurements of  $\beta^2/2$ , fulfilling the MGS, in the high Z range of the periodic table. This will articulate an experimental effort from year 1 to year 2 (PEP4).

The experiment will use the GATOR facility [22] at LNGS, with the implementation of a dedicated target system composed by: high radio-purity materials (Pb, Au, Pt, etc.) targets fed by a 400 A direct current power supply, target cooling system and feed-through flange. GATOR is a low-background germanium counting facility with a core p-type coaxial HPGe detector with 2.2 kg sensitive mass. The energy resolution of the detector is 1.1 keV FWHM at 74.96 keV, corresponding to the standard  $K_{\alpha 1}$  line in Pb. The energy shift among the standard and the PEP-violating  $K_{\alpha 1}$  transitions is 1.25 keV.

An exploratory measurement was performed above ground, as reported in [79], exploiting a point-contact Ge detector and a Pb target circulated by a 110 A current, and the limit  $\beta^2/2 < 1.5 \times 10^{-27}$  was established.

Geant4 Monte Carlo simulations were performed with the aim to optimize the target geometry and thickness, in order to maximize the photons detection efficiency and the maximum circulating current which is compatible with power dissipation. A design of the optimized inner configuration of the detector system is shown in Fig. 8; to give an example, the thickness of the cylindrical Pb target is 25  $\mu\text{m}$ .

The realization of the Pb target is presently ongoing. The design of the feed-through flange of the cabling/connectors and of the target/cables cooling system is presently under finalization. Based on the performed MC studies, a three-month measurement of the VIP-GATOR experiment will improve the result in [79] of at least two orders of magnitude.

The finalization of the setup realization and three/four months of data taking with Pb target are previewed for year 1. A scan over several high Z targets will be performed in the year 2.

### 3.2.4 VIP Closed Systems future plans

The midterm future experimental activity in the Closed Systems context is aimed to extend the falsification of quantum gravity models, to perform tests of the Generalized Uncertainty Principle, to investigate the interplay among CPT violation and quantum decoherence and the role of gravity. This will be accomplished by means of a Broad Energy Germanium Detector (BEGe)-based system, as described below, during year 1 to year 3 (PEP5). The long-term plan will be addressed to the search for signal of inhomogeneity and anisotropy of the geometry ground state in year 2 to year 7 (PEP6).

#### VIP Closed Systems—BEGe-based setup

The falsification of the  $\theta$ -Poincaré NCQG model, for vanishing  $\theta_{\mu\nu}$  “electric-like” components, requires the improvement of the current lower limit on the non-commutativity scale  $\Lambda > 6.9 \times 10^{-2}$  [37, 38] of a factor 15. Considering that the PEP violation probability is given by:

$$\delta^2 \simeq \frac{\bar{E}_1}{\Lambda} \frac{\bar{E}_2}{\Lambda} \tag{3}$$

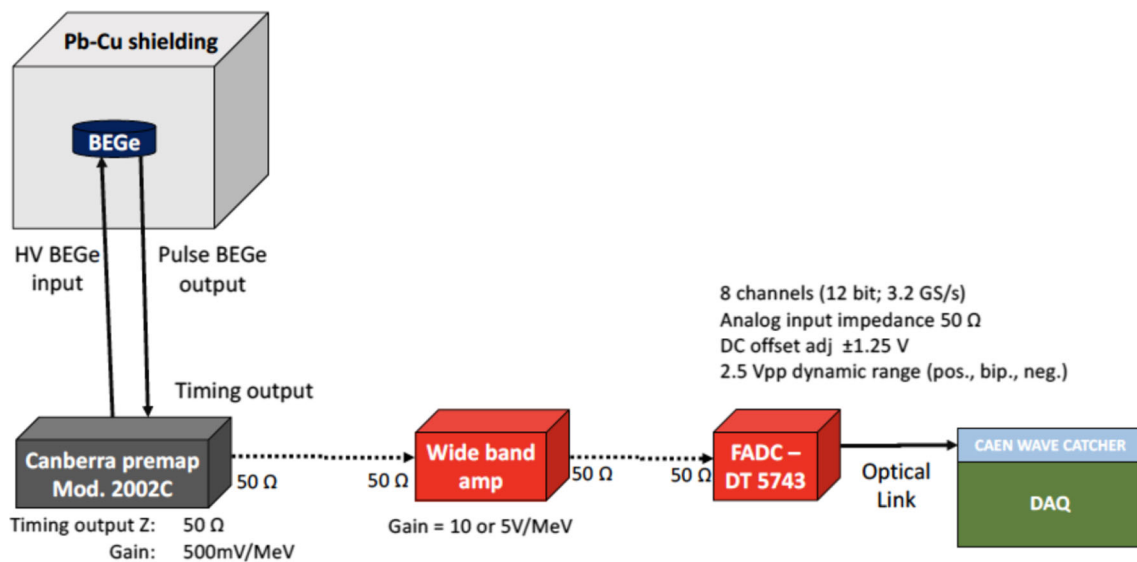


**Fig. 9** Block diagram of the BEGe-based system

where  $\bar{E}_{1,2}$  are the energy levels occupied by the initial and the final electrons, the strategy is to use the Germanium as an active target, and to search for  $K_{\alpha}$  violating transitions in the Ge crystal itself. Considering the energy of the levels in Ge and Pb, the sensitivity of the experiment has to be improved of a factor  $s \sim 2 \times 10^4$ . This will be accomplished exploiting the incremented efficiency, which is  $\epsilon_{Pb} = (5.39 \pm 0.11) \times 10^{-5}$  for the detection of a PEP-violating  $K_{\alpha_1}$  transition occurring in the Pb target of our previous experiment, and is  $\epsilon_{Ge} \sim 1$  for the detection of a PEP-violating  $K_{\alpha_1}$  transition generated in the Ge crystal. The main difficulty is represented by the high background level, due to electronic noise, which characterizes the HPGe detectors below 20 keV, which makes impossible the measurement of the PEP-violating germanium  $K_{\alpha}$  lines. The strategy is to exploit a BEGe-based setup, which allows, by means of pulse shape discrimination techniques, to reject the electronic noise and to disentangle photons produced inside the crystal from photons impinging from outside the detector.

A test setup was already realized and two data taking runs were performed in the period 2021–2022, which served for the DAQ optimization. A block diagram of the BEGe-based system is shown in Fig. 9. The BEGe detector is cooled to 80 K by means of  $\text{LN}_2$ , contained in a dedicated dewar, and is surrounded by two layers of Cu and Pb shielding. The CAEN FADC is characterized by a 12 bit resolution and a 3.2Gs/s sampling rate, which allows to reconstruct the shape of the incoming signals. A wideband low-noise amplifier, with a gain of a factor 10 in voltage, serves to increase the amplitude of the BEGe signals corresponding to photons of few keV. An extremely low-noise power supply was realized for the digitizer and the amplifier.

We have developed and tested a machine learning-based pulse shape discrimination (PSD) procedure. While dedicated algorithms for PSD require extensive fine-tuning and calibrations, deep learning techniques have already been pioneered for the GERDA and MAJORANA experiments [80] showing the potential to match the state-of-the-art algorithms. We applied convolutional neural networks (CNN) for discriminating between single-site events, in which the energy is deposited in a single location within the detector, and multi-site events, in which the energy is distributed over multiple locations. A CNN was developed and trained on a dataset of simulated pulse shapes from single-site and multi-site events, representative samples are shown in Fig. 10. The CNN performance was evaluated by using various metrics, and our results show that is able to accurately discriminate between single-site and multi-site events, with a classification accuracy of better than 95%.

For PEP5, the period year 1 to year 2 will be dedicated to data taking and to the analysis of the collected data in the context of NCQG, CPT violation and Generalized Uncertainty Principle theories. Additionally, during year 3 to year 4 several data taking campaigns will be performed alternating various targets, to also explore the energy dependence of the  $\delta^2$  which is predicted in NCQG.

*Test of quantum gravity induced anisotropy effects* The longer-term plan experimental activity on fundamental symmetries in Closed Systems will be focused on the first time ever investigation of Quantum Gravity induced anisotropy effects. The experimental setup will be capable of probing the directionality of the electromagnetic field background emission and will allow to recover tighter limits on space-time non-commutativity, testing possible tensor background effects that are peculiarly expected in string theory. These effects are predicted because of the non-vanishing vacuum expectation value of anti-symmetric background fields, which is at the very origin of space-time non-commutativity, and hence of the deformation of the fundamental symmetries.

The experiment will measure directionality of the electromagnetic radiation emitted in atomic transitions exploiting a  $4\pi$  detection geometry. The central targets will be surrounded by layered structures of 1 mm thick SDDs. The targets will be embedded in magnetic



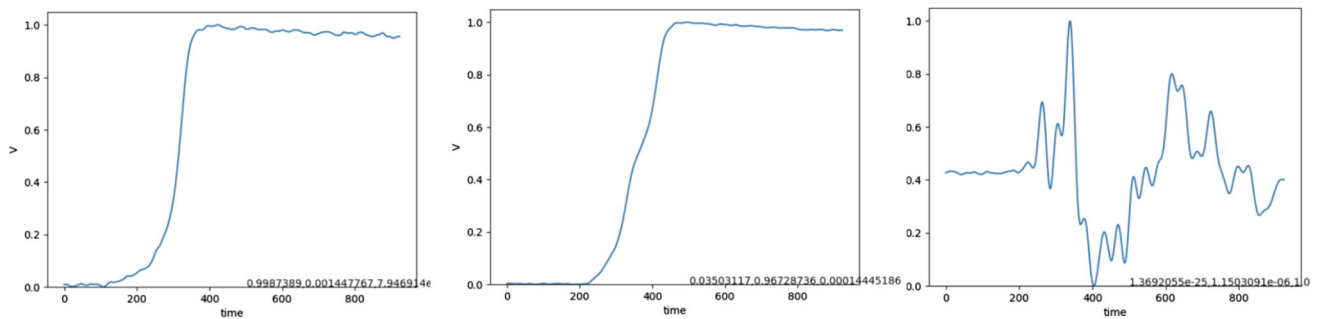


**Fig. 10** Examples of pulse shapes from physics data from the BEGe detector, the vertical axis reports the normalized pulse amplitude, and the horizontal axis the time in AU. (Left) Single-site event, in which the energy is deposited in a single location within the detector, identified with 99% accuracy. (Center) Multi-site event, in which the energy is distributed over multiple locations, identified with 97% accuracy. (Right) Noise event, representing background radiation or other sources of interference, identified at 99% accuracy

fields which will introduce the directionality-dependence, necessary to unveil a characteristic and still unexplored signature of the quantum gravity predictions. The setup will be surrounded by a complex of pure lead, electrolytic copper and polyethylene shielding system and by a performant veto system against residual cosmic and environmental radioactivity background.

The previewed experimental program PEP6 will have a duration of five years. The first two years will be dedicated to the R & D of a new setup, one year will serve for the realization and test of the setup, which will be followed by two years of data taking.

### 3.3 Quantum collapse models and their experimental tests

The wave function collapse or the measurement problem in QM refers to the conflict between the deterministic evolution of a quantum system described by the Schrödinger equation and the stochastic collapse of the wave function that occurs as a consequence of the measurement. This issue was first brought to light by Schrödinger’s famous thought experiment [81], known as the Schrödinger’s cat paradox, which highlighted the contradiction between the microscopic and macroscopic realms in QM.

The Schrödinger equation describes the evolution of a quantum system in terms of a linear, deterministic differential equation. However, when a measurement is performed on a system in superposition of different states, the wave function abruptly collapses to a single eigenstate of the observable being measured. This process, known as wave function reduction, is nonlinear and stochastic in nature and has been postulated as an ad hoc addition to the Schrödinger equation to account for the lack of superposition in macroscopic objects.

At a fundamental level, several questions arise circa the foundation of QM. Why and how do we have a boundary between the two dynamics? Why the quantum properties of microscopic systems, e.g., the possibility of being in a superposition of different states at once, do not carry over to larger objects? Fundamental question has a relevance also in light of the recent advancements in quantum technologies, which make use of quantum superposition. Will an isolated system manifest linear and deterministic Schrödinger evolution forever?

Spontaneous collapse models propose dynamics able to explain the breakdown of the linear, deterministic evolution into the collapse [82–87]. The most discussed in literature are the Diósi–Penrose (DP) and Continuous Spontaneous Localization (CSL) models. In the DP model [45–48, 88], gravity plays a major role. As soon as a ‘significant’ amount of space-time curvature is introduced, the rules of quantum linear superposition must fail. If two states in superposition are displaced by a distance **d**, with a mass density  $\mu(\mathbf{r})$ , the self-potential difference  $\Delta E_{DP}$  of the states in superposition can be written:

$$\Delta E_{DP}(\mathbf{d}) = -8\pi G \int d\mathbf{r} \int d\mathbf{r}' \frac{\mu(\mathbf{r})[\mu(\mathbf{r} + \mathbf{d}) - \mu(\mathbf{r}')] }{|\mathbf{r} - \mathbf{r}'|} . \tag{4}$$

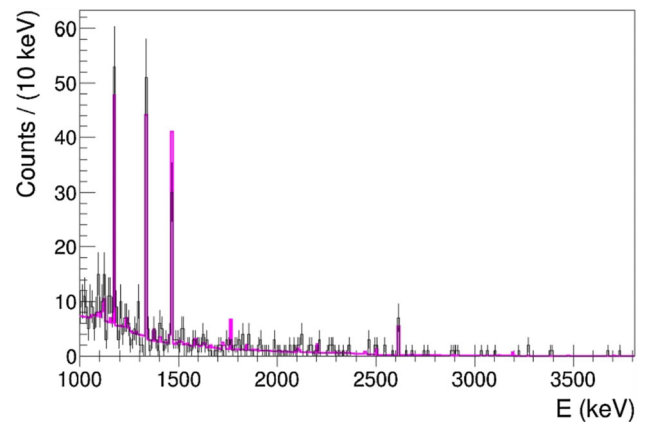
The wave function collapse takes place with a characteristic time  $\tau_{DP} = \hbar/\Delta E_{DP}$ . For microscopic systems, the superposition is preserved, and the characteristic time is very long. For a proton, for example,  $\tau_{DP} \simeq 10^6$  years, while for a dust grain  $\tau_{DP} \simeq 10^{-8}$  seconds. Superposition in macroscopic systems is almost immediately suppressed, recovering the reduction postulate.

The CSL model [85, 89, 90] is a stochastic and nonlinear modification of the Schrödinger equation:

$$d|\psi_t\rangle = \left[ -\frac{i}{\hbar} H dt + \frac{\sqrt{\lambda}}{m_0} \int d\mathbf{x} (\mu(\mathbf{x}) - \langle \mu(\mathbf{x}) \rangle_t) dW_t(\mathbf{x}) - \frac{\lambda}{2m_0^2} \int d\mathbf{x} \int d\mathbf{y} e^{-\frac{(\mathbf{x}-\mathbf{y})^2}{4r_c^2}} (\mu(\mathbf{x}) - \langle \mu(\mathbf{x}) \rangle_t)(\mu(\mathbf{y}) - \langle \mu(\mathbf{y}) \rangle_t) \right] |\psi_t\rangle .$$

In the first addend, one can recognize the system’s Hamiltonian *H* within the standard Schrödinger dynamics. The model depends on the parameters  $\lambda$  and  $r_c$ , the collapse strength and correlation length, respectively.  $\mu(\mathbf{x})$  is the mass density of the system.

**Fig. 11** Measured X-rays spectrum (black histogram) and simulated background distribution (magenta histogram) in the energy range  $\Delta E = (1000\text{--}3800)$  keV from the germanium detector described in [91]



The nonlinearity is introduced via the  $\langle \mu(\mathbf{x}) \rangle_t$  term. The stochastic noise field  $W_t(t)$  depends on  $r_C$ , with the properties of a white noise in the original formulation of the model.  $dW_t(\mathbf{x})$  are a set a Wiener increments with zero average and correlation  $\mathbb{E}[dW_t(\mathbf{x})dW_t(\mathbf{y})] = dt e^{-\frac{(\mathbf{x}-\mathbf{y})^2}{4r_C^2}}$ . The parameter can effectively tune the dynamics of collapse. For example, for  $r_C \sim 10^{-5}$  cm,  $\lambda \sim 10^{-8 \pm 2}$  s $^{-1}$  gives the boundary between the microscopic and mesoscopic world;  $\lambda \sim 10^{-17}$  s $^{-1}$  is the boundary between the mesoscopic and macroscopic one.

In both models, if the particle undergoing the collapse is charged, the diffusive Brownian-like motion which takes place as a result of the spontaneous collapse implies the emission of radiation. This results in the radiation emission rates:

$$\left. \frac{d\Gamma}{dE} \right|_{\text{DP}} = \frac{2}{3} \frac{G e^2 N^2 N_a}{\pi^{3/2} \epsilon_0 c^3 R_0^3 E}, \quad \left. \frac{d\Gamma}{dE} \right|_{\text{CSL}} = (N^2 + N) N_a \frac{\hbar \lambda}{4\pi^2 \epsilon_0 m_0^2 r_C^2 c^3 E}. \quad (5)$$

Both models predict an emission rate which follows the  $1/E$  dependence. On the left, the variables  $G$ ,  $e$ ,  $\epsilon_0$ , and  $c$  represent the gravitational constant, the charge of an electron, the vacuum permittivity, and the speed of light, respectively. The term  $N_a$  stands for the total number of atoms being considered, while the factor  $N^2$  takes into account the atomic number's quadratic effect on the outcome.  $R_0$  is the size of the particle's mass density, as proposed by Penrose, to be similar to the size of the nucleus' wave function. However,  $R_0$  can also be used as a free variable in the model [21]. On the right,  $r_C$  and  $\lambda$  are the two main parameters: the spatial resolution of collapse and the strength of noise. The term  $(N^2 + N)N_a$  takes into account both the coherent emission from nuclei (accounted for by  $N^2$ ) and the incoherent emission from electrons (accounted for by  $N$ );  $m_0$  represents the reference mass of a nucleon (in mass-proportional CLS model).

### 3.3.1 Quantum collapse, present status and results

At LNGS, collapse models can be strongly constrained, searching for the spontaneous radiation. The extremely low background allows detectors to be sensitive to even the small signal predicted by the models, if it exists.

Using germanium detectors at LNGS, the available parameter space of the DP and CLS models has been severely constrained [21, 91]. The data taken by a coaxial p-type HPGe detector, with active crystal volume of 375 cm $^3$  and shielded by environmental radiation with a copper and lead casing, are shown in Fig. 11. Since no evidence of the signal, which has the shape of a falling distribution as a function of  $E$ , is found, it is possible to exclude at 90% C.L. the available parameter space. The  $(r_C - \lambda)$  plane of the CSL model is progressively reduced, as shown in Fig. 12 in the most up-to-date plot.

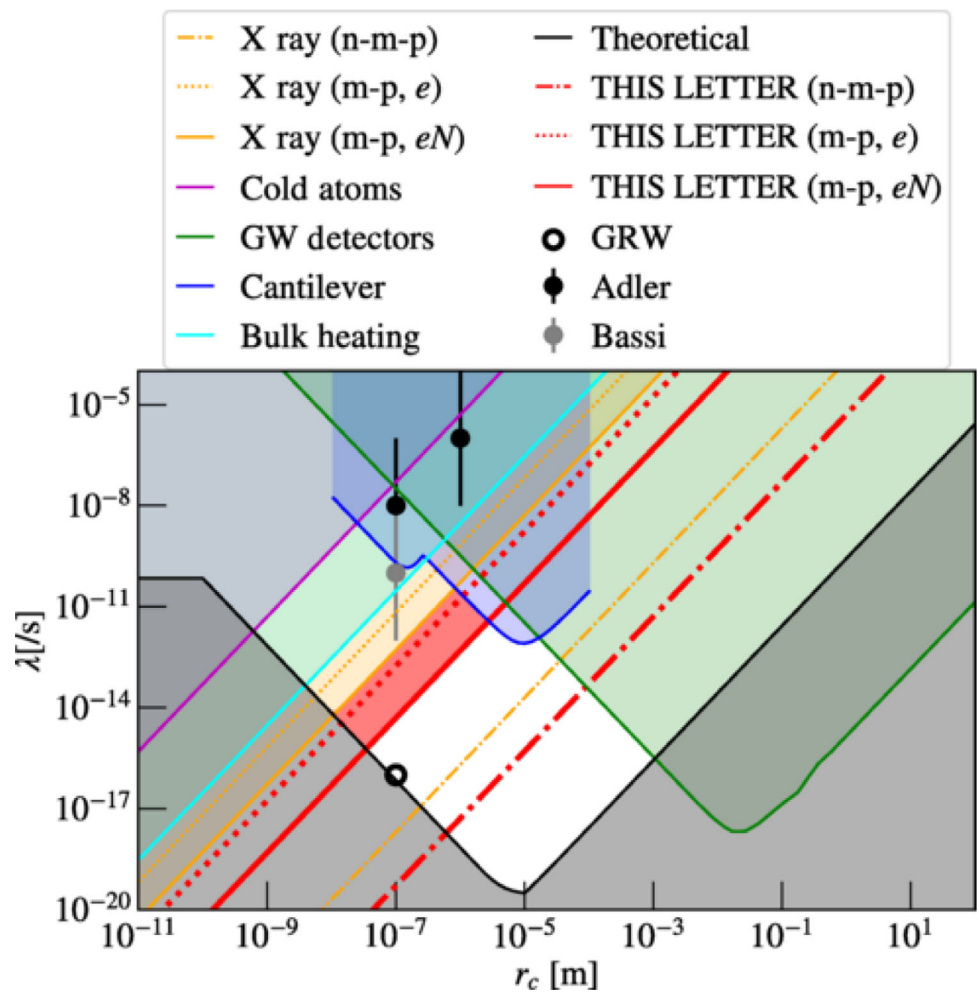
### 3.3.2 Quantum collapse models and their experimental tests future plans

The activities planned for the midterm at LNGS regarding the quantum collapse model and their experimental tests will pave the way to a deeper understanding of the measurement problem, with implication ranging from fundamental physics to quantum technologies. The activities in this subgroup are outlined in Fig. 4, task T3, with time horizon for the next 2, 5 and 8 years from the first quarter of 2023.

*Generalized models, cancellation effects and energy dependence* The first activities of T3 (year 1–year 2) consist of theoretical and phenomenological work on the collapse models, with focus on: generalized models (QC1), cancellation effects (QC2) and energy dependence on the target atomic number (QC3).

The DP model is ruled out in the parameter-free version, however the model can be extended to more general cases. This will be realized in collaboration with the theoretical groups (Diósi, Penrose, Adler, Bassi and others). The following extensions are foreseen:

**Fig. 12** Updated exclusion plot of the  $(r_c - \lambda)$  plane from the MAJORANA DEMONSTRATOR [92]. Solid line and dotted represent the mass-proportional case for quasi-free electrons (m-p,e) and coherent emission from the nuclei (m-p, eN). Dash-dotted line represents the non-mass-proportional (n-m-p) case. The limits come from cold atom experiments (in magenta) [93, 94], the interpretation of gravity wave experiments from LIGO and LISA Pathfinder (in green) [95], measurements using cantilevers where an anomalous result was reported (in blue) [96–98], and the interpretation of heat leaks in low-temperature experiments in terms of the CSL heating effect (in cyan) [99, 100]. The limits from previous x-ray studies at LNGS [91, 101] are represented by orange lines. Additionally, a theoretical lower limit is shown in black, which is based on the idea that a graphene disk with a radius of 10 micrometers (the minimum resolution of the human eye) should be localized in less than 1ms (the minimum time resolution of the human eye) [102]. Some proposed lower bounds by Adler [103], Bassi [104], and Ghirardi, Rimini, and Weber [85] are also shown as black vertical lines, a gray vertical line and a black hollow circle, respectively



- Addition of dissipation terms to the master equation and stochastic nonlinear Schrödinger equation of the DP theory: This addition will mitigate a known criticism on the model, which is the runaway energy increase.
- Inclusion of non-Markovian correlation function.

The extensions of the model are expected to lead to stronger dependence on the energy of the spontaneous radiation, in relation to the atomic structure.

With the present formulation of the models, the spontaneous radiation rate is expressed with Eq. (5). However, in the lower energy regime, the photon wavelength is comparable to the atomic orbits dimensions, and the coherent emission of electrons together with protons leads to cancellation effects; their strength and behavior strongly correlates with the atomic structure. Moreover, due to the different interplay of the models parameters, the DP and CSL models are expected to originate different behaviors at low-energy. This feature will effectively change the phenomenology, which will be dependent on the target atomic number and the model, allowing for a richer and more dedicated optimization of the searches. There will be great advantage with the use of ultra-pure aluminum, silver, gold and lead, each of them exhibiting a different energy dependence at lower energy for the different collapse models.

*Preliminary data taking* The activities from year 3 to year 4 focus on exploiting experimentally what found in the previous ones. The energy dependence will be targeted with a preliminary study of a BEGe detector of around 1 kg of mass. This activity has already been pioneered with a BEGe of smaller mass. Preliminary results of the data taking of this detector are shown in Fig. 13, where the spectrum of 74 days of data taking is shown, together with a CNN output trained to discriminate single-site from multi-site events, the latter contributing to the background. Leveraging machine learning technique is in fact expected to further enhance the physics capability of the detector.

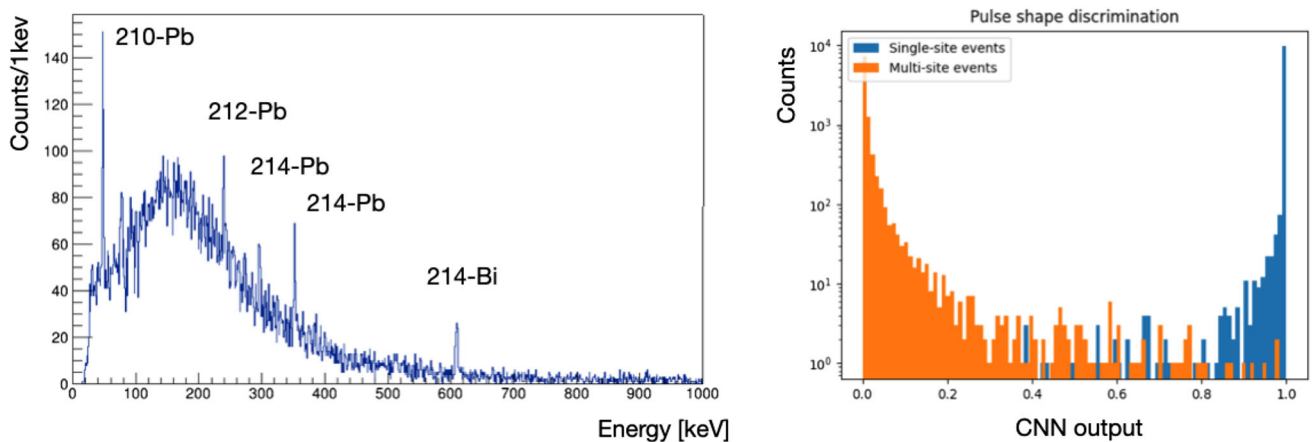


**Fig. 13** Preliminary data from a BEGe devoted to collapse studies. On the left, the data acquired in 74 days in the region 0–1 MeV, where the lines originating from the lead isotopes are indicated. Lead is used as both target and shielding in this setup. On the right, the output of a machine learning approach trained to discriminate signals acquired from the germanium detector into two categories: single-site and multi-site events

In order to exploit a stronger energy dependence on the target material (QC5), lower energies are necessary to fully disentangle the model and atomic number dependence. This will be achieved with an upgrade of the front-end electronics, via a low-noise data acquisition system and a high insulation, low-noise amplifier (QC4).

*Dedicated setup* Finally, from year 5 to year 7 (QC6) a dedicated setup with focus on quantum wave function collapse is planned. To this end, an array of p-type point-contact germanium detectors with the total active crystal mass of more than 10 kg is needed. The setup will have to be equipped with a compact shield and an active muon veto, in order to suppress the environmental and cosmic background. In order to exploit shape dependence, it will need a lower energy threshold, with the possibility of carrying out a data taking campaign with different targets. This last feature (not typically present at deep underground experiments searching for effects beyond the SM) will enable exploiting the atomic mass dependence, and potentially strongly constrain the dissipative and non-Markovian DP and CLS collapse models. Moreover, the setup will be at the same time suited for Dark Matter searches.

#### 4 Direct measurements for nuclear astrophysics

An overview of the INFN-CSN3 activities in Nuclear Astrophysics is presented in [6] and further discussed in the Nuclear Physics Mid Term Plan in Italy of LNL and LNS sessions [10, 11]. In the following sections, a selection of challenging scientific cases debated during the LNGS session [13] are reviewed.

Nuclear Astrophysics is devoted to shed light on the nuclear processes active in stellar environments and Big Bang Nucleosynthesis (BBN). Nuclear Astrophysics studies include the measurement at very low energies of the cross section of nuclear reactions related to various stages of stellar evolution and nucleosynthesis; the study of the neutron induced reactions responsible for the production of the heavy elements in the Universe; the understanding of nuclear processes far from stability (associated with stellar explosions or extreme condition of matter) such as *r*-process, *p*-process and *rp*-process.

In the last decades, huge experimental efforts were devoted to the study of a large number of reactions, using different approaches, that were developed and brought to their best performances. Several projects have been conducted in close cooperation between nuclear physicists and astrophysicists, stimulating further improvements both on the experimental nuclear research side, and on the interpretation of astronomical observations. The main scientific motivations are presented in Sect. 4.1, while the experimental aspects on most relevant cases are discussed in Sect. 4.2. Tables 1 and 2 present a list of key reactions that might be investigated at LNGS and CIRCE laboratories, respectively, in the next 5–10 years, as also shown in Fig. 14.

##### 4.1 Open questions in astrophysics

An impressive advance in the astronomical facilities, those already available, such as the Gaia mission and the new James Webb Space Telescope, and those under development, such as the next generation of large aperture ground-based telescopes like the Extremely Large Telescope, allow more accurate determinations of the physical and the chemical properties of single stars and, more in general, of stellar populations. The exploitation of this huge amount of data requires sophisticated models of stellar evolution and nucleosynthesis, based on extended nuclear networks and very accurate sets of nuclear physics inputs, such as reaction rates.

In this section, a brief overview of different astrophysics scenarios that are influenced by the reactions discussed in the LNGS Session of the Nuclear Physics Mid Term Plan in Italy is presented.

**Table 1** List of the reactions described in previous sections that can be studied at LNGS, along with the machine required the measurement

Reaction	Machine	Upgrade	Phase
D (p, $\gamma$ ) $^3\text{He}$	3.5 MV	None	C
D ( $\alpha$ , $\gamma$ ) $^6\text{Li}$	3.5 MV	None	C
$^3\text{He}(^4\text{He}, \gamma)^7\text{Be}$	3.5 MV	Targets	C
$^{14}\text{N}(p, \gamma)^{15}\text{O}$	400 kV	Detectors	B
$^{14}\text{N}(p, \gamma)^{15}\text{O}$	3.5 MV	None	A
$^{23}\text{Na}(p, \alpha)^{20}\text{Ne}$	400 kV	Detectors	A
$^{27}\text{Al}(p, \alpha)^{24}\text{Mg}$	400 kV	Detectors	A
$^{30}\text{Si}(p, \gamma)^{31}\text{P}$	400 kV	Detectors	C
$^{19}\text{F}(p, \alpha_0, i)^{16}\text{O}$	400 kV	Detectors	B
$^{19}\text{F}(p, \alpha_{2,3,4})^{16}\text{O}$	400 kV	Detectors	B
$^{19}\text{F}(p, \gamma)^{20}\text{Ne}$	400 kV	Detectors	B
$^6\text{Li}(\alpha, \gamma)^{10}\text{B}$	400 kV	Targets	C
$^7\text{Li}(\alpha, \gamma)^{11}\text{B}$	400 kV	Targets	C
$^{10}\text{B}(\alpha, d)^{12}\text{C}$	400 kV	Detectors	C
$^{10}\text{B}(\alpha, p)^{13}\text{C}$	400 kV	Detectors	C
$^{10}\text{B}(\alpha, n)^{13}\text{N}$	400 kV	Detectors	C
$^{11}\text{B}(\alpha, n)^{14}\text{N}$	400 kV	Detectors	C
$^{18}\text{O}(\alpha, \gamma)^{22}\text{Ne}$	3.5 MV	Detectors	B
$^{17}\text{O}(\alpha, \gamma)^{21}\text{Ne}$	3.5 MV	Detectors	B
$^{15}\text{N}(\alpha, \gamma)^{19}\text{F}$	3.5 MV	Detectors	B
$^{14}\text{N}(\alpha, \gamma)^{18}\text{F}$	3.5 MV	Detectors	B
$^{12}\text{C}(\alpha, \gamma)^{16}\text{O}$	3.5 MV	Target and detectors	C
$^{22}\text{Ne}(\alpha, n)^{25}\text{Mg}$	3.5 MV	Gas target	A
$^{22}\text{Ne}(\alpha, \gamma)^{26}\text{Mg}$	3.5 MV	Gas target	B
$^{13}\text{C}(\alpha, n)^{16}\text{O}$	3.5 MV	None	A
$^{12}\text{C} + ^{12}\text{C}$	3.5 MV	Target and detectors	A (gamma)
$^{12}\text{C} + ^{12}\text{C}$	3.5 MV	Target and detectors	C (particles)

The necessary upgrades to the experimental setup and time schedule are indicated: phase A corresponds to the next 2–3 years, phase B to 3–5 years, and phase C to 5–7 years

**Table 2** List of the reactions described in previous sections that can be studied at CIRCE

Reaction	Upgrade/Materials	Phase
$^7\text{Be}(p, \gamma)^8\text{B}$	$^1\text{H}$ Target/80 GBq $^7\text{Be}$	A/B
$^{12}\text{C}(\alpha, \gamma)^{16}\text{O}$	None	A
$^{16}\text{O}(\alpha, \gamma)^{20}\text{Ne}$	None	A/B
$^{14}\text{N}(\alpha, \gamma)^{18}\text{F}$	None	A/B
$^{15}\text{N}(\alpha, \gamma)^{19}\text{F}$	None	A/B
$^7\text{Be}(\alpha, \gamma)^{11}\text{C}$	RMS optics/60 GBq $^7\text{Be}$	C
$^7\text{Be}(d, p)^8\text{Be}$	none/20 GBq $^7\text{Be}$	B
$^7\text{Be}$ Half-life	Windowless post-stripper/ 80 GBq $^7\text{Be}$	A
$^{12}\text{C} + ^{12}\text{C}$	None	B
$^{12}\text{C} + ^{16}\text{O}$	None	B
Triple- $\alpha$	$^3\text{He}$ gas target	C
THM with RMS	Scattering Chamber, Array of DSSSD	C

The necessary upgrades to the experimental setup, main needs and time schedule are indicated: phase A corresponds to the next 2–3 years, phase B to 3–5 years, and phase C to 5–7 years

	Phase A	Phase B	Phase C	
LNGS 400 kV	$^{23}\text{Na}(p,\alpha)^{20}\text{Ne}$ , $^{27}\text{Al}(p,\alpha)^{24}\text{Mg}$	$^{14}\text{N}(p,\gamma)^{15}\text{O}$ , $^{19}\text{F}(p,\alpha)^{16}\text{O}$ , $^{19}\text{F}(p,\gamma)^{16}\text{O}$	$^{30}\text{Si}(p,\gamma)^{31}\text{P}$	H burning
			$^6\text{Li}(\alpha,\gamma)^{10}\text{B}$ , $^7\text{Li}(\alpha,\gamma)^{11}\text{B}$ , $^{10}\text{B}(\alpha,d)^{12}\text{C}$ , $^{10}\text{B}(\alpha,p)^{13}\text{C}$ , $^{10}\text{B}(\alpha,n)^{13}\text{N}$ , $^{11}\text{B}(\alpha,n)^{14}\text{N}$	He burning
LNGS 3.5 MV			$\text{D}(p,\gamma)^3\text{He}$ , $\text{D}(\alpha,\gamma)^6\text{Li}$ , $^3\text{He}(\alpha,\gamma)^7\text{Be}$	BBN
	$^{14}\text{N}(p,\gamma)^{15}\text{O}$			H burning
		$^{14}\text{N}(\alpha,\gamma)^{18}\text{F}$ , $^{15}\text{N}(\alpha,\gamma)^{19}\text{F}$ , $^{16}\text{O}(\alpha,\gamma)^{20}\text{Ne}$ , $^{17}\text{O}(\alpha,\gamma)^{21}\text{Ne}$ , $^{18}\text{O}(\alpha,\gamma)^{22}\text{Ne}$	$^{12}\text{C}(\alpha,\gamma)^{16}\text{O}$	He burning
	$^{13}\text{C}(\alpha,n)^{16}\text{O}$ , $^{22}\text{Ne}(\alpha,n)^{25}\text{Mg}$	$^{22}\text{Ne}(\alpha,\gamma)^{26}\text{Mg}$		neutron sources
		$^{12}\text{C}+^{12}\text{C}$ (particle detection)	C burning	
CIRCE		$^7\text{Be}(d,p)^8\text{Be}$		BBN
	$^7\text{Be}(p,\gamma)^8\text{B}$		$^7\text{Be}(\alpha,\gamma)^{11}\text{C}$	H burning
	$^{12}\text{C}(\alpha,\gamma)^{16}\text{O}$	$^{16}\text{O}(\alpha,\gamma)^{20}\text{Ne}$ , $^{14}\text{N}(\alpha,\gamma)^{18}\text{F}$ , $^{15}\text{N}(\alpha,\gamma)^{19}\text{F}$		He burning
		$^{12}\text{C}+^{12}\text{C}$ , $^{16}\text{O}+^{16}\text{O}$		Advanced burnings
	$^7\text{Be}$ half-life		triple $\alpha$ , THM	more RMS

Fig. 14 GANTT chart of the activities of WG2 for the midterm. Phase A corresponds to the next 2–3 years, phase B to 3–5 years, phase C to 5–7 years

#### 4.1.1 H-burning

Stars burn hydrogen via different sets of nuclear reactions: the proton–proton (p–p) chain and the CNO cycle. The latter is the dominant energy source, and thus of the nucleosynthesis, in stars having mass larger than about  $1.2 M_{\odot}$ . Unlike the p–p chain, the CNO cycle is a catalytic cycle, i.e., it converts 4 protons into one helium nucleus but does so via reactions on the preexisting seed nuclei of carbon, nitrogen and oxygen. Depending on the temperature attained in stellar interiors, different branches of the CNO cycle are active. For instance, at low temperatures ( $T \sim 20$  MK) only the CN cycle works, while at higher energies ( $T \gtrsim 30$  MK) the NO cycle is efficiently active as well. The rate of the CN with respect to the NO cycle depends on the branching ratio of the proton capture on  $^{15}\text{N}$ , i.e., the  $^{15}\text{N}(p,\gamma)^{16}\text{O}$  and  $^{15}\text{N}(p,\alpha)^{12}\text{C}$  reaction cross sections. In all cases, the  $^{14}\text{N}(p,\gamma)^{15}\text{O}$  is the slowest reaction of the cycle and, in turn, it determines the whole H-burning rate. Once central hydrogen has been converted into helium, proton burning continues in a shell surrounding the core. The synthesis of heavier elements, up to Si, can occur through the NeNa and the MgAl cycles, provided that large enough temperatures are attained. A detailed knowledge of the nuclear processes active in these cycles is mandatory to properly determine the nucleosynthesis during the star evolution, in particular in the Red Giant Branch and Asymptotic Giant Branch (AGB) phases, as well as in Novae explosions. The abundances of the synthesized elements critically depend on the rates of the nuclear processes involved, often through non-trivial nucleosynthesis reaction chains, combined with complex mixing mechanisms.

In addition, in extremely metal-poor stars, as the first generation of stars, owing to the scarcity of C, N and O, the H-burning cannot occur through the CNO cycle. In this case, even massive stars burn H only through the p–p chain, but the released nuclear energy is not sufficient to balance the contraction of the core. As a result, the central temperature increases, until the triple- $\alpha$  process is efficiently activated, as will be further discussed in the next Subsection (see also Sect. 4.2.3).

#### 4.1.2 He burning

*Triple- $\alpha$  and the  $A = 5$  and  $A = 8$  gaps* The triple- $\alpha$  reaction, i.e., the fusion of three  $\alpha$  particles into a  $^{12}\text{C}$  nucleus, plays a role in many astrophysical processes. Firstly, it is the main mechanism behind the synthesis of carbon in stellar interiors, essential to the development of life on Earth (at least). Secondly, it is the mechanism by which the first generation of stars, created from the hydrogen and helium ashes of the Big Bang (the so-called population III), was able to bridge the  $A = 5$  and  $A = 8$  mass gaps, thus allowing nucleosynthesis to proceed toward heavier elements. The triple- $\alpha$  reaction proceeds as a two-step process, strongly enhanced by two low-lying s-wave ( $l = 0$ ) resonances,  $\alpha + \alpha \rightarrow ^8\text{Be}(0_1^+)$ ;  $\alpha + ^8\text{Be}(0_1^+) \rightarrow ^{12}\text{C}(0_2^+)$ . In the intermediate-temperature domain (0.1–2 GK), the rate of this important reaction is fully determined by the properties of the Hoyle state in  $^{12}\text{C}$  (7.654 MeV,  $0^+$ ) [105], and, in particular, by the competition between its  $\alpha$  and radiative decays. At the energies corresponding to this temperature range, the reaction cross section cannot be directly measured, and the rate determination relies mainly on measurements of the radiative decay partial width of the Hoyle state [106]. This leads, in turn, to a relatively precise determination of the reaction rate (10%), even

though ambiguities still persist in the experimental findings related to the radiative decay width of the Hoyle state [107]. The latter directly affects the reaction rate, and calls for new experimental investigations.

The determination of the reaction rate is far more complicated in the low- and high-temperature domains, i.e.,  $T < 0.1$  GK and  $T > 2$  GK, respectively. In particular, complex three-body models are necessary to calculate the rate in the low-temperature regime [108, 109]. However, the commonly used evaluation of the reaction rate (NACRE, [110]) assumes that the breakup of the  $^{12}\text{C}$  Hoyle state into three particles proceeds exclusively as a sequential two-step process via the ground state of  $^8\text{Be}$  (SD). In practice, direct decay (DD) into three  $\alpha$ -particles, associated with three-body processes that bypass the formation of the  $^8\text{Be}$  resonance, is neglected. The competition between SD and DD has been for a long time the subject of theoretical and experimental efforts. From a theoretical point of view, the Hoyle state is often described as a cluster state made by three weakly interacting  $\alpha$ -particles, but the peculiarities of this geometrical arrangement, which affect the observed DD branching ratio [111], are still quite debated [111–118]. In spite of the critical importance, the experimental determination of the DD partial width has received relatively little scrutiny until recently [106, 119–123]. Improved high-precision experiments [124–127] have finally allowed to prove the dominance of the SD decay over the DD one, reaching a level of sensitivity that now enables to experimentally test the predictions of microscopic nuclear structure calculations [111]. The existence of a non-vanishing DD partial width for the Hoyle state has a relevance in astrophysics, as it may affect low-temperature triple- $\alpha$  reaction rate and, in turn, the synthesis of C during the H-burning phase of primordial stars. The first stellar generation was probably made of peculiar massive stars. Indeed, owing to the lack of CNO isotopes, the H-burning proceeded in the core of these stars through the p-p chain and, in order to generate enough energy to replace the radiative energy loss, the temperature rises up, until the triple- $\alpha$  reactions starts. Then, the C released by the triple- $\alpha$  activates the CNO cycle, causing the development of a quite extended convective core. A fundamental question arises: is the triple- $\alpha$  reaction the only process in nature that makes it past the gaps at  $A = 5$  and  $8$ ? According to the current stellar nucleosynthesis models, the answer is yes. However, these scenarios include alternative nuclear chains involving reactions such as  $^6\text{Li}(\alpha, \gamma)^{10}\text{B}$ ,  $^7\text{Li}(\alpha, \gamma)^{11}\text{B}$ ,  $^7\text{Be}(\alpha, \gamma)^{11}\text{C}$ ,  $^{10}\text{B}(\alpha, d)^{12}\text{C}$ ,  $^{10}\text{B}(\alpha, p)^{13}\text{C}$ ,  $^{10}\text{B}(\alpha, n)^{13}\text{N}$  and  $^{11}\text{B}(\alpha, d)^{14}\text{N}$ , whose cross sections are barely known at the stellar thermal energies. Their study, although interesting, is beyond the midterm discussed in this paper.

The high-temperature domain is instead interesting for the explosive nucleosynthesis, as it occurs in core-collapse supernovae (SNe) and neutron star mergers. At  $T > 4$  GK, baryons attain a nuclear statistical equilibrium, in which matter photodisintegrates into protons, neutrons and  $\alpha$  particles. Then, as this matter expands and the temperature drops below 3–4 GK, fusions restarts building up heavier nuclei. However, the lack of stable nuclei with  $A = 5$  and  $8$  hampers this process that can be overcome through triple- $\alpha$  reactions. At these high temperatures, the triple- $\alpha$  rate is determined by higher energy states of  $^{12}\text{C}$  and by possible interferences among them. In this respect, the properties (spin, parity and partial widths) of roto-vibrational excitations of the Hoyle state, which are predicted by many cluster models [128–130], are expected to play a role. For example, the possible occurrence of a monopole breathing-mode excitation of the Hoyle state, recently conjectured in [131], is expected to modify the temperature dependence of the triple- $\alpha$  process, and the predicted nucleosynthesis in explosive environments and neutron star mergers. These theoretical findings are yet to be fully confirmed by experimental investigations.

**$^{12}\text{C}(\alpha, \gamma)^{16}\text{O}$ , the Holy Grail** The competition between the triple- $\alpha$  and the  $^{12}\text{C}(\alpha, \gamma)^{16}\text{O}$  reaction determines the relative abundances of C and O left by the He burning. The C/O ratio, which scales inversely with the rate of the  $^{12}\text{C}(\alpha, \gamma)^{16}\text{O}$ , has a profound impact on the more advanced phases of the stellar evolution. For instance, the cooling timescale of C-O white dwarfs is longer in case of higher C/O [132] and the amount of  $^{56}\text{Ni}$  ejected by type Ia SNe is higher in case of a higher C/O ratio [133]. Concerning core-collapse SNe, the C/O ratio left after the He burning affects the chemical composition of the ejecta [134, 135]. Hence, a robust determination of the  $^{12}\text{C}(\alpha, \gamma)^{16}\text{O}$  cross section around 300 keV (with an uncertainty of 15% or better) would boost our understanding of the final fate of stellar evolution. At such low energy, the cross section of this reaction is dominated by ground state captures through two sub-threshold resonances ( $J^\pi = 1^-$  and  $2^+$ ). Interferences with higher energy states and the direct capture (DC) component can substantially affect the cross section. The most accurate estimation of the astrophysical  $S$ -factor, as obtained by means of R-matrix calculations, combines direct and indirect measurements [135] and found an uncertainty of  $\sim 30\%$  at 300 keV.

#### 4.1.3 Neutron sources

The  $^{22}\text{Ne}(\alpha, n)^{25}\text{Mg}$  reaction is the main source of neutrons for the  $s$ -process nucleosynthesis taking place in massive AGB stars,  $M > 4 - 5 M_\odot$  [136], and massive stars,  $M > 10 M_\odot$  [137]. In particular, massive stars are contributing to the nucleosynthesis of the bulk of nuclei in the mass range  $70 < A < 110$  via the *weak s-process* component in the solar system [138]. This would account for most of the copper, gallium and germanium in the Solar System [137]. In principle, the abundance of  $^{22}\text{Ne}$ , i.e., the fuel for the  $s$ -process activation, depends on the stellar metallicity. Indeed, the bulk of the CNO isotopes is converted into  $^{14}\text{N}$  during the H-burning phase, and then to  $^{22}\text{Ne}$  via the  $^{14}\text{N}(\alpha, \gamma)^{18}\text{F}(\beta^+\nu)^{18}\text{O}(\alpha, \gamma)^{22}\text{Ne}$  chain during He burning. Therefore, the amount of  $^{22}\text{Ne}$  available for the  $s$ -process in the stellar core should be more than the 60% of the initial metallicity of the star [139, 140]. In this framework, the contribution of massive stars to the production of  $s$ -process elements is expected to decrease with decreasing the initial stellar metallicity [141, 142]. However, for fast-rotating massive stars the amount of  $^{22}\text{Ne}$  can be boosted by mixing induced by rotational instabilities, such as meridional circulation or shear (in case of differential rotation). In this case, the main source of  $^{22}\text{Ne}$

becomes the  $^{12}\text{C}$  made during He burning, by the triple- $\alpha$  reaction, and the resulting  $s$ -process production is significantly enhanced [143]. The relevance of the  $s$ -process from fast-rotating massive stars in the galactic chemical evolution is matter of current research [144, 145]. Recent nucleosynthesis calculation in rotating massive stars [146] has shown that they may contribute significantly to the weak  $s$ -process down to a metallicity  $[\text{Fe}/\text{H}] \sim -1.5$ . Anyway, a precise evaluation of the  $^{22}\text{Ne}(\alpha, n)^{25}\text{Mg}$  reaction rate is mandatory to understand the synthesis of various elements, such as Se, Ge, As and Sb, and to distinguish between different scenarios for the  $s$ -process in massive stars. Furthermore, this reaction affects the magnesium isotopic ratio  $^{24}\text{Mg}/^{25}\text{Mg}/^{26}\text{Mg}$  in the material ejected to the interstellar medium by massive AGB and/or massive stars. Currently, both kind of objects are the proposed polluters of the second generation of stars observed in many globular clusters, which show chemical anomalies in terms of O-Na and Al-Mg abundance anticorrelations [see, e.g., 147]. In this context, an important player is the concurrent reaction  $^{22}\text{Ne}(\alpha, \gamma)^{26}\text{Mg}$ . Indeed, at high temperature most of the  $^{22}\text{Ne}$  is burned through the  $(\alpha, n)$  channel, while the  $(\alpha, \gamma)$  dominates at low temperatures, being the former hampered by the neutron threshold. Note that the minimum temperature for the  $(\alpha, n)$  activation depends on many nuclear resonances in the  $^{26}\text{Mg}$  compound nucleus. The magnesium isotopic ratio is one of the few elemental isotopic ratios which can be measured directly in stars and the interstellar medium with modern astronomical facilities. Therefore, the feedback between Mg isotopic ratio measurements in stars and the interstellar medium and the improvement of the  $^{22}\text{Ne}(\alpha, n)^{25}\text{Mg}$  and  $^{22}\text{Ne}(\alpha, \gamma)^{26}\text{Mg}$  reaction rates certainly will enlighten the puzzle of the origin of abundance anomalies in globular cluster as well as the contribution of massive stars to the synthesis of beyond-iron-peak elements.

On the other hand, the *main s-process* component, which is mainly responsible for the nucleosynthesis of nuclei with mass  $90 < A < 210$ , is efficiently active in low-mass AGB stars ( $1.5 < M/M_{\odot} < 3$ ) [138]. In this case, the main neutron source is the  $^{13}\text{C}(\alpha, n)^{16}\text{O}$  reaction, while the  $^{22}\text{Ne}(\alpha, n)^{25}\text{Mg}$  plays a secondary role [148–150]. The former reaction is indeed active at rather low temperatures (about 90–100 MK) and generates a low neutron density (about  $10^7$  neutrons per  $\text{cm}^{-3}$ ) but for a long time (up to  $10^5$  yr), thus providing a sufficiently high neutron exposure, as needed to produce the heavier  $s$ -process elements, from Sr to Pb. In practice, an AGB star undergoes recurrent He-shell flashes, called thermal pulses (TP), which are thermonuclear runaways whose power attains a few  $10^8 L_{\odot}$ . Then, a dredge-up episode may occur after a TP, when the external layers expand and cool down, until the H-burning shell eventually dies, and the external convection can penetrate the He- and C-rich mantle. According to the standard paradigm, a partial mixing occurring at the bottom of the convective envelope at the time of the dredge-up leaves a thin pocket where the H mass fraction is  $X_H < 0.01$ , while the carbon mass fraction is about 0.2. Then, at the H re-ignition, a substantial amount of  $^{13}\text{C}$  is produced by the  $^{12}\text{C}(p, \gamma)^{13}\text{N}$  reaction followed by the  $^{13}\text{N}$  decay, and, later on, the  $s$ -process can start, due to the activation of the  $^{13}\text{C}$  neutron source. A second neutron burst, as due to the activation of the  $^{22}\text{Ne}(\alpha, n)^{25}\text{Mg}$  reaction, may eventually occur at the bottom of the convective shell powered by a TP, but only if the temperature exceeds 300 MK.

#### 4.1.4 Carbon and oxygen burnings

The C burning phase is triggered by the  $^{12}\text{C} + ^{12}\text{C}$  reaction, whose main channels release protons and  $\alpha$  particles that react with various isotopes, from C to Si, so that a rich nucleosynthesis arises. Below 2.3 MeV, the cross section of this reaction is largely debated. Contrasting scenarios are possible:  $\alpha$ -clusters and molecular states in the  $^{24}\text{Mg}$  compound nucleus could substantially enhance the cross section [151], while fusion hindrance could depress it [152]. Anyway, the cross section between 1.5 and 2 MeV determines the astrophysical reaction rate and, in turn, the temperature of the C burning. This uncertainty has profound consequences in our understanding the late phase of massive stars evolution, i.e., the progenitors of core-collapse SNe [153], and the carbon-simmering phase preceding the dynamical breakout in type Ia SNe progenitors [154].

In massive stars, the C burning rate affects the number, the extension and the duration of the C convective shells and, in turn, it determines the final mass-to-radius relation or, equivalently, the structural compactness at the onset of the core collapse. This parameter plays a key role in understanding the final fate of a massive star. In particular, it determines: i) if the initial implosion is converted into an explosion or a full collapse takes place, directly or after a fallback; ii) if the remnant will be a neutron star or a black hole; iii) the “islands” of explosibility, i.e., the initial mass ranges for which the explosion is possible; and iv) the relative abundances of intermediate-mass nuclei in the SNe ejecta.

The  $^{12}\text{C} + ^{12}\text{C}$  reaction rate also determines the minimum stellar mass that undergoes a C burning phase [155]. Stars whose initial mass is below this threshold skip the C burning phase and directly enter the AGB phase, ending their live as C–O white dwarfs. Stars with mass slightly larger than this threshold will ignite C in a degenerate core and, later on, enter the super-AGB phase. Their final fate may be the development of an O–Ne white dwarf or an electron capture SN. Therefore, the knowledge of this mass limit is of paramount importance in modern astrophysics.

In type Ia SNe, a thermonuclear explosion follows a hydrostatic C burning phase, called simmering. The rate of the C burning during the simmering, which is controlled by the  $^{12}\text{C} + ^{12}\text{C}$  reaction, determines the physical and the chemical structure of the exploding white dwarfs, namely the temperature and the density profiles, as well as the degree of neutronization (see [156] and references therein). Concerning the explosive phase, the anomalous Ca/S and Ar/S mass ratios observed in type Ia SNe remnants suggest a substantial reduction (by a factor of 10) of the current estimates of the  $^{12}\text{C} + ^{16}\text{O}$  reaction rate or, alternatively, a combined variation of the rates of  $^{12}\text{C} + ^{12}\text{C}$ ,  $^{12}\text{C} + ^{16}\text{O}$ ,  $^{16}\text{O} + ^{16}\text{O}$  and the  $^{16}\text{O}(\gamma, \alpha)^{12}\text{C}$  [157]. This occurrence has important implications for the whole nucleosynthesis of Chandrasekhar and sub-Chandrasekhar mass SNe Ia explosions. The relative mass fraction of Ca to S also hints to a metallicity dependent yield during explosive oxygen burning. This ratio depends on the quantity of  $\alpha$  particles:



O burning can proceed through an  $\alpha$ -poor or an  $\alpha$ -rich branch. The  $\alpha$ -rich explosive O burning enhances the production of Ca with respect to S. The  $^{16}\text{O}(p, \alpha)^{13}\text{N}$  reaction, followed by  $^{13}\text{N}(\gamma, p)^{12}\text{C}$ , has been identified as the origin of the metallicity dependence. This reaction chain boosts  $\alpha$ -rich oxygen burning when the proton abundance is large, increasing the synthesis of Ar and Ca with respect to S and Si. At high  $Z$  the presence of free neutrons leads to a drop of the proton abundance and the above chain is not efficient. Moreover, an increase of the rate of this reaction by a factor of approximately 7 with respect to the usual tabulated values (e.g., REACLIB) would be enough to explain all the measured Ca/S mass ratios in the Milky Way and Large Magellanic Cloud SN remnants. Cross section measurements for the  $^{16}\text{O}(p, \alpha)^{13}\text{N}$ , within the Gamow peak for temperatures in the range  $3\text{--}5 \times 10^9\text{K}$ , are encouraged, as it is critical to elucidate the impact of this reaction on the synthesis of Ca in thermonuclear SNe.

#### 4.2 Challenges for nuclear physics: underground and recoil mass separator measurements

Stellar nucleosynthesis is driven by charged particle interactions that, due to the relatively low temperatures in stellar environments, occur at very low energies. The structures of the compound nuclei are often characterized by the single particle and cluster configurations, as well as possible Coulomb and quantum effects near the threshold. In the absence of direct reaction measurements, complementary information from indirect transfer or other reaction techniques helps to understand these configurations. Extrapolations from high-energy experimental data, by means of physical or phenomenological nuclear models, to energies of astrophysical interest have been developed reaching the so-called Gamow Peak [105], but often result in large reaction rate uncertainties. There is, therefore, the need to push direct measurements to lower and lower energies. However, most cross sections are too small to be directly measured in the laboratory at these energies. This is because, in a stellar environment, the energy available to the nuclei is much lower than the Coulomb barrier and nuclear reactions proceed via quantum tunneling. The main challenge in direct measurements comes from the background signals, which, together with the low yields, set a limit to the energy range that can be investigated. Cosmic rays, environmental radioactivity, and beam-induced background reactions on target impurities all represent major limitations to the measurement of cross sections down to the Gamow Peak. Different experimental approaches can be used to maximize signal to background in the measurement of cross sections at very low energies.

One approach is the exploitation of the extremely low background at LNGS, as was first proposed by the LUNA Collaboration. The LUNA experiments have established underground nuclear physics as a powerful tool for determining nuclear reaction rates at Gamow peak energies (which represents the energies where most of the reactions take place in the interior of a star at a given temperature), during thirty years of continuous refinement of the experimental procedures. Over the last few years, several reactions belonging to the CNO, MgAl and NeNa cycles have been studied by the LUNA Collaboration, using the LUNA 400 kV accelerator, a Singletron accelerator which has been installed in year 2000 [16]. These studies have contributed to unveil the origin of some meteoric stardust [158] and to shed light on the speed at which the NeNa cycle operates [159, 160]. It was also measured, with high precision, the cross section of the most important reaction affecting the BBN, i.e.,  $\text{D}(p, \gamma)^3\text{He}$ . LUNA results have contributed to precisely establish one of most uncertain nuclear physics input to BBN calculations leading to an accurate determination of the density of baryonic matter [161]. More recently, thanks to the intense He beam available, it was measured for the first time the rate of the most important stellar neutron source, the  $^{13}\text{C}(\alpha, n)^{16}\text{O}$  reaction, directly inside the Gamow peak [162], thus improving our understanding of the branch points along the  $s$ -process [162].

A second possible approach is the use of more complex experimental apparatuses to maximize signal to background through high selectivity and larger detection efficiency. An example is provided by RMSs that allow to measure the cross section of radiative capture reactions by means of the detection of the residual nucleus, without the need of  $\gamma$ -ray measurements, that can be optionally performed in order to gain additional information on the nuclear process. The ERNA RMS is one of the few recoil separators devoted to the measurement of nuclear cross section of astrophysical interest. In the early 2000s, the ERNA RMS was realized at the 4MV Dynamitron Tandem Laboratorium of the Ruhr-Universität Bochum (Germany) [34, 163–166], with the aim of studying the  $^{12}\text{C}(\alpha, \gamma)^{16}\text{O}$  reaction. In 2009, the ERNA RMS was moved to the Tandem Accelerator Laboratory of CIRCE, and its updated layout is shown in Fig. 3.

The ERNA RMS so far has provided data on several processes of astrophysical relevance. The first results were obtained from the measurement of the total cross section of the  $^{12}\text{C}(\alpha, \gamma)^{16}\text{O}$  reaction [167]. It was possible to get a new insight on the relevance of the cascade transitions that were later investigated by DRAGON [168] and ERNA [169]. The use of ERNA RMS for the measurement of the  $^3\text{He}(\alpha, \gamma)^7\text{Be}$  reaction cross section gives an important contribution to solve the then long-standing issue of the difference between extrapolation based on experiments selection according to the measurement method [170].

The ERNA RMS was used to measure the resonances in the  $^{15}\text{N}(\alpha, \gamma)^{19}\text{F}$  reaction at  $E_{c.m.} = 1323$  and 1487 keV. The reaction was studied in inverse kinematics, using a  $^{15}\text{N}$  beam [171] on a windowless extended  $^4\text{He}$  target [172]. More recently, the ERNA Collaboration completed the measurement of the  $^7\text{Be}(p, \gamma)^8\text{B}$  total cross section in the energy range  $E_{c.m.} = 367.2\text{--}812.2$  keV [173, 174] using a windowless gas target [31] and the radioactive  $^7\text{Be}$  beam available at CIRCE with intensities up to  $10^9$  pps [30].

The ERNA Collaboration also performed at CIRCE measurements of the  $^{12}\text{C} + ^{12}\text{C}$  cross section using the array of GASTLY detectors [35] at backward angles. The GASTLY detectors allowed for unambiguous identification of both protons and alpha particles of  $^{12}\text{C} + ^{12}\text{C}$  [175]

#### 4.2.1 Big Bang Nucleosynthesis

**$D(p, \gamma)^3\text{He}$  and  $D(\alpha, \gamma)^6\text{Li}$**  Deuterium (D) is an excellent indicator of cosmological parameters in the early Universe because its primordial abundance is the most sensitive to the baryon density of the Universe. Although astronomical observations of primordial deuterium abundance reached percent accuracy [176], theoretical predictions [177, 178] based on BBN were hampered by large uncertainties on the cross section of the deuterium burning reaction  $D(p, \gamma)^3\text{He}$ .

A recent measurement at the LUNA 400 kV accelerator reached 3% accuracy in the energy range  $E_{c.m.} = 33\text{--}263$  keV [161] that provided remarkable boost to these studies: a BBN estimates of the baryon density at the 1.6% level has become possible, now in excellent agreement with cosmic microwave background analyses. However, the maximum achievable beam energy (400keV) did not allow to completely explore the energy range relevant for BBN that extends up to  $E_{c.m.} = 369$  keV for 95% coverage. The BIBF is perfectly suited to extend precision measurements in the energy range of interest up to  $E = 1.5$  MeV using an approach similar to the one used in [161], with a windowless gas target [179]. Given the high  $Q$  value of the reaction (5.5MeV) the photons are emitted with an energy where the background suppression in  $\gamma$ -ray spectra is most effective in an underground laboratory. In addition to the important cosmological implications, precise measurements of the angular distribution and of the cross section over a broad energy range are relevant to test nuclear physics models. In fact, the  $D(p, \gamma)^3\text{He}$  reaction cross section has been calculated within a microscopic *ab-initio* approach, i.e., using realistic models for the nuclear interactions and currents, and applying numerical techniques able to calculate the bound- and scattering-state wave functions, including the Coulomb interaction without approximation (see refs. [180–182]), and a comparison with precise experimental data would be very helpful.

Another important reaction contributing to BBN is the  $D(\alpha, \gamma)^6\text{Li}$  responsible for the production of the  $^6\text{Li}$  isotope. Its cross section has been measured around 130keV with the LUNA 400 kV accelerator [183, 184]. It was the first direct measurement in the BBN energy range. Coulomb dissociation experiments provided only upper limits [185, 186]. The BIBF 3.5 MV accelerator offers the possibility to extend the measurements up to  $E_{c.m.} = 1.2$  MeV, by using an  $\alpha$  beam in the 0.2–3.5MeV range and a deuterium gas target to fully cover the BBN energy range.

##### **$^3\text{He}(\alpha, \gamma)^7\text{Be}$**

The  $^3\text{He}(\alpha, \gamma)^7\text{Be}$  reaction plays an important role in the production of  $^7\text{Li}$  during BBN ( $E = 160\text{--}380$  keV) and is also crucial for the hydrogen burning in low-mass stars.

Due to its very low cross section, the  $^3\text{He}(\alpha, \gamma)^7\text{Be}$  reaction cannot be measured directly at solar energies and the data relies on high-energy data extrapolations using different theoretical calculations. A recent theoretical work [187] showed that the angular distribution of the  $^3\text{He}(\alpha, \gamma)^7\text{Be}$   $S$ -factor is directly correlated to the extrapolated astrophysical  $S$ -factor at solar energies. To better constrain the extrapolations down to solar energies, experimental data which connect the BBN range data [27] with higher energy data [188] is still missing. A new high-energy measurement might be performed at the BIBF 3.5 MV accelerator using a gas target setup similar to the one used in [189] in combination with a large (140%) HPGe.

**$^7\text{Be}(d, p)^8\text{Be}$  reaction via THM at BBN energies** The quest of a nuclear solution to the long-standing cosmological lithium problem is matter of debate and research in nuclear astrophysics [190–192]. Indeed, while BBN nicely describes  $^2\text{H}$ ,  $^3\text{He}$  and  $^4\text{He}$  primordial abundances in connection with the most recent astronomical observations, it fails in predicting the  $^7\text{Li}$  ones being these a factor  $\sim 2\text{--}3$  larger with respect the observed ones in halo stars, as discussed in [193]. Besides the solutions provided by cosmology and stellar physics, nuclear physics solutions have been also investigated in recent years in order to constrain the processes affecting the nucleosynthesis of  $^7\text{Li}$ . For instance, the Trojan Horse method (THM, see, e.g., [194, and references therein]) was applied to study the  $^7\text{Be}+n$  induced reactions, opening the new frontier of applying THM on reactions in which unstable nuclei and neutrons are involved. In detail, the  $^7\text{Be}(n, \alpha)^4\text{He}$  THM measurement [195, 196] was performed at the EXOTIC facility at LNL [10, 197], while a subsequent measurement [198] allowed to investigate also the competing  $^7\text{Be}(n, p)^7\text{Li}$  channel via a devoted experiment performed at CRIB-Riken in which both  $p_0$  and  $p_1$  exit channels have been measured.

In order to further investigate the impact of nuclear reactions involving the unstable  $^7\text{Be}$ -isotope, a further channel to be investigated is the  $^7\text{Be}(d, p)^8\text{Be}$  because of its role in depleting  $^7\text{Be}$  nuclei during BBN by populating several  $^8\text{Be}$  excited states in the exit channel as given in [199].

However, direct cross section measurements partially cover the BBN energy region (i.e., energies  $\approx 100\text{--}300$  keV), thus requiring additional investigations via indirect techniques.

For such a reason, THM could be applied to the quasi-free  $^6\text{Li}(^7\text{Be}, p^8\text{Be})^4\text{He}$  breakup reaction by using the LNS THM group know-how and a 7–9 MeV  $^7\text{Be}$  beam, available at the CIRCE laboratory, impinging on a  $^6\text{LiF}$  target, evaporated on a C-backing. Indeed,  $^6\text{Li}$  represents a suitable TH nucleus because of its marked  $\alpha+d$  structure, its relative low binding energy,  $\sim 1.47$  MeV, and its well-known momentum distribution for the  $\alpha$ - $d$  intercluster motion occurring in  $s$ -wave [194].

#### 4.2.2 Hydrogen burning

##### **$^7\text{Be}(p, \gamma)^8\text{B}$**

The reaction  $^7\text{Be}(p, \gamma)^8\text{B}$  plays an important role in the Sun, where it determines the high-energy component of the solar neutrino spectrum. The importance of this reaction triggered several experiments over the last decades. Recently, the ERNA Collaboration

measured for the first time, with adequate precision the cross section of  ${}^7\text{Be}(p, \gamma){}^8\text{B}$  using the a radioactive  ${}^7\text{Be}$  beam and a RMS in the energy range from  $E_{c.m.} = 367\text{--}812$  keV [173, 174]. A combined analysis of their results produces an overall consistent picture for the energy dependence of the cross section, while an inflation of the quoted uncertainties is needed to accommodate the observed discrepancy in the absolute scale of the different data sets [174, 200]. It is important to note that in the energy range above  $E_{c.m.} = 1$  MeV the different data sets and theoretical models show the greatest discrepancy. The available direct measurements data, in this energy range, are all obtained in direct kinematics, with a proton beam on a  ${}^7\text{Be}$  target [200, 201]. A completely new measurement, performed in inverse kinematics, with a  ${}^7\text{Be}$  beam impinging on a proton target, using the ERNA RMS, will help shed light on the origin of the discrepancy and the selection of a more accurate theoretical extrapolation model. Recently, the accelerator terminal has been equipped with a solid stripper system that leads to an increase in the probability of higher charge states and then more intense  ${}^7\text{Be}$  beams at high energy. This opens the possibility to measure with the RMS the cross section up to  $E_{c.m.} = 1.3$  MeV. A new extended hydrogen gas target, with reduced dimension respect the one used in the lower energy range, is necessary to optimize the energy and angular acceptance of the ERNA RMS. Considering an average  ${}^7\text{Be}$  beam current of  $\approx 10^8$  pps, to perform the measurements in the energy range  $E_{c.m.} = 0.8\text{--}1.3$  MeV will be needed about 80 GBq of  ${}^7\text{Be}$  to produce the cathodes and 8 weeks measurement time.

#### ${}^{14}\text{N}(p, \gamma){}^{15}\text{O}$

As already mentioned, the reaction  ${}^{14}\text{N}(p, \gamma){}^{15}\text{O}$  plays a fundamental role in the CNO cycle of stellar hydrogen burning and has strong impact in various other astrophysical phenomena [202], being the bottle-neck of the cycle. An extrapolation to the astrophysical relevant energies requires its cross section to be known with high precision over a wider energy range. Recent experiments exhibit some contradictions [203–206]; this emphasizes the need for a new, high-precision measurement of the  ${}^{14}\text{N}(p, \gamma){}^{15}\text{O}$  cross section. The energy range of BIBF 3.5 MV accelerator, is perfectly suited to address these emerging inconsistencies.

Preparations for the experiments at the BIBF are already ongoing. A first setup will use a single  $\gamma$ -ray detector, readily available at LUNA, and can then be extended to a multi-detector setup for angular distribution experiments. Different options of target preparation are investigated, including implanted and sputtered solid state targets. For the high proton energies and intensities, beam-induced background and target stability are crucial issues.

Additionally, a further study of the  ${}^{14}\text{N}(p, \gamma){}^{15}\text{O}$  at the LUNA 400 kV accelerator is highly desirable, to measure the cross section at energies above and below the well-known resonance at  $E_{c.m.} = 259$  keV [207]. In particular, cross section data with branching ratios for the decay of  ${}^{15}\text{O}$  at energies below the resonance have large uncertainties [208]. The use of a new scintillation detector with high efficiency and granularity, currently under planning at LUNA, would allow to reach the ambitious goal of measuring the  ${}^{14}\text{N}(p, \gamma){}^{15}\text{O}$  total and partial cross sections down to very low energies. The principle of using a segmented summing detector to reconstruct the branching ratios has been already studied by the LUNA Collaboration [20, 159].

#### ${}^{19}\text{F}(p, \alpha_0){}^{16}\text{O}$ , ${}^{19}\text{F}(p, \alpha_{2,3,4}){}^{16}\text{O}$ , ${}^{19}\text{F}(p, \gamma){}^{16}\text{O}$

The galactic abundance of  ${}^{19}\text{F}$  is a long-standing puzzle in nuclear astrophysics. The dominant  ${}^{19}\text{F}(p, \alpha_0){}^{16}\text{O}$  channel has been studied at energies below 400 keV (of interest for AGB star nucleosynthesis) via direct and indirect measurements [209, 210] with results in qualitative agreement. However, a recent review paper [211] reported a disagreement between aforementioned data and old results [212]. The  ${}^{19}\text{F}(p, \alpha_1){}^{16}\text{O}$  reaction is expected to have a negligible contribution to the total reaction rate [211]. In a recent work [213], however, the crucial impact on the  ${}^{19}\text{F}(p, \alpha_1){}^{16}\text{O}$  reaction  $S(E)$  of the elusive resonance at  $E_{c.m.} \sim 206$  keV (corresponding to  $E_x = 13095$  keV) was clearly pointed out, demanding experimental efforts, especially at unexplored astrophysical energies. At the Jinping Underground Nuclear Astrophysics (JUNA) laboratory recently was measured for the first time the  ${}^{19}\text{F}(p, \alpha_{2,3,4}){}^{16}\text{O}$  reaction  $S(E)$  down to  $E_{c.m.} = 72.4$  keV [214], with a significant difference with respect to a previous measurement performed down to  $E_p = 200$  keV, that was leading to a quite different extrapolation, thus new independent data would help in settling the discrepancy.

The  $(p, \gamma)$  channel investigation is severely hampered by the huge background produced by the  $(p, \alpha\gamma)$  reaction. Another measurement performed at JUNA, however, recently reported new  $S$ -factor data down to  $E \sim 180$  keV, resulting in an increase of the rate of this reaction by almost an order of magnitude [215]. Given the significant impact of such results on our understanding of observed abundances in population III stars [216] together with the fact that we still need to rely on extrapolation at Gamow energies, a new measurement is required to confirm and possibly improve the JUNA results.

Given the high-intensity beam of LUNA 400 kV, it is crucial to investigate the optimal target among the many options available in literature. For the  $\alpha$  detection, the setup designed for the  ${}^{23}\text{Na}(p, \alpha){}^{20}\text{Ne}$  reaction might be used with minor changes, see below. The particle detection system will be coupled with 2 CeBr<sub>3</sub> scintillators and a HPGe detector in forward geometry to measure the prompt  $\gamma$ -rays produced by the  $(p, \alpha)$  channel. Coincidence measurements between  $\alpha$  particles and  $\gamma$ -rays will improve the discrimination between the different  $\alpha$  groups. A second campaign will focus on the  $(p, \alpha_1)$  and the  $(p, \gamma)$  channels, and it would be performed with a high-efficiency segmented  $4\pi$  scintillator detector, placed all around the target chamber. The  ${}^{19}\text{F}(p, \alpha_1){}^{16}\text{O}$  reaction, indeed, populates the  $0^+$  state at  $E_x = 6049$  keV in  ${}^{16}\text{O}$ , which de-excites via  $e^-e^+$  pair production. The emitted positron quickly annihilates producing two photons of 511 keV energy each in opposite directions, which will be detected in coincidences by two opposite crystals of the clover scintillator. In the study of the of the  ${}^{19}\text{F}(p, \gamma){}^{20}\text{Ne}$  reaction, one of the major challenges is the background due to the concurrent  $(p, \alpha)$  channel, its identification would benefit of a highly segmented detector.

### $^{23}\text{Na}(p, \alpha)^{20}\text{Ne}$ , $^{27}\text{Al}(p, \alpha)^{24}\text{Mg}$

The  $^{23}\text{Na}(p, \alpha)^{20}\text{Ne}$  and  $^{27}\text{Al}(p, \alpha)^{24}\text{Mg}$  reactions belong to the NeNa and MgAl cycles, respectively, active during H-burning when the temperature exceeds  $\sim 50$  MK. In particular, over the temperature range relevant for hot-bottom burning in the final stages of intermediate-mass stars ( $M \approx 4$  to  $8M_{\odot}$ ), and for core and shell-hydrogen burning in massive stars ( $M \geq 8M_{\odot}$ ), the  $^{23}\text{Na}(p, \alpha)^{20}\text{Ne}$  appears [217] to totally dominate the  $^{23}\text{Na}$  destruction due to proton capture. As such, its rate is key to evaluate how much Na is synthesized in stars and subsequently ejected in the interstellar medium by means of *winds* and/or SNe explosions.

One of the most debated issues in modern astrophysics is the origin of the peculiar chemical patterns observed in Globular Clusters, gravitationally bound groups of very old stars ( $\approx 12$ – $13$  Gyr), whose ages set a lower limit to the age of our Universe. Understanding the chemical characteristics of Globular Clusters can provide us with the key to understanding the formation of our Galaxy from the epochs of the early Universe until today. Of particular interest in recent years has been the so-called oxygen-sodium (O-Na) anti-correlation [218], i.e., a strong sodium enhancement when oxygen is heavily depleted. Therefore, having a precise measurement of the  $^{23}\text{Na}(p, \alpha)^{20}\text{Ne}$  rate is important for testing the plausibility of the various hypotheses suggested so far [219–221].

The  $^{27}\text{Al}(p, \alpha)^{24}\text{Mg}$  reaction is also active in stellar interiors during the hydrogen burning stages and significantly affects the abundances of Mg and Al isotopes. Current uncertainties do not allow an unambiguous conclusion about the existence of a MgAl cycle, for example, according to present knowledge at temperatures  $T < 50$  MK the ratio of the cross section of the  $(p, \gamma)$  and the  $(p, \alpha)$  channels ranges from about 0.01 to 1000 [222] due to a number of key nuclear resonances for which only upper limits exist [223].

In the framework of the ELDAR ERC starting grant,<sup>2</sup> a new measurements of the  $^{23}\text{Na}(p, \alpha)^{20}\text{Ne}$  and  $^{27}\text{Al}(p, \alpha)^{24}\text{Mg}$  reactions are already planned. A new charged particle detection setup specifically designed and built for underground in beam charged particle spectroscopy will be mounted at the LUNA 400 kV accelerator.

For the  $^{23}\text{Na}(p, \alpha)$  reaction, the solid target will likely be a tantalum-backed target of the type used and tested in [160] at LUNA. Alpha particles will be detected at backward angles by an array of silicon detectors, shielded by thin aluminized Mylar foils from the flux of recoiling beam protons. Tests are underway to employ neutron transmutation-doped (nTD) silicon detectors to identify and discriminate charged particles via pulse shape discrimination without the need of a  $\Delta E$ - $E$  telescope or similar arrangements that would cause a larger energy degradation. For light particles, this type of detectors has already been shown to be capable of particle identification at higher energies compared to those expected for this experiment [224]. Particle identification would further reduce the background and help identifying the alpha signal of interest.

### $^{30}\text{Si}(p, \gamma)^{31}\text{P}$

An underground measurement of the  $^{30}\text{Si}(p, \gamma)^{31}\text{P}$  reaction would represent a fundamental piece of knowledge to solve the Globular Cluster abundance anomalies puzzle. Knowledge on the cross section of this reaction for astrophysical scenarios is sorely lacking and a measurement of the  $^{30}\text{Si}(p, \gamma)^{31}\text{P}$  reaction ( $Q = 7297$  keV) would be possible at the LUNA 400 kV accelerator. The high intensity and the possibility of beam-induced background issues require a dedicated study to find the best target and eventually the optimal experimental strategy.

Because of the low rate expected, particularly at low energies, a high-efficiency  $4\pi$  scintillator detector should be used, combined with light (Al) target chamber and holder, and with a properly designed shielding to further reduce the residual background.

#### 4.2.3 Hydrogen burning in extremely metal-poor stars

### $^6\text{Li}(\alpha, \gamma)^{10}\text{B}$ , $^7\text{Li}(\alpha, \gamma)^{11}\text{B}$ , $^{10}\text{B}(\alpha, d)^{12}\text{C}$ , $^{10}\text{B}(\alpha, p)^{13}\text{C}$ , $^{10}\text{B}(\alpha, n)^{13}\text{N}$

The importance of these reactions has been discussed in Sect. 4.1.2. The strong background reduction in underground and the intense  $\alpha$ -beam available at the LUNA 400 kV accelerator allow to study the  $^{10,11}\text{B}+\alpha$  and  $^6,7\text{Li}+\alpha$  reactions at the most relevant energies, i.e.,  $E_{c.m.} \gtrsim 100$  keV. Specifically, we plan to investigate the  $^{10}\text{B}(\alpha, p)$ ,  $(\alpha, d)$  and  $(\alpha, n)$  using a combined detection system for charged particles and neutrons. Separate measurements will be done for the  $^6,7\text{Li}(\alpha, \gamma)^{10,11}\text{B}$  radiative captures. These studies will serve to address the contribution and location of broad and interfering resonances in the compound systems, as well as DC transitions with the intent of reduce reaction rate uncertainties.

Count-rate estimates on the basis of present knowledge suggest a data taking time of about 2 weeks per reaction. Estimates are calculated on the basis of  $R$ -matrix extrapolations of existing  $S$ -factor data, assuming  $200 \mu\text{A}$   $\alpha$ -beam current,  $2 \times 10^8$  atoms/cm<sup>2</sup> active nuclei in the target, a 10% (20%) detection efficiency for charged particles (neutrons).

### $^7\text{Be}(\alpha, \gamma)^{11}\text{C}$

The  $^7\text{Be}(\alpha, \gamma)^{11}\text{C}$  reaction rate remains very uncertain because of the quite limited knowledge on its cross section. Until recently, only the strength of the two resonances at  $E_{c.m.} = 884$  and  $1376$  keV were known [225]. This triggered new experimental efforts and recently the strength of two other resonances at  $E_{c.m.} = 1110$  and  $1155$  keV were measured in inverse kinematics using the DRAGON RMS [226, 227]. Thus, the NACRE II compilation [228] to evaluate the cross section uses a potential model analysis, and the strengths of higher energy resonances are estimated on the basis of the corresponding states in the mirror nucleus  $^{11}\text{B}$ . Likewise, DC contribution is calculated from the mirror reaction  $^7\text{Li}(\alpha, \gamma)^{11}\text{B}$ . As a consequence, the  $^7\text{Be}(\alpha, \gamma)^{11}\text{C}$   $S$ -factor is loosely constrained, and the rate below  $T = 0.2$  GK has an estimated uncertainty of about an order of magnitude. Further, the known

<sup>2</sup> UKRI ERC-StG grant EP/X019381/1.

resonance strengths rest on just a single experimental investigation. Measurement at higher energies would be interesting also to better determine the  $^{10}\text{B}(\text{p}, \gamma)^{11}\text{C}$  and  $^{10}\text{B}(\text{p}, \alpha)^7\text{Be}$  cross sections, since they populate the same compound nucleus [229]. At these higher energies, it would be very useful to measure the resonance that corresponds to the threshold state in the  $^{10}\text{B}+\text{p}$  reaction as well as broader higher energy resonances where their level assignments are still somewhat uncertain.

#### 4.2.4 Helium burning

##### $^{12}\text{C}(\alpha, \gamma)^{16}\text{O}$ , $^{16}\text{O}(\alpha, \gamma)^{20}\text{Ne}$

The  $^{12}\text{C}(\alpha, \gamma)^{16}\text{O}$  is challenging, being the cross section in the Gamow window ( $\approx 300\text{keV}$ ) the result of the composition of overlapping resonances and non-resonant components. The estimated cross section at  $E_{\text{c.m.}} = 300\text{keV}$  is about  $2 \times 10^{-17}\text{b}$  [135] which makes a direct measure unfeasible. The estimation is done by extrapolating higher-energy measurements to the stellar energies through a phenomenological model such as R-matrix. The  $^{12}\text{C}(\alpha, \gamma)^{16}\text{O}$  reaction has been studied for more than 60 years now, see, e.g., [135]. Its astrophysical interest was known since 1957 [230], but experiments specifically for this purpose started only 13 years later with [231]. Given its central role in the astrophysical scenario, many research groups faced the goal of measuring the  $^{12}\text{C}(\alpha, \gamma)^{16}\text{O}$  cross section from that moment on. The demand for more accurate cross section extrapolations, pushed the design of increasingly sophisticated apparatuses and analysis techniques to solve the experimental and theoretical difficulties arising. Despite all of the work mentioned above, the uncertainty on the extrapolated  $S$ -factor sits around 15%. Fits are now mostly limited by inconsistencies of data sets available in the literature especially for the  $E2$  ground state transition. In synthesis, the following focus on future measurements is desired [135]:

- Differential cross section,
- Interference behavior,
- Accurate cascade transitions,
- Lower energy measurements with RMSs.

However, beam-induced background, mainly from  $(\text{n}, \gamma)$  reactions induced by neutrons from the  $^{13}\text{C}(\alpha, \text{n})^{16}\text{O}$  reaction, will still remain one of the major challenges to be afforded. Past measurements have shown that this background can be strongly suppressed using time of flight (e.g., [232–234]), and that this outweighs the loss of beam intensity because of the gain in signal to background. The  $E1$  and  $E2$  multipole components of the ground state transition are the dominant components of the total cross section at low energy. The  $E1$  is most pronounced at  $90^\circ$  [235], while the  $E2$  and the interference term distribute the  $\gamma$  intensity more evenly over a larger angular interval. Therefore, a high-efficiency detection setup able to cover forward,  $90^\circ$ , and backward angles will be required.

It is very important to anchor any low-energy measurements with a scan of the well-known broad  $1^-$  level at a center of mass energy of about  $2.3\text{MeV}$ . Measurements with improved accuracy are needed to better constrain the shape of the tails of the  $1^-$  resonance, thereby improving the extrapolation to low energy because the resonance shape is distorted due to interference with the sub-threshold state. These measurements are desirable both above and below the  $1^-$  resonance, as demonstrated by the greatly improved constraint provided by the results reported in [236].  $E2$  measurements over this region are also highly desirable where there is a great deal of discrepancy in past data [135, 237]. Finally, very low-energy  $E2$  measurements, which will be extremely challenging, can constrain the relative contributions of the  $E2$  sub-threshold state and the  $E2$  DC component [238].

Another possible approach to measure the  $^{12}\text{C}(\alpha, \gamma)^{16}\text{O}$  is to use a RMS where the  $^{16}\text{O}$  produced in the reaction is detected in coincidence with  $\gamma$ -rays, thus measuring at the same time the total cross section and the angular distribution of the  $\gamma$ -rays. The environmental background is negligible on the charged particle detection and is strongly suppressed in the  $\gamma$ -ray spectra by applying coincidence between recoils and photons. This has been done in the past with the ERNA separator [167]. The total cross section data are still, after almost 20 years, the most stringent constrain to the R-matrix fit in the energy range covered with RMS measurements. The ERNA collaboration has upgraded the apparatus with a new beam optics layout and a recirculating helium jet gas target combined with a  $2\pi$  scintillator array to extend its capability both in terms of energy range and angular resolution of the  $\gamma$ -ray detection. The ongoing campaign will assess the cross section down to  $E_{\text{c.m.}} \sim 1\text{MeV}$  with a focus on the  $E1$  and  $E2$  contributions.

The  $^{16}\text{O}(\alpha, \gamma)^{20}\text{Ne}$  reaction represents the endpoint of the main reaction sequence  $^4\text{He}(2\alpha, \gamma)^{12}\text{C}(\alpha, \gamma)^{16}\text{O}(\alpha, \gamma)^{20}\text{Ne}$  and determines, together with the rate of  $^{12}\text{C}(\alpha, \gamma)^{16}\text{O}$ , the  $^{16}\text{O}$  abundance at the ignition of the carbon burning phase in late stellar evolution. As for  $^{12}\text{C}(\alpha, \gamma)^{16}\text{O}$ , the ERNA RMS at CIRCE can be used for the measurement of the  $^{16}\text{O}(\alpha, \gamma)^{20}\text{Ne}$  total cross section using the already available gas target and the same final detector with a few upgrades in the setup.

##### $^{14}\text{N}(\alpha, \gamma)^{18}\text{F}$ , $^{15}\text{N}(\alpha, \gamma)^{19}\text{F}$

Thanks to their high  $Q$  value, both the reactions are good candidates for measurements at the BIBF 3.5 MV accelerator through  $\gamma$ -ray spectroscopy.

At temperatures from 0.1 to 0.5GK, the rate of the  $^{14}\text{N}(\alpha, \gamma)^{18}\text{F}$  reaction rate is dominated by the contribution of a  $J_\pi = 1^-$  resonance at  $E_{\text{c.m.}} = 572\text{keV}$ . Below 0.1GK additional contributions are possible from the low-energy tail of the 445keV resonance, the DC component, and the  $J_\pi = 4^+$  resonance at 237keV. The lowest directly measured resonance is the one at 445keV [239], whose cross section is sufficiently high to allow a new measurement. The strength of the  $E_{\text{c.m.}} = 237\text{keV}$  resonance has never been measured

and is far below present experimental measurement possibilities. The DC contribution for this reaction is only theoretically estimated from spectroscopic factors, using some crude approximations, to be about 0.7–0.8keV b [240]. An underground measurement is an opportunity to determine it.

The rate of the  $^{15}\text{N}(\alpha, \gamma)^{19}\text{F}$  reaction is dominated by the resonant contribution of several low-lying states in  $^{19}\text{F}$ . At astrophysical relevant energies, the main contributions to the thermonuclear reaction rate are from the  $E_{\text{c.m.}} = 364, 536$  and  $542$  keV resonances. The strength of the 364keV resonance, directly influencing the reaction rate at temperatures lower than 200MK, has been measured only indirectly [241]. The counting rate at this energy is about 100 reactions per day considering an  $\alpha$  beam of  $100 \mu\text{A}$ , allowing for a direct measurement in the underground facility. Also in this case, the high beam intensity might allow to perform a measurement of the DC component.

However, such measurements require a new and high-efficiency  $4\pi$  segmented detector and a HPGe detector in close geometry, while monitoring target degradation for a proper cross section normalization. An optimization of the setup (e.g., low absorption aluminum vacuum pipes, lead and polyethylene shielding around the detectors) will also concur to maximize the signal to noise ratio to achieve the best possible precision.

The  $^{15}\text{N}(\alpha, \gamma)^{19}\text{F}$  reaction has been recently studied also using the ERNA RMS [172]. Similarly, the  $^{14}\text{N}(\alpha, \gamma)^{18}\text{F}$  might be investigated. The measurement of the total cross section through the detection of the recoils produced in the reactions can provide complementary information about the processes and experimental systematic effects.

#### $^{17}\text{O}(\alpha, \gamma)^{21}\text{Ne}, ^{18}\text{O}(\alpha, \gamma)^{22}\text{Ne}$

Both the  $^{17}\text{O}(\alpha, \gamma)^{21}\text{Ne}$  and  $^{18}\text{O}(\alpha, \gamma)^{22}\text{Ne}$  reactions have been scarcely studied in the past and no DC data exist for these reactions. The strengths of some of the resonances are known, although with large uncertainties [240, 242]. Both nitrogen and oxygen targets are very well known and were studied many times during the last years. Additionally, the experimental technique could involve the activation method [243] for the first reaction and the total absorption spectroscopy [159] for the second one. Furthermore, both the techniques would require the use of a highly segmented and efficient scintillator clover detector [23]; thus, both the reactions could be studied during the same beam time.

#### 4.2.5 Neutron sources

##### $^{22}\text{Ne}(\alpha, n)^{25}\text{Mg}, ^{22}\text{Ne}(\alpha, \gamma)^{26}\text{Mg}$

The energy range of interest for both reactions is around 460–750 keV (for a stellar temperature of 300 MK), and below the neutron production threshold at  $E_{\alpha} = 561.9$  keV only the  $\gamma$ -ray channel is active. Both below and above the threshold, a number of natural-parity compound states have been identified, but their resonance strengths are not known (mostly due to undetermined  $\alpha$  widths) [244]. Only a single resonance in the stellar energy window (at  $E_{\alpha} = 830$  keV) has been directly measured in both channels, leading to large uncertainties in nucleosynthesis calculations.

Using dedicated detector and target systems (see Sect. 2.1.2), the high beam intensity of the BIBF 3.5 MV accelerator and the ultra-low background in the underground, an increase in sensitivity for both reactions by at least three orders of magnitude is expected.

The measurement of the neutron channel is funded by the SHADES ERC starting grant.<sup>3</sup> Instead of traditionally used energy-blind moderating neutron counters it relies on a coupled array of liquid scintillators and  $^3\text{He}$  counters, allowing for a certain energy sensitivity. This latter point is of great importance to be able to identify possible beam-induced backgrounds, which have been an issue in past experiments [245]. In addition, it allows to suppress a part of the remaining higher-energy natural neutron background, improving sensitivity even more.

The measurement of the  $(\alpha, \gamma)$  channel has strong synergies with the neutron setup, utilizing the same target and electronics system. Design of a high-efficiency, low-background  $\gamma$ -ray detection system is underway.

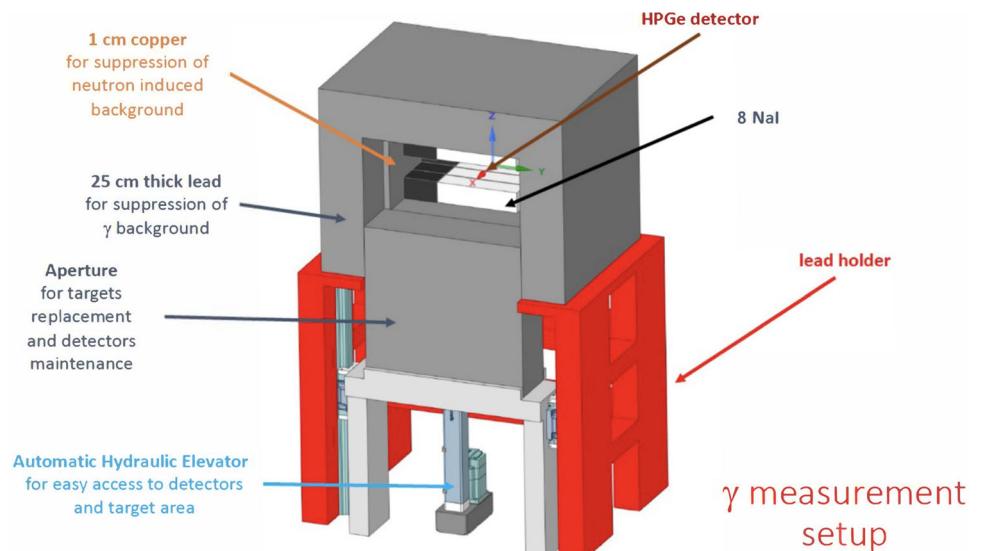
The program for both measurements is similar: re-measuring the 830 keV resonance and performing a high-sensitivity search for resonances in the astrophysical energy range.

##### $^{13}\text{C}(\alpha, n)^{16}\text{O}$

As discussed in Sect. 4.1, this reaction is the main neutron source in AGB stars, at Gamow energies of 140–230keV. Due to the nuclear structure of the  $^{17}\text{O}$  compound nucleus, the reaction rate in this region of interest is dominated by two resonances: the near-threshold resonance at  $E_x = -3 \pm 8$  keV and a wide resonance at  $E_{\text{c.m.}} = 880$  keV ( $E_x = 7215$  keV,  $\Gamma = 300$  keV). As for direct measurements, two recent measurements were performed in underground laboratories by the LUNA [162] and JUNA collaborations [246], entering the Gamow window and improving the extrapolation toward lower energies. In particular, at LUNA was used an  $\alpha$  beam impinging on a solid highly enriched  $^{13}\text{C}$  target, produced by evaporation. Neutrons were detected using the  $^3\text{He}$  counters detection array [25]. The cross section was determined in the  $E_{\text{c.m.}} = 230$ –305 keV energy range, with an overall uncertainty lower than 20% for all data points, thanks to the setup high efficiency and the low intrinsic background in combination with an innovative method for target monitoring [247]. It has been shown, in particular, that this reaction rate is about 20% lower than previously estimated, with interesting consequences for the production of some s-process isotopes. This result was confirmed by the independent measurement performed at the JUNA underground laboratory [246]. However, at high energy, the new measurements

<sup>3</sup> SHADES ERC-SiG grant n. 852016.

**Fig. 15** Drawing of the shielding for the  $^{12}\text{C} + ^{12}\text{C}$  measurement which will be installed at LNGS



present a systematic difference with respect to the results of previous experiments. For this reason, a further study at higher energy would clarify the origin of this discrepancy, thus allowing a better R-matrix fit of the astrophysical  $S$ -factor down to the energies relevant for  $s$ -process nucleosynthesis. Independently, a crucial open point is a 30% discrepancy between different data sets on the 880keV resonance, i.e., the results reported in [248] and in [249]. According to the sensitivity study presented in [250], the inconsistency in the overall normalization of the  $^{13}\text{C}(\alpha, n)^{16}\text{O}$  experimental data remains a significant source of uncertainty.

Thanks to the BIBF 3.5 MV accelerator, the LUNA measurement will be extended toward higher energies, providing a complete data set over a wide energy range.

#### 4.2.6 Carbon burning

##### $^{12}\text{C} + ^{12}\text{C}$ , $^{12}\text{C} + ^{16}\text{O}$

Fusion reactions involving carbon nuclei are among the most important in stellar evolution since they determine the fate of massive stars. In particular,  $^{12}\text{C} + ^{12}\text{C}$  and  $^{12}\text{C} + ^{16}\text{O}$  reactions play a crucial role in the C and O burning phase of stellar evolution. Existing data do not provide an estimate of the stellar rate of these reactions with the precision required by stellar models. Recent indirect measurements indicated possible low-energy resonances, dramatically changing the predicted rate, calling for improved direct investigations. In the past, some experiments provided hints of an anisotropic angular distribution of the  $^{12}\text{C} + ^{12}\text{C}$  reactions [251].

The  $^{12}\text{C} + ^{12}\text{C}$  will be the flagship reaction of the first 5-year scientific program of the LUNA Collaboration with the BIBF 3.5 MV accelerator. Energies in the center of mass system down to about 1.5 MeV will be investigated. The reaction can proceed through different channels corresponding to the emission of a photon, a neutron, a proton, an  $\alpha$  particle or even two  $\alpha$  particles or a  $^8\text{Be}$  nucleus. Of these channels, the two more relevant are the emission of protons and alpha particles. The proton and alpha channels can be measured either by detecting the charged particles or by revealing the  $\gamma$  decay of the first excited state to the ground state of the  $^{23}\text{Na}$  or  $^{20}\text{Ne}$  residual nuclei, respectively. A significant challenge in direct measurements is the beam-induced background, produced by the interaction of the impinging C ions with  $^1\text{H}$  and  $^2\text{H}$  contaminations present in graphite targets. Different approaches have been attempted to mitigate this issue [175, 252], also at LNL the dedicated experiment HEAT (Hydrogen dEsorption from cArbon Targets) was started [10] to develop a reproducible technique for hydrogen desorption in different types of graphite targets through heating up to 1200 °C, while assessing hydrogen content through different IBA techniques.

To measure the reaction cross section through the detection of  $\gamma$ -rays, the LUNA Collaboration is developing a setup composed by a lead (25cm thick) and copper (1cm thick) shielding to suppress the environmental  $\gamma$ -ray background. The detection setup will feature a HPGe detector (150% relative efficiency) installed at  $0^\circ$  in close geometry to the target to maximize the signal to noise ratio and 8 NaI scintillator detectors surrounding both the target and the HPGe for Compton suppression; see Fig. 15.

To measure the reaction cross section detecting charged particles, their identification is needed, and different options are already under evaluation.

A promising candidate is the GASTLY (Gas-Silicon Two-Layer sYstem) detector [35] consisting of an ionization chamber (IC) and a silicon strip detector (SSD) already used to measure this reaction at higher energies [36]. The intrinsic background of the GASTLY detectors expected from  $\alpha$  emitter contaminations in the detector's materials, was studied within a joint effort of the ERNA and LUNA collaborations. Background measurements performed underground in different conditions, e.g., several gas pressures, show background levels compatible with the expected yield for the  $^{12}\text{C} + ^{12}\text{C}$  reaction at 1.5 MeV of a few reactions

per day. Additional material characterization studies and Monte Carlo simulations are undergoing in order to identify most critical components and thus further reduce the intrinsic background with appropriate choice of materials or coatings. Another option is given by nTD detectors using pulse shape discrimination analysis techniques, as already described in Sect. 4.2.5.

Using the intense beam of the CIRCE laboratory accelerator, the ERNA Collaboration performed measurements of the  $^{12}\text{C} + ^{12}\text{C}$  down to  $E_{\text{c.m.}} \approx 2.0$  MeV [36] and plans to measure  $^{12}\text{C} + ^{16}\text{O}$  down to  $E_{\text{c.m.}} = 3.0$  MeV, respectively. Such low energies have already a strong influence at the astrophysical region. Regions of energies where discrepancies still remain will be covered and data will overlap with the results obtained by indirect methods [151]. These data will clarify discrepancies, conceal results obtained with direct and indirect methods and minimize uncertainties.

#### 4.2.7 ERNA RMS innovative applications

**Half-life measurements** Under terrestrial conditions, the short range of the strong interaction and its strength make the environmental influence on the atomic nucleus wave function negligible. Consequently, in most cases nuclear decay is not affected by environmental conditions. However, there are exceptions, like electron capture decay (EC). This process depends on the electron density in the nucleus, which can be modified by environmental conditions.  $^7\text{Be}$  is a nucleus decaying purely by EC to  $^7\text{Li}$  ( $Q = 0.861$  MeV): the decay populates either the  $^7\text{Li}$  ground state (90%) or the first excited state at 478 keV (10%) decaying to the  $^7\text{Li}$  ground state. The simple nuclear and atomic configurations of  $^7\text{Be}$  allow influencing the electron density at the nucleus rather easily, thus making  $^7\text{Be}$  ideal to constrain the decay nuclear matrix elements (NMEs). Moreover, the comparison of the so obtained experimental NMEs with calculated ones can provide a valuable contribution to the solution of the quenched  $g_A$  puzzle. This latter refers to the need for quenching the axial coupling constant  $g_A$  in nuclear many-body calculations employing truncated Hilbert spaces to reproduce beta-decay data [253]. In addition, it is worth noting that the change of the  $^7\text{Be}$  decay rate has been demonstrated to have a significant impact in solar physics and neutrino physics [254, 255].

A possible, yet unexplored, way to measure the change in half-life for different  $^7\text{Be}$  ionization, is to observe its in-flight decay. This possibility is based on the fact that  $^7\text{Be}$  EC decay produces  $^7\text{Li}$  ions in the same charge state, being Auger emission from ionized Li not allowed. Therefore, the measurement of the number ratio  $^7\text{Be}$ -to- $^7\text{Li}$  ions allows determining the half-life, provided:

- The  $^7\text{Be}$  ion beam is sufficiently purified from  $^7\text{Li}$ .
- Both  $^7\text{Be}$  and  $^7\text{Li}$  ions from the in-flight decay are fully collected.

A full feasibility study has been performed at CIRCE by the ERNA Collaboration [256, 257]. Based on this work, the measurement is briefly described below.

Ions are accelerated toward the terminal, which is equipped with a gas stripper system, where molecules break and  $^7\text{Be}$  ions in different charge states  $q_i$  are formed emerging from the accelerator with different energies. The  $^7\text{Li}$  contamination is eliminated populating the  $4+$  charge state, not accessible to Li, in a post-stripper at the accelerator exit. The pure  $^7\text{Be}^{4+}$  beam is transported to the ERNA gas target through the AMS system, a dipole magnet–electrostatic analyzer–dipole magnet combination, that cleans up contamination with mass different from  $A = 7$ . The gas target system can be operated with heavy or light gases to optimize the population of high or low charge states, respectively. Finally, the pure  $^7\text{Be}$  beam in the selected charge state enters the ERNA RMS and is transported to the end detector, a  $\Delta E$ – $E$  telescope able of charged particle identification.

The in-flight half-life measurement described here is part of the project ASBeST (A 7-Beryllium electron capture STudy for nuclear and solid state physics), supported by the Italian Ministry of Research through the funding action PRIN2020.

**THM with RMS** The measurement of the cross section of an  $A + x \rightarrow c + C$  two-body reaction of astrophysical interest using the THM (see [194, e.g.]) requires the selection of the quasi-free contribution of the three-body reaction  $a + A \rightarrow c + C + s$  measured in laboratory. For measurements where the TH nucleus  $a$  is used as projectile the quasi-free reaction mechanism gives the maximum contribution to the three-body process for the spectator nucleus  $s$  emitted at zero degree. Although in a typical TH measurement nuclei  $c$  and  $C$  (ejectiles of the two-body process of interest) are detected in coincidence, in some cases spectator detection becomes necessary. In detail, it becomes crucial when one among  $c$  or  $C$  is a neutron as for the  $^{13}\text{C}(\alpha, n)^{16}\text{O}$  or  $^{22}\text{Ne}(\alpha, n)^{25}\text{Mg}$  reactions. In such cases the use of a RMS, allowing the measurement of the spectator at zero degree, improves the coverage of the kinematical region where the quasi-free mechanism is favored, reducing the contribution due to other unwanted reaction mechanisms. This would allow for a different and complementary way to apply the THM. The excitation function of the two-body reaction of astrophysical interest will be measured in the best quasi-free kinematic conditions, that is momentum of the spectator equal to zero, with a change of the beam energy in order to span the energy range of astrophysical interest. Moreover, the possibility to measure at zero degree can improve the THM studies when one of the two ejectiles is emitted at very forward angles, allowing for a better covering of the quasi-free phase-space region. An actual physical case is represented by the  $^{23}\text{Na}(d, \alpha)^{20}\text{Ne}$  THM reaction measured to study the  $^{23}\text{Na}(p, \alpha)^{20}\text{Ne}$  (preliminary results obtained with standard THM are reported in [258]). The ERNA RMS could allow to perform such kind of zero-degree measurements even if the available beam energies represent an important limit for the application of the THM where beam energies of tens of MeV might be required (even up to 100 MeV). Nevertheless, in order to investigate the coupling of the THM measurement with RMS and the possible experimental advantages, we propose a test consisting in the study of the  $^{13}\text{C}(\alpha, n)^{16}\text{O}$  applying the THM to the  $^{13}\text{C}(^6\text{Li}, n)^{16}\text{O}$  reaction where the  $^6\text{Li} = (\alpha \oplus d)$  is the TH nucleus. Such reaction



was already measured with  ${}^6\text{Li}$  as target nucleus [259, 260]. Now the idea is to use a  ${}^6\text{Li}$  beam delivered on a  ${}^{13}\text{C}$  target. Taking advantage of ERNA RMS the deuteron (spectator) will be detected at zero degree in coincidence with the  ${}^{16}\text{O}$  (measured using a position sensitive detector at target position) with a better selection of the quasi-free kinematical region and a reduced background. To perform such measurement, a scattering chamber to place a solid target and an array of DSSSD is required.

*Triple- $\alpha$  with RMS* As stated before, the triple- $\alpha$  process is crucial to bridge the  $A = 5$  and 8 mass gaps in the first generation of stars. Its rate is determined by the decay widths of the Hoyle state in  ${}^{12}\text{C}$ . The latter is the main channel in the intermediate-temperature domain. A large part of the uncertainty in the reaction rate estimation is currently related to the knowledge of the radiative decay width of the Hoyle state, e.g., the recent estimation in [107] is in disagreement with the former state of the art [261]. Unfortunately, the detailed measurement of the radiative decay of the Hoyle state is not trivial, as it requires precision  $\gamma$ -ray measurements. An alternative way is to probe the radiative decay branching ratio by exploiting particle-particle coincidence techniques, as previously done, for example, in Ref. [262]. To this end, the Hoyle state in  ${}^{12}\text{C}$  can be formed as the final state of a nuclear reaction, such as  ${}^{13}\text{C}({}^3\text{He}, {}^4\text{He}){}^{12}\text{C}$ , and the radiative decay branching ratio of the Hoyle state can be measured from the coincidence rate between the two ions in the final state, given that the reaction ejectile tags the residual  ${}^{12}\text{C}$  in its Hoyle state. Usually, a pair of detectors can be used to detect the two ions in kinematical coincidence. However, the most favorable kinematical conditions are obtained when the light fragment is emitted backward, such that the recoiling  ${}^{12}\text{C}$  has the maximum energy. This poses challenges due to the high-rate measured at forward angle. An RMS such as ERNA could be successfully exploited to overcome these limitations and crucially enhance the rate in the most favorable kinematical conditions.

## 5 Applied nuclear physics

The development of nuclear astrophysics experiments at CIRCE has led to a fruitful interchange between basic and applied research activities. Indeed, analytical tools routinely used in applied nuclear physics can be devoted to fundamental research, and the techniques and instrumentation developed for nuclear physics experiments contribute to an important know-how for further uses in applications.

In Sect. 5.1 will be described the use of conventional and accelerator-based mass spectrometry to study processes of astrophysical interest by means of isotopic ratio measurements. Similarly, some technical developments needed for nuclear physics experiments (ion beams, detectors and related equipment) have led to applications in various fields, as described in Sect. 5.2. At present, similar applications are performed in few specific research centers, however often involve only one analytical technique (mostly AMS). In this framework CIRCE, with the potential of multi-analytical isotopic techniques, represents an opportunity for nuclear physics research but also for the development and characterization of complex detectors.

### 5.1 Mass spectrometry

Isotope ratio mass spectrometry (i.e., the measurement of a sample isotope ratio based on high resolution magnetic selection and ion counting) is a specialized analytical technique usually utilized to address different scientific issues over several research fields such as Geology, Environmental Sciences, Archaeology, Food and Material Sciences [263]. Here is given a short overview of the current state of the art of the isotope ratio mass spectrometric techniques applied to different field of research related to CSN3 activities at CIRCE, also highlighting possible developments over short- to midterm time ranges.

For the simplicity of illustration, isotope ratio mass spectrometry techniques applications, either if historically originating from the same root [264], are introduced and discussed according to the specific isotope ratio, rare vs stable, to be measured.

#### 5.1.1 Accelerator mass spectrometry for the measurement of rare isotope ratios

The development of accelerator mass spectrometry (AMS) allows the determination of the relative isotopic abundance of rare isotopes (long lived radioisotopes) with respect to stable ones. Such isotopic ratios span from over  $10^{-12}$  (or higher) to  $10^{-16}$  [265]. AMS history is mostly related to the use and development of accelerators for nuclear physics experiments [266], and its definitive birth is related to experimental activities related to the measurements of  ${}^{14}\text{C}$  (radiocarbon) isotope ratios for dating applications by cyclotron [267] or tandem accelerators equipped with Cs negative ion sputter source [268]. That is why, along its lifespan, AMS has always been tightly connected to nuclear physics research studies, sharing with them most of the technology utilized. AMS spectrometers allow the measurement of rare vs abundant isotope ratios being also characterized by a wide dynamic range, and guaranteeing the best precision performances, i.e., from 0.3% to c.a. 10% relative error depending of the measured isotope at typical detection abundances through the use of fast cycling technologies such as magnet bouncing systems [269].

AMS applications at CIRCE Laboratory described in this paper fall in

- i) i) The ultra-sensitive determination of  ${}^{14}\text{C}$  isotope ratios for archaeometry, forensics and environmental sciences;
- ii)  ${}^{14}\text{C}$  AMS measurements on tree rings to search for past astrophysical events in proximity of the Solar System;
- iii) The ultra-sensitive determination of actinides, U and Pu, for environmental studies like radionuclides release monitoring during nuclear power plant operation and decommissioning;

- iv) The determination of  $^{244}\text{Pu}$  content in environmental matrices (carbonatic sediments), to search for natural occurrence of this isotope;
- v) Ultra-sensitive determination of material composition for rare events physics studies and
- vi) The direct determination of nuclear reaction strengths such as  $^{25}\text{Mg}(\text{p}, \gamma)^{26}\text{Al}$ .

Measurements for points (i) and (iii) are reported here to highlight typical AMS application performed at CIRCE laboratory, but also to stress the point that methods and knowledge developed starting from nuclear physics technologies, after a period of development and specialization, may come back to their origins in order to be used for specific of analytical requests for nuclear physics studies. As examples of such applications of  $^{14}\text{C}$  AMS, we like to mention the dating of the “Acerenza portrait” in archaeometry, the determination of the year of death and age at death for forensics [270] and the determination of colonization chronology for the Caribbean for environmental sciences and paleoanthropology [271]. Also the development of new procedures allowing to increase the bouquet of datable materials such as Mortars [272, 273] should be mentioned here. For example, attained sample preparation methodologies performances (i.e., lower detection limits) can play a key role for the ultra-sensitive determination of material composition for rare events physics studies (vi). The developments needed in such researches, leading on the average to practical feed-backs such as pushing toward the limits the minimum analyzable mass while guaranteeing high precision (i.e., specific compound radiocarbon analysis), might increase the possibilities of analyses for fundamental nuclear physics measurements applications drastically reducing the necessity of long time demanding chemical preparation. For Actinides it is the case to mention the characterization of environmental matrices collected around the Garigliano Nuclear Power Plant, for the purpose of environmental monitoring during plant decommissioning, through the measurement of  $^{236}\text{U}/^{238}\text{U}$ , and  $^{239}\text{Pu}/^{240}\text{Pu}$  ratios [274, 275].

A bit higher degree of detail will be spent in discussing applications of  $^{14}\text{C}$  AMS developed within the ERNA experiment to identify in geological and environmental archives traces of past near Earth astrophysical events (point iii). Over the last decade a strong research effort was spent by several AMS laboratories aiming to look at fast  $^{14}\text{C}$  concentration increase by working onto annually resolved tree rings series. The combination of the ultra-precise measurements with a chronological proxy allows to infer about solar activity, namely Solar Proton Event (SPE), and several events have been identified and confirmed also by C biogeochemical modeling [276, 277]. However, also SNe events and Gamma Ray Bursts (GRB) might have a role in producing such spikes. This aspect was sometimes discussed, but its role was neglected also because no known SNe were reported for the period of interest. On the contrary, at CIRCE annual resolved tree ring series in the 1030–1080 AD interval from a Finnish Lapland Tree [278] was analyzed aiming to evaluate possible SNe influence on the period of the SN1054 [279], i.e., the event that generated the Crab Nebula, that is sufficiently close to Earth to contemplate this possibility. While a clear oscillation during 1050–1063 CE was found, having different characteristics with respect to other identified SPEs, its connection to the SN1054 remains unclear, and other measurements using  $^{14}\text{C}$  and/or different proxies, e.g.,  $^{10}\text{B}$  in polar ices, are required.

The search for astronomical events in the local Universe also involves the AMS of actinide nuclei. In particular, the determination of  $^{244}\text{Pu}$  abundances can be performed on environmental matrices (carbonatic sediments) to search for natural production of this isotope. Several studies attribute the production of this nuclide to explosive stellar nucleosynthesis environments, such as some types of SNe and neutron star mergers [280]. Reported typical concentrations of  $^{244}\text{Pu}$  for environmental samples are in the range of tens to hundreds of attograms per gram of sediment ( $10^{-18}$ ) with an isotopic ratio of  $^{244}\text{Pu}/^{239}\text{Pu}$  c.a.  $10^{-4}$ ; therefore, AMS is the tool of election for such measurements. At CIRCE Laboratory, AMS performances have been assessed by measuring 2 reference samples, IAEA 410 and 412, for the validation of the analytical procedures (sample preparation and measurement) to be applied to sedimentary rock samples, with the final goal to infer about *r*-process captures that might lead to natural occurrence of  $^{244}\text{Pu}$ .

AMS applications in Nuclear Astrophysics fall also into the direct cross section measurements through the detection of isotope ratios. An example of this kind of measurements is the determination of the resonance strengths in the  $^{25}\text{Mg}(\text{p}, \gamma)^{26}\text{Al}$  fusion process that plays a key role in the MgAl cycle. The study of this reaction through  $\gamma$ -ray spectroscopy was complemented by a measurement of the  $^{27}\text{Al}/^{26}\text{Al}$  ratio in  $^{25}\text{Mg}$  samples, doped with a known amount of  $^{27}\text{Al}$ , that were irradiated at the LUNA 400 kV accelerator at LNGS at the energy corresponding to the resonance at  $E_{\text{c.m.}} = 304$  keV [281].

### 5.1.2 SIRMS and MC-ICP-MS or the measurement of stable isotope ratios

The sensitivity prerequisite for the determination of stable isotope ratios in a sample asks for an Isotope Ratio Mass Spectrometer capable to measure isotope ratios ranging from  $10^{-2}$  till  $10^{-4}$  [282]. To reach such a ratio sensitivity, it is possible to operate at lower energies and thus apparatuses of minor complexity are used. The precision that can be achieved ranges typically around 0.01% to 0.001% (relative error) depending on the measured isotopes and on the spectrometer specifications. For such purposes, two different approaches can be applied: (1) using an adequate ion source (electron impact or thermal ionization) producing a quasi-monoenergetic beam (i.e.,  $\Delta E$  10 eV) only a magnetic selection can be applied (SIRMS or TIMS); ii) ion sources producing higher energy spread (ion coupled plasma) requires double focusing using an electrostatic analyzer (ESA) to reduce energy spread produced during ionization (SF-ICP-MS). Nowadays double-focusing mass spectrometers with forward or reverse Nier-Johnson [283] for isotope ratio measurements. Precision can be drastically improved using an array of position adjustable collectors (Faraday cups plus single electron multipliers) guaranteeing the desired dynamic range. These methodologies are routinely conducted for environment and cultural heritage studies and applications.

Among the applications of stable isotope ratio mass spectrometry of interest for the INFN-CSN3 activities performed at CIRCE, it is worth to mention the development and application of MC-ICP-MS to search for nucleosynthesis signatures in meteoritic materials. This project was initiated as an extension of a project of the University of Perugia [284] where the study of such materials was started on samples of the local collection. These kind of researches are highly interdisciplinary, since the meteorites are quite complex objects, having specific phases characterized by different geochemistry that need to be carefully assessed, e.g., the metallic matrix and the olivine in metallic meteorites such as Pallasites [285, 286], to understand the contribution due to the various processes that play a role to their isotopic enrichment. At CIRCE have been developed and characterized the procedures aimed at the measurement of the Ni isotopes ratio, since  $^{60}\text{Ni}$  is the stable product of the decay of  $^{60}\text{Fe}$ , that is one of the main nucleosynthesis products of core-collapse SNe. The sample preparation and measurement procedures have been tested and validated onto the reference material NIST SRM 986 doped with Fe. Actual measurements can be performed provided the availability of the meteorite samples.

## 5.2 Diagnostics and modification of materials with ion beams

Several technical developments made at CIRCE to meet the requirements of the experiments described above turned out to have interesting applications in material and devices characterization. These applications are briefly presented in the following sections.

### 5.2.1 Wear measurements

Radioactive ion implantation allows non-contacting, online wear measurements with sub micrometric sensitivity to be performed, by monitoring the removed and/or residual activity on parts subject to wear. Comparative studies of different materials, including those who exhibit a low resistance to radiation damage, can be easily performed by means of this technique.  $^7\text{Be}$  is a nuclide particularly interesting in this kind of applications because its intermediate half-life, 53 d, is long enough to perform experiments, but not too long to make its handling complicated, its decay mode (EC followed by a single low-energy  $\gamma$ -ray) reduces its radio-toxicity, its low atomic number allows larger implantation depths while minimizing the damage to the tested materials. The development of a  $^7\text{Be}$  ion beam at CIRCE [30] made these applications possible in fundamental and in applied industrial research. A dedicated implantation beam line is present at CIRCE; see Fig. 3. It allows for the realization of tailored radionuclide depth distributions on a variety of samples (e.g., bushings, joints, bearings) through a combination of different beam energies and passive absorbers.

In collaboration with the CIRA (Italian Aerospace Research Centre) the study of durability tests of Thermal Protection Systems (TPS) used in space science to protect space vessel in atmospheric reentry are performed. The  $^7\text{Be}$  ion implantation has been proposed as an innovative tool to study the deterioration of ablative TPS [287–289] and the IBA techniques are used for the composition estimation of the sample [290]. The collaboration in this field is still open, in the next years the  $^7\text{Be}$  ion implantation and the IBA methods will be applied to ceramic TPS to study, respectively, their recession rate and their surface oxidation.

In addition, among other equipment developed for fundamental nuclear physics research the ERNA collaboration has built and used different windowless gas targets, both extended and as supersonic jet. Supersonic jet gas targets are very similar, besides dimensions, to plasma wind tunnels used to study the durability of materials of interest for space missions. Due to its quite compact size a jet gas target with a high degree of ionization, i.e., a supersonic plasma jet, is an interesting opportunity for material testing because of the major reduction of the complexity and both the building and running costs. Such a system would be also very interesting for fundamental nuclear research, in particular for the study of electron screening effects in nuclear reactions [291]. The development of a supersonic plasma jet has been investigated in a joint effort with CIRA [292]. The use of such a system in nuclear physics is discussed in the LNF Session of the Nuclear Physics Mid Term Plan [12].

### 5.2.2 Materials characterization

Another activity that benefits of the intense and well characterized  $^7\text{Be}$  ion beam is the ASBeST project. This project aims at measuring the effect of electron density variation on  $^7\text{Be}$  EC decay rate and possibly its applications.

To reach this goal,  $^7\text{Be}$  implantations in silicon carbide (SiC) devices are conducted in order to study the possible variation in the half-life of the beryllium isotope under intense electrostatic field, of the order of  $\text{MV cm}^{-1}$ . For this study, is of paramount importance to understand how the implanted  $^7\text{Be}$  ions are located in the SiC lattice and the nature of this impurity. In fact, the  $^7\text{Be}$  can create a substitutional or interstitial impurity, that corresponds to a completely different behavior with respect to the electrostatic field. For this purpose, the channeling-RBS is a powerful tool [293]; therefore, a scattering chamber with a five-axis in-vacuum sample manipulator is under commissioning phase and will allow to perform both Channeling-RBS and Elastic Recoil Detection Analysis (ERDA) measurements.

Since 2018, adjacent to the CIRCE is present the CAPACITY (Campania AstroPartiCle InfrastrucTure facilitY) laboratory, whose main goal is to build the detection units and related equipment for the KM3NeT deep-sea neutrino telescope [294]. The close contact between the two laboratories has generated a positive feedback. A program aimed at the investigation of the performances of materials and devices to be deployed at high depths, was started exploiting the high sensitivity of IBA and Mass Spectrometry techniques. In fact, water penetration is expected to be one of the main factors limiting the lifetime of the KM3NeT underwater equipment. A first series of measurements showed that through these techniques it is possible to identify micro-leaks on a scale

capable to produce a critical malfunctioning in twenty years from deep-sea deployment. In detail, NRA and RBS can be used to trace penetration depth of deuterium in materials, such as glass or plastics, exposed to deuterated water ( $D_2O$ ) at high pressure. Deuterium can be also detected with SIRMS on microtome cut plastic samples of such exposed materials. Using SIRMS can be also quantified the amount of  $^{14}C$ , introduced as a spike in the inorganic carbon dissolved in water, that leaks into immersed air filled assembled parts (e.g., detection modules) or liquid-filled parts (e.g., oil-filled cables). In order to push the attainable mass sensitivity by such isotopic methodologies, an innovative high-pressure test chamber with isotopic markers is under construction and an ISO4 clean room was installed. This equipment will allow sample tests to be carried out throughout the entire construction phase of the undersea telescope.

**Acknowledgements** The authors express their gratitude to LNGS for having hosted the Nuclear Physics Mid Term Plan in Italy - LNGS Session, in particular the Scientific Secretary of the Research Division for their support. The authors in WG1 wish to acknowledge the support of Grant No. 62099 from the John Templeton Foundation (the opinions expressed in this publication are those of the authors and do not necessarily reflect the views of the John Templeton Foundation). The support from the Foundational Questions Institute and Fetzer Franklin Fund, a donor advised fund of Silicon Valley Community Foundation (Grants No. FQXi-RFP-CPW-2008 and No. FQXi-MGB-2011), and from the H2020 FET TEQ (Grant No. 766900) is also acknowledged. The VIP-2 project is supported by the Austrian Science Foundation (FWF) through the Grant No. P25529-N20, Projects No. P30635-N36, and No. W1252-N27 (doctoral college particles and interactions). K. P. acknowledges support from the Centro Ricerche Enrico Fermi–Museo Storico della Fisica e Centro Studi e Ricerche “Enrico Fermi” (Open Problems in Quantum Mechanics project). A. M. wishes to acknowledge support by the Shanghai Municipality, through the Grant No. KBH1512299, by Fudan University, through the Grant No. JJH1512105, the Natural Science Foundation of China, through the Grant No. 11875113, and by the Department of Physics at Fudan University, through the Grant No. IDH1512092/001. The support from the STELLA facility at LNGS is gratefully acknowledged. A. M. thanks Rita Bernabei and Pierluigi Belli for useful discussions on the subject. The authors in WG2 and WG3 express their gratitude to the Accelerator Services of LNGS and CIRCE. Support by MIUR through the “Dipartimenti di eccellenza” project “Physics of the Universe” program, the EU grants ERC-SiG *SHADES* no. 852016, UKRI ERC-StG *ELDAR* no. EP/X019381/, *ChETEC-INFRA*, no. 101008324, the DFG BE 4100-4/1, the Helmholtz Association ERC-RA-0016, the NKFIH K134197, PD129060, the COST Action ChETEC CA16117, is gratefully acknowledged.

**Funding** Open access funding provided by Università degli Studi di Napoli Federico II within the CRUI-CARE Agreement.

**Data Availability Statement** No data associated with this manuscript.

**Open Access** This article is licensed under a Creative Commons Attribution 4.0 International License, which permits use, sharing, adaptation, distribution and reproduction in any medium or format, as long as you give appropriate credit to the original author(s) and the source, provide a link to the Creative Commons licence, and indicate if changes were made. The images or other third party material in this article are included in the article’s Creative Commons licence, unless indicated otherwise in a credit line to the material. If material is not included in the article’s Creative Commons licence and your intended use is not permitted by statutory regulation or exceeds the permitted use, you will need to obtain permission directly from the copyright holder. To view a copy of this licence, visit <http://creativecommons.org/licenses/by/4.0/>.

## References

- <https://www.lngs.infn.it>
- M. Laubenstein, I. Lawson, Low background radiation detection techniques and mitigation of radioactive backgrounds. *Front. Phys.* **8**, 506 (2020). <https://doi.org/10.3389/fphy.2020.577734>
- M. Ambrosio et al., Vertical muon intensity measured with [MACRO] at the Gran Sasso laboratory. *Phys. Rev. D* **52**, 3793–3802 (1995). <https://doi.org/10.1103/PhysRevD.52.3793>
- A. Best et al., Low energy neutron background in deep underground laboratories. *Nucl. Instrum. Methods Phys. Res. A* **812**, 1–6 (2016). <https://doi.org/10.1016/j.nima.2015.12.034>
- <https://www.circe.unicampania.it>
- C. Brogginini et al., Experimental nuclear astrophysics in Italy. *Riv. Nuovo Cim.* **42**, 103 (2019). <https://doi.org/10.1393/ncr/i2019-10157-1>
- A. Badalà et al., Trends in particle and nuclei identification techniques in nuclear physics experiments. *La Rivista del Nuovo Cimento* **45**(3), 189–277 (2022). <https://doi.org/10.1007/s40766-021-00028-5>
- Nuclear Physics Midterm Plan in Italy. <https://web.infn.it/nucphys-plan-italy>
- G. Benzoni, D. Bettoni, F. Bossi, M. Colonna, A. Di Leva, E. Fioretto, A. Formicola, L. Fortunato, S. Gammino, F. Gramegna, C. Gustavino, M. Junker, M. La Cognata, I. Lombardo, R. Nania, S. Pisano, E. Previtali, S. Romano, P. Russotto, F. Soramel, J.J. Valiente-Dobón, Nuclear physics midterm plan in Italy: introduction to the series. *Eur. Phys. J. Plus* **138**(6), 526 (2023). <https://doi.org/10.1140/epjp/s13360-023-04108-9>
- M. Ballan et al., Nuclear physics midterm plan at Legnaro National Laboratories (LNL). *Eur. Phys. J. Plus* **138**(8), 709 (2023). <https://doi.org/10.1140/epjp/s13360-023-04249-x>
- C. Agodi et al., Nuclear physics midterm plan at LNS. *Eur. Phys. J. Plus* **138**, 1038 (2023)
- Nuclear Physics Midterm Plan at LNF (In preparation)
- Nuclear Physics Midterm Plan in Italy—LNGS Session agenda. <https://agenda.infn.it/event/31580>
- M. Junker et al., Cross section of  $^3He(^3He,2p)^4He$  measured at solar energies. *Phys. Rev. C* **57**(5), 2700–2710 (1998). <https://doi.org/10.1103/PhysRevC.57.2700>
- C. Arpesella, A low background counting facility at Laboratori Nazionali del Gran Sasso. *Appl. Rad. Isotop.* **47**(9), 991–996 (1996). [https://doi.org/10.1016/S0969-8043\(96\)00097-8](https://doi.org/10.1016/S0969-8043(96)00097-8). Proceedings of the International Committee for Radionuclide Metrology Conference on Low-level Measurement Techniques
- A. Formicola et al., The LUNA II 400 kV accelerator. *Nucl. Instrum. Methods Phys. Res. A* **507**(3), 609–616 (2003). [https://doi.org/10.1016/S0168-9002\(03\)01435-9](https://doi.org/10.1016/S0168-9002(03)01435-9)
- A. Sen et al., A high intensity, high stability 3.5 MV Singletron<sup>TM</sup> accelerator. *Nucl. Instrum. Methods Phys. Res. B* **450**, 390–395 (2019). <https://doi.org/10.1016/j.nimb.2018.09.016>
- F. Napolitano et al., Testing the Pauli exclusion principle with the VIP-2 experiment. *Symmetry* **14**(5), 893 (2022). <https://doi.org/10.3390/sym14050893>

19. A. Caciolli et al., Preparation and characterisation of isotopically enriched  $Ta_2O_5$  targets for nuclear astrophysics studies. *Eur. Phys. J. A* **48**, 144 (2012). <https://doi.org/10.1140/epja/i2012-12144-0>
20. F. Ferraro et al., A high-efficiency gas target setup for underground experiments, and redetermination of the branching ratio of the 189.5 keV  $^{22}Ne(p, \gamma)^{23}Na$  resonance. *Eur. Phys. J. A* **54**(3), 44 (2018). <https://doi.org/10.1140/epja/i2018-12476-7>
21. S. Donadi et al., Underground test of gravity-related wave function collapse. *Nat. Phys.* **17**(1), 74–78 (2020). <https://doi.org/10.1038/s41567-020-1008-4>
22. L. Baudis et al., Gator: a low-background counting facility at the Gran Sasso Underground Laboratory. *J. Instrum.* **6**(08), 08010 (2011). <https://doi.org/10.1088/1748-0221/6/08/P08010>
23. A. Boeltzig et al., Improved background suppression for radiative capture reactions at LUNA with HPGe and BGO detectors. *J. Phys. G Nucl. Part. Phys.* **45**(2), 025203 (2018). <https://doi.org/10.1088/1361-6471/aaa163>
24. J. Skowronski et al., Advances in radiative capture studies at LUNA with a segmented BGO detector. *J. Phys. G Nucl. Part. Phys.* **50**(4), 045201 (2023). <https://doi.org/10.1088/1361-6471/aca961>
25. L. Csedreki et al., Characterization of the LUNA neutron detector array for the measurement of the  $^{13}C(\alpha, n)^{16}O$  reaction. *Nucl. Instrum. Methods Phys. Res. A* **994**, 165081 (2021). <https://doi.org/10.1016/j.nima.2021.165081>
26. F. Cavanna et al., A new study of the  $^{22}Ne(p, \gamma)^{23}Na$  reaction deep underground: feasibility, setup and first observation of the 186 keV resonance. *Eur. Phys. J. A* **50**, 179 (2014). <https://doi.org/10.1140/epja/i2014-14179-5>
27. F. Confortola et al., Astrophysical  $S$  factor of the  $^3He(\alpha, \gamma)^7Be$  reaction measured at low energy via detection of prompt and delayed  $\gamma$  rays. *Phys. Rev. C* **75**(6), 065803 (2007). <https://doi.org/10.1103/PhysRevC.75.065803>
28. F. Terrasi et al., A new AMS facility in Caserta/Italy. *Nucl. Instrum. Methods Phys. Res. B* **259**(1), 14–17 (2007). <https://doi.org/10.1016/j.nimb.2007.01.139>
29. L. Gialanella et al., Off-line production of a  $^7Be$  radioactive ion beam. *Nucl. Instrum. Methods Phys. Res. B* **197**(1), 150–154 (2002). [https://doi.org/10.1016/S0168-583X\(02\)01386-1](https://doi.org/10.1016/S0168-583X(02)01386-1)
30. B.N. Limata et al.,  $^7Be$  radioactive beam production at CIRCE and its utilization in basic and applied physics. *Nucl. Instrum. Methods Phys. Res. B* **266**(10), 2117–2121 (2008). <https://doi.org/10.1016/j.nimb.2008.02.083>
31. D. Schürmann et al., A windowless hydrogen gas target for the measurement of  $^7Be(p, \gamma)^8B$  with the recoil separator ERNA. *Eur. Phys. J. A* **49**, 80 (2013). <https://doi.org/10.1140/epja/i2013-13080-1>
32. D. Rapagnani et al., A supersonic jet target for the cross section measurement of the  $^{12}C(\alpha, \gamma)^{16}O$  reaction with the recoil mass separator ERNA. *Nucl. Instrum. Methods Phys. Res. B* **407**, 217–221 (2017). <https://doi.org/10.1016/j.nimb.2017.07.003>
33. F. Brandi et al., Optical and spectroscopic study of a supersonic flowing helium plasma: energy transport in the afterglow. *Sci. Rep.* **10**, 5087 (2020). <https://doi.org/10.1038/s41598-020-61988-y>
34. D. Rogalla et al., Recoil separator ERNA: ion beam purification. *Nucl. Instrum. Methods Phys. Res. A* **437**(2), 266–273 (1999). [https://doi.org/10.1016/S0168-9002\(99\)00767-6](https://doi.org/10.1016/S0168-9002(99)00767-6)
35. M. Romoli et al., Development of a two-stage detection array for low-energy light charged particles in nuclear astrophysics applications. *Eur. Phys. J. A* **54**(8), 142 (2018). <https://doi.org/10.1140/epja/i2018-12575-5>
36. E.L. Morales-Gallegos, Carbon burning in stars: an experimental study of the  $^{12}C(^{12}C, p)^{23}Na$  reaction towards astrophysical energies. PhD thesis, The University of Edinburgh (2017). <http://hdl.handle.net/1842/28967>
37. K. Piscicchia et al., Strongest atomic physics bounds on noncommutative quantum gravity models. *Phys. Rev. Lett.* (2022). <https://doi.org/10.1103/physrevlett.129.131301>
38. K. Piscicchia et al., Experimental test of noncommutative quantum gravity by VIP-2 lead. *Phys. Rev. D* **107**(2), 200 (2023). <https://doi.org/10.1103/physrevd.107.026002>
39. M. Lulli, A. Marciano, K. Piscicchia, Stochastic Ricci Flow dynamics of the gravitationally induced wave-function collapse. *arXiv arXiv:2307.10136* (2023)
40. A. Addazi, P. Belli, R. Bernabei, A. Marciano, Testing noncommutative spacetimes and violations of the Pauli exclusion principle through underground experiments. *Comput. Phys. Commun.* **42**(9), 094001 (2018). <https://doi.org/10.1088/1674-1137/42/9/094001>
41. A. Addazi, P. Belli, R. Bernabei, A. Marciano, H. Shababi, Phenomenology of the Pauli exclusion principle violations due to the non-perturbative generalized uncertainty principle. *Eur. Phys. J. C* **80**, 1–7 (2020). <https://doi.org/10.1140/epjc/s10052-020-8401-0>
42. G. Amelino-Camelia, M. Arzano, A. Marciano, On the quantum-gravity phenomenology of multiparticle states. *Frascati Phys. Ser.* **43**, 155 (2007)
43. M. Arzano, Quantum fields, nonlocality and quantum group symmetries. *Phys. Rev. D* **77**(2), 025013 (2008). <https://doi.org/10.1103/PhysRevD.77.025013>
44. A. Addazi, A. Marciano, A modern guide to  $\theta$ -Poincaré. *Int. J. Mod. Phys. A* **35**(32), 2042003–385 (2020). <https://doi.org/10.1142/S0217751X20420038>
45. L. Diósi, A universal master equation for the gravitational violation of quantum mechanics. *Phys. Lett. A* **120**(8), 377–381 (1987). [https://doi.org/10.1016/0375-9601\(87\)90681-5](https://doi.org/10.1016/0375-9601(87)90681-5)
46. L. Diósi, Models for universal reduction of macroscopic quantum fluctuations. *Phys. Rev. A* **40**(3), 1165–1174 (1989). <https://doi.org/10.1103/PhysRevA.40.1165>
47. R. Penrose, On gravity's role in quantum state reduction. *Gen. Relativ. Gravit.* **28**(5), 581–600 (1996). <https://doi.org/10.1007/BF02105068>
48. R. Penrose, On the gravitization of quantum mechanics I: quantum state reduction. *Found. Phys.* **44**(5), 557–575 (2014). <https://doi.org/10.1007/s10701-013-9770-0>
49. E. Nelson, *Dynamical Theories of Brownian Motion* (Princeton University Press, Princeton, 1967)
50. E. Nelson, Derivation of the Schrödinger equation from Newtonian mechanics. *Phys. Rev.* **150**, 1079–1085 (1966). <https://doi.org/10.1103/PhysRev.150.1079>
51. F. Guerra, P. Ruggiero, New interpretation of the Euclidean-Markov field in the framework of physical Minkowski space-time. *Phys. Rev. Lett.* **31**, 1022–1025 (1973). <https://doi.org/10.1103/PhysRevLett.31.1022>
52. L. Smolin, Could quantum mechanics be an approximation to another theory?. *arXiv e-prints* (2006). <https://doi.org/10.48550/arXiv.quant-ph/0609109>
53. J.P. Desclaux, A multiconfiguration relativistic DIRAC-FOCK program. *Comput. Phys. Commun.* **9**(1), 31–45 (1975). [https://doi.org/10.1016/0010-4655\(75\)90054-5](https://doi.org/10.1016/0010-4655(75)90054-5)
54. H. Shi et al., Experimental search for the violation of Pauli exclusion principle. *Eur. Phys. J. C* (2018). <https://doi.org/10.1140/epjc/s10052-018-5802-4>
55. L.B. Okun', Possible violation of the Pauli principle in atoms. *J. Exp. Theor. Phys. Lett.* **46**, 529 (1987)
56. E. Fermi, Le ultime particelle costitutive della materia. *Scientia* **55**, 21–28 (1934)
57. E. Milotti, Enrico Fermi's view of identical particles. *arXiv arXiv:0705.1363* (2007)
58. G. Gentile, Osservazioni sopra le statistiche intermedie. *Il Nuovo Cimento* **17**(10), 493–497 (1940). <https://doi.org/10.1007/bf02960187>

59. G. Dell'Antonio, O. Greenberg, O. Sudarshan, Group Theoretical Concepts and Methods in Elementary Particle Physics. Lectures at the Istanbul Summer School of Theoretical Physics, 1962. Gordon and Breach, New York (1964)
60. A.Y. Ignatiev, V. Kuzmin, Is small violation of the Pauli principle possible? *Quarks* **86**, 263 (1987)
61. A.Y. Ignatiev, V. Kuzmin, Search for slight violation of the Pauli principle. *Yad. Fiz.* **46**, 786 (1987)
62. A.Y. Ignatiev, X rays test the Pauli exclusion principle. *Radiat. Phys. Chem.* **75**(11), 2090–2096 (2006). <https://doi.org/10.1016/j.radphyschem.2005.10.040>
63. V. Rahal, A. Campa, Thermodynamical implications of a violation of the Pauli principle. *Phys. Rev. A* **38**(7), 3728–3731 (1988). <https://doi.org/10.1103/physreva.38.3728>
64. O.W. Greenberg, R.N. Mohapatra, Local quantum field theory of possible violation of the Pauli principle. *Phys. Rev. Lett.* **59**(22), 2507–2510 (1987). <https://doi.org/10.1103/physrevlett.59.2507>
65. O.W. Greenberg, Example of infinite statistics. *Phys. Rev. Lett.* **64**(7), 705–708 (1990). <https://doi.org/10.1103/physrevlett.64.705>
66. K. Piscicchia et al., Search for a remnant violation of the Pauli exclusion principle in a roman lead target. *Eur. Phys. J. C* (2020). <https://doi.org/10.1140/epjc/s10052-020-8040-5>
67. A.M.L. Messiah, O.W. Greenberg, Symmetrization postulate and its experimental foundation. *Phys. Rev.* **136**(1B), 248–267 (1964). <https://doi.org/10.1103/physrev.136.b248>
68. A.P. Balachandran, G. Mangano, A. Pinzul, S. Vaidya, Spin and statistics on the Groenewold-Moyal plane: Pauli-forbidden levels and transitions. *Int. J. Mod. Phys. A* **21**(15), 3111–3126 (2006). <https://doi.org/10.1142/S0217751X06031764>
69. A.P. Balachandran et al., Statistics and UV-IR mixing with twisted Poincaré invariance. *Phys. Rev. D* **75**(4), 045009 (2007). <https://doi.org/10.1103/PhysRevD.75.045009>
70. N.E. Mavromatos, Models & searches of CPT violation: a personal, very partial, list. *Eur. Phys. J. Web Conf.* **166**, 00005 (2018). <https://doi.org/10.1051/epjconf/201816600005>
71. C. Curceanu et al., Experimental tests of quantum mechanics—Pauli exclusion principle violation (the VIP experiment) and future perspective. *J. Phys. Conf. Ser.* **306**, 012036 (2011). <https://doi.org/10.1088/1742-6596/306/1/012036>
72. L. Sperandio, New experimental limit on the Pauli exclusion principle violation by electrons from the VIP experiment. PhD thesis, Università degli Studi di Roma “Tor Vergata” (2008)
73. C. Curceanu et al., Test of the Pauli exclusion principle in the VIP-2 underground experiment. *Entropy* **19**(7), 300 (2017). <https://doi.org/10.3390/e19070300>
74. K. Piscicchia et al., VIP-2—high-sensitivity tests on the Pauli exclusion principle for electrons. *Entropy* **22**(11), 1195 (2020). <https://doi.org/10.3390/e22111195>
75. E. Ramberg, G.A. Snow, Experimental limit on a small violation of the Pauli principle. *Phys. Lett. B* **238**(2–4), 438–441 (1990). [https://doi.org/10.1016/0370-2693\(90\)91762-z](https://doi.org/10.1016/0370-2693(90)91762-z)
76. E. Milotti et al., On the importance of electron diffusion in a bulk-matter test of the Pauli exclusion principle. *Entropy* **20**(7), 515 (2018). <https://doi.org/10.3390/e20070515>
77. E. Milotti et al., Semi-analytical monte Carlo method to simulate the signal of the VIP-2 experiment. *Symmetry* **13**(1), 6 (2020). <https://doi.org/10.3390/sym13010006>
78. K. Piscicchia et al., High sensitivity Pauli Exclusion Principle tests by the VIP experiment: status and perspectives. *Acta Phys. Pol. A* **142**(3), 361–366 (2022). <https://doi.org/10.12693/APhysPolA.142.361>
79. S.R. Elliott et al., An improved limit on Pauli-Exclusion-Principle forbidden atomic transitions. *Found. Phys.* **42**(8), 1015–1030 (2012). <https://doi.org/10.1007/s10701-012-9643-y>
80. P. Holl et al., Deep learning based pulse shape discrimination for germanium detectors. *Eur. Phys. J. C* (2019). <https://doi.org/10.1140/epjc/s10052-019-6869-2>
81. E. Schrödinger, Die gegenwärtige Situation in der Quantenmechanik. *Naturwissenschaften* **23**(49), 823–828 (1935). <https://doi.org/10.1007/BF01491914>
82. A.J. Leggett, Macroscopic quantum systems and the quantum theory of measurement. *Prog. Theor. Phys. Supp.* **69**, 80–100 (1980). <https://doi.org/10.1143/PTP.69.80>
83. S. Weinberg, Precision tests of quantum mechanics. *Phys. Rev. Lett.* **62**, 485 (2014). [https://doi.org/10.1142/9789814571616\\_0005](https://doi.org/10.1142/9789814571616_0005)
84. J.S. Bell, A. Aspect, *Speakable and Unsayable in Quantum Mechanics* (Cambridge University Press, Cambridge, 2004)
85. G.C. Ghirardi, A. Rimini, T. Weber, Unified dynamics for microscopic and macroscopic systems. *Phys. Rev. D* **34**, 470–491 (1986). <https://doi.org/10.1103/physrevd.34.470>
86. S.L. Adler, *Quantum Theory as an Emergent Phenomenon* (Cambridge University Press, Cambridge, 2004). <https://doi.org/10.1017/cbo9780511535277>
87. S. Weinberg, Collapse of the state vector. *Phys. Rev. A* **85**(6), 062116 (2012). <https://doi.org/10.1103/PhysRevA.85.062116>
88. R. Howl, R. Penrose, I. Fuentes, Exploring the unification of quantum theory and general relativity with a Bose-Einstein condensate. *New J. Phys.* **21**(4), 043047 (2019). <https://doi.org/10.1088/1367-2630/ab104a>
89. P. Pearle, Combining stochastic dynamical state-vector reduction with spontaneous localization. *Phys. Rev. A* **39**(5), 2277–2289 (1989). <https://doi.org/10.1103/physreva.39.2277>
90. G.C. Ghirardi, P. Pearle, A. Rimini, Markov processes in Hilbert space and continuous spontaneous localization of systems of identical particles. *Phys. Rev. A* **42**, 78–89 (1990). <https://doi.org/10.1103/physreva.42.78>
91. S. Donadi et al., Novel CSL bounds from the noise-induced radiation emission from atoms. *Eur. Phys. J. C* (2021). <https://doi.org/10.1140/epjc/s10052-021-09556-0>
92. I.J. Arnquist et al., Search for spontaneous radiation from wave function collapse in the Majorana Demonstrator. *Phys. Rev. Lett.* **129**, 080401 (2022). <https://doi.org/10.1103/PhysRevLett.129.080401>
93. M. Bilardello, A. Trombettoni, A. Bassi, Collapse in ultracold Bose Josephson junctions. *Phys. Rev. A* **95**, 032134 (2017). <https://doi.org/10.1103/PhysRevA.95.032134>
94. M. Bilardello, S. Donadi, A. Vinante, A. Bassi, Bounds on collapse models from cold-atom experiments. *Phys. A* **462**, 764–782 (2016). <https://doi.org/10.1016/j.physa.2016.06.134>
95. M. Carlesso, A. Bassi, P. Falferi, A. Vinante, Experimental bounds on collapse models from gravitational wave detectors. *Phys. Rev. D* **94**, 124036 (2016). <https://doi.org/10.1103/PhysRevD.94.124036>
96. A. Vinante et al., Narrowing the parameter space of collapse models with ultracold layered force sensors. *Phys. Rev. Lett.* **125**, 100404 (2020). <https://doi.org/10.1103/PhysRevLett.125.100404>
97. A. Vinante et al., Improved noninterferometric test of collapse models using ultracold cantilevers. *Phys. Rev. Lett.* **119**, 110401 (2017). <https://doi.org/10.1103/PhysRevLett.119.110401>

98. A. Vinante et al., Upper bounds on spontaneous wave-function collapse models using millikelvin-cooled nanocantilevers. *Phys. Rev. Lett.* **116**, 090402 (2016). <https://doi.org/10.1103/PhysRevLett.116.090402>
99. S.L. Adler, A. Vinante, Bulk heating effects as tests for collapse models. *Phys. Rev. A* **97**, 052119 (2018). <https://doi.org/10.1103/PhysRevA.97.052119>
100. M. Bahrami, Testing collapse models by a thermometer. *Phys. Rev. A* **97**, 052118 (2018). <https://doi.org/10.1103/PhysRevA.97.052118>
101. K. Piscicchia et al., CSL collapse model mapped with the spontaneous radiation. *Entropy* **19**(7), 319 (2017). <https://doi.org/10.3390/e19070319>
102. M. Toroš, A. Bassi, Bounds on quantum collapse models from matter-wave interferometry: calculational details. *J. Phys. A Math. Theor.* **51**(11), 115302 (2018). <https://doi.org/10.1088/1751-8121/aaabc6>
103. S.L. Adler, Lower and upper bounds on CSL parameters from latent image formation and IGM heating. *J. Phys. A Math. Theor.* **40**(12), 2935–2957 (2007). <https://doi.org/10.1088/1751-8113/40/12/s03>
104. A. Bassi, D.-A. Deckert, L. Ferialdi, Breaking quantum linearity: constraints from human perception and cosmological implications. *Europhys. Lett.* **92**(5), 50006 (2010). <https://doi.org/10.1209/0295-5075/92/50006>
105. C.E. Rolfs, W.S. Rodney, *Cauldrons in the Cosmos* (The University of Chicago Press, Chicago, 1988)
106. M. Freer et al., Limits for the  $3\alpha$  branching ratio of the decay of the 7.65 MeV,  $0_2^+$  state in  $^{12}\text{C}$ . *Phys. Rev. C* **49**(4), 1751–1754 (1994). <https://doi.org/10.1103/PhysRevC.49.R1751>
107. T. Kibédi et al., Radiative width of the Hoyle state from  $\gamma$ -ray spectroscopy. *Phys. Rev. Lett.* **125**(18), 182701 (2020). <https://doi.org/10.1103/PhysRevLett.125.182701>
108. T. Akahori, Y. Funaki, K. Yabana, Imaginary-time formalism for triple- $\alpha$  reaction rates. *Phys. Rev. C* **92**, 022801 (2015). <https://doi.org/10.1103/PhysRevC.92.022801>
109. H. Suno, Y. Suzuki, P. Descouvemont, Triple- $\alpha$  continuum structure and Hoyle resonance of  $^{12}\text{C}$  using the hyperspherical slow variable discretization. *Phys. Rev. C* **91**(1), 014004 (2015). <https://doi.org/10.1103/PhysRevC.91.014004>
110. C. Angulo et al., A compilation of charged-particle induced thermonuclear reaction rates. *Nucl. Phys. A* **656**(1), 3–183 (1999). [https://doi.org/10.1016/S0375-9474\(99\)00030-5](https://doi.org/10.1016/S0375-9474(99)00030-5)
111. S. Ishikawa, Decay and structure of the Hoyle state. *Phys. Rev. C* **90**(6), 061604 (2014). <https://doi.org/10.1103/PhysRevC.90.061604>
112. H. Morinaga, Interpretation of some of the excited states of  $4n$  self-conjugate nuclei. *Phys. Rev.* **101**, 254–258 (1956). <https://doi.org/10.1103/PhysRev.101.254>
113. W. von Oertzen, Dimers based on the  $\alpha$ - $\alpha$  potential and chain states of carbon isotopes. *Z. Phys. A* **357**(4), 355–365 (1997). <https://doi.org/10.1007/s002180050255>
114. E. Uegaki, S. Okabe, Y. Abe, H. Tanaka, Structure of the excited states in  $^{12}\text{C}$ . *I. Prog. Theor. Phys.* **57**(4), 1262 (1977). <https://doi.org/10.1143/PTP.57.1262>
115. M. Kamimura, Transition densities between the  $0_1^+$ ,  $2_1^+$ ,  $4_1^+$ ,  $0_2^+$ ,  $2_2^+$ ,  $1_1^-$  and  $3_1^-$  states in  $^{12}\text{C}$  derived from the three-alpha resonating-group wave functions. *Nucl. Phys. A* **351**(3), 456–480 (1981). [https://doi.org/10.1016/0375-9474\(81\)90182-2](https://doi.org/10.1016/0375-9474(81)90182-2)
116. A. Tohsaki, H. Horiuchi, P. Schuck, G. Röpke, Alpha cluster condensation in  $^{12}\text{C}$  and  $^{16}\text{O}$ . *Phys. Rev. Lett.* **87**, 192501 (2001). <https://doi.org/10.1103/PhysRevLett.87.192501>
117. M. Chernykh et al., Structure of the Hoyle state in  $^{12}\text{C}$ . *Phys. Rev. Lett.* **98**, 032501 (2007). <https://doi.org/10.1103/PhysRevLett.98.032501>
118. E. Epelbaum, H. Krebs, D. Lee, U.-G. Meißner, Ab initio calculation of the Hoyle state. *Phys. Rev. Lett.* **106**(19), 192501 (2011). <https://doi.org/10.1103/PhysRevLett.106.192501>
119. A.R. Raduta et al., Evidence for  $\alpha$ -particle condensation in nuclei from the Hoyle state deexcitation. *Phys. Lett. B* **705**(1–2), 65–70 (2011). <https://doi.org/10.1016/j.physletb.2011.10.008>
120. J. Manfredi et al.,  $\alpha$  decay of the excited states in  $^{12}\text{C}$  at 7.65 and 9.64 MeV. *Phys. Rev. C* **85**(3), 037603 (2012). <https://doi.org/10.1103/PhysRevC.85.037603>
121. O.S. Kirsebom et al., Improved limit on direct  $\alpha$  decay of the Hoyle state. *Phys. Rev. Lett.* **108**(20), 202501 (2012). <https://doi.org/10.1103/PhysRevLett.108.202501>
122. T.K. Rana et al., Estimation of direct components of the decay of the Hoyle state. *Phys. Rev. C* **88**(2), 021601 (2013). <https://doi.org/10.1103/PhysRevC.88.021601>
123. M. Itoh et al., Further improvement of the upper limit on the direct  $3\alpha$  decay from the Hoyle state in  $^{12}\text{C}$ . *Phys. Rev. Lett.* **113**(10), 102501 (2014). <https://doi.org/10.1103/PhysRevLett.113.102501>
124. D. Dell’Aquila et al., High-precision probe of the fully sequential decay width of the Hoyle state in  $^{12}\text{C}$ . *Phys. Rev. Lett.* **119**(13), 132501 (2017). <https://doi.org/10.1103/PhysRevLett.119.132501>
125. R. Smith et al., New measurement of the direct  $3\alpha$  decay from the  $^{12}\text{C}$  Hoyle state. *Phys. Rev. Lett.* **119**(13), 132502 (2017). <https://doi.org/10.1103/PhysRevLett.119.132502>
126. T.K. Rana et al., New high precision study on the decay width of the Hoyle state in  $^{12}\text{C}$ . *Phys. Lett. B* **793**, 130–133 (2019). <https://doi.org/10.1016/j.physletb.2019.04.028>
127. J. Bishop et al., Almost medium-free measurement of the Hoyle state direct-decay component with a TPC. *Phys. Rev. C* **102**(4), 041303 (2020). <https://doi.org/10.1103/PhysRevC.102.041303>
128. R. Bijker, F. Iachello, Cluster states in nuclei as representations of a  $U(\nu+1)$  group. *Phys. Rev. C* **61**(6), 067305 (2000). <https://doi.org/10.1103/PhysRevC.61.067305>
129. D.J. Marín-Lámbarri et al., Evidence for triangular  $D_{3h}$  symmetry in  $^{12}\text{C}$ . *Phys. Rev. Lett.* **113**(1), 012502 (2014). <https://doi.org/10.1103/PhysRevLett.113.012502>
130. G. Cardella et al., Potential experimental evidence of an Efimov state in  $^{12}\text{C}$  and its influence on astrophysical carbon creation, in *EPJ Web of Conferences*, vol. 279 (2023), p. 03001. <https://doi.org/10.1051/epjconf/202327903001>
131. K.C.W. Li et al., Investigating the predicted breathing-mode excitation of the Hoyle state. *Phys. Lett. B* **827**, 136928 (2022). <https://doi.org/10.1016/j.physletb.2022.136928>
132. P.G. Prada Moroni, O. Straniero, Calibration of white dwarf cooling sequences: theoretical uncertainty. *Astrophys. J.* **581**(1), 585–597 (2002). <https://doi.org/10.1086/344052>
133. I. Domínguez, P. Höflich, O. Straniero, Constraints on the progenitors of Type Ia supernovae and implications for the cosmological equation of state. *Astrophys. J.* **557**(1), 279–291 (2001). <https://doi.org/10.1086/321661>
134. G. Imbriani et al., The  $^{12}\text{C}(\alpha, \gamma)^{16}\text{O}$  reaction rate and the evolution of stars in the mass range  $0.8 \leq M/M_{\odot} \leq 25$ . *Astrophys. J.* **558**(2), 903–915 (2001). <https://doi.org/10.1086/322288>
135. R.J. deBoer et al., The  $^{12}\text{C}(\alpha, \gamma)^{16}\text{O}$  reaction and its implications for stellar helium burning. *Rev. Mod. Phys.* **89**(3), 035007 (2017). <https://doi.org/10.1103/RevModPhys.89.035007>

136. A.I. Karakas, J.C. Lattanzio, The Dawes review 2: nucleosynthesis and stellar yields of low- and intermediate-mass single stars. *Publ. Astron. Soc. Austral.* **31**, 030 (2014). <https://doi.org/10.1017/pasa.2014.21>
137. M. Pignatari et al., The weak  $s$ -process in massive stars and its dependence on the neutron capture cross sections. *Astrophys. J.* **710**(2), 1557–1577 (2010). <https://doi.org/10.1088/0004-637X/710/2/1557>
138. F. Käppeler, R. Gallino, S. Bisterzo, W. Aoki, The  $s$  process: nuclear physics, stellar models, and observations. *Rev. Mod. Phys.* **83**(1), 157–194 (2011). <https://doi.org/10.1103/RevModPhys.83.157>
139. C.M. Raiteri et al.,  $s$ -Process nucleosynthesis in massive stars and the weak component. I. Evolution and neutron captures in a  $25 M_{\odot}$  star. *Astrophys. J.* **367**, 228 (1991). <https://doi.org/10.1086/169622>
140. F. Käppeler et al., Reaction rates for  $^{18}\text{O}(\alpha, \gamma)^{22}\text{Ne}$ ,  $^{22}\text{Ne}(\alpha, \gamma)^{26}\text{Mg}$ , and  $^{22}\text{Ne}(\alpha, n)^{25}\text{Mg}$  in stellar helium burning and  $s$ -process nucleosynthesis in massive stars. *Astrophys. J.* **437**, 396 (1994). <https://doi.org/10.1086/175004>
141. N. Prantzos, M. Hashimoto, K. Nomoto, The  $s$ -process in massive stars: yields as a function of stellar mass and metallicity. *Astron. Astrophys.* **234**, 211 (1990)
142. I. Baraffe, M.F. El Eid, N. Prantzos, The  $s$ -process in massive stars of variable composition. *Astron. Astrophys.* **258**(2), 357–367 (1992)
143. M. Pignatari et al., The  $s$ -process in massive stars at low metallicity: the effect of primary  $^{14}\text{N}$  from fast rotating stars. *Astrophys. J.* **687**, 95–98 (2008). <https://doi.org/10.1086/593350>
144. G. Cescutti et al., The  $s$ -process in the Galactic halo: the fifth signature of spinstars in the early Universe? *Astron. Astrophys.* **553**, 51 (2013). <https://doi.org/10.1051/0004-6361/201220809>
145. N. Prantzos et al., Chemical evolution with rotating massive star yields II. A new assessment of the solar  $s$ - and  $r$ -process components. *Mon. Not. R. Astron. Soc.* **491**(2), 1832–1850 (2020). <https://doi.org/10.1093/mnras/stz3154>
146. M. Limongi, A. Chieffi, Presupernova evolution and explosive nucleosynthesis of rotating massive stars in the metallicity range  $-3 \leq [\text{Fe}/\text{H}] \leq 0$ . *Astrophys. J. Suppl. Ser.* **237**(1), 13 (2018). <https://doi.org/10.3847/1538-4365/aacb24>
147. D. Yong, W. Aoki, D.L. Lambert, Mg isotope ratios in giant stars of the globular clusters M13 and M71. *Astrophys. J.* **638**(2), 1018–1027 (2006). <https://doi.org/10.1086/498974>
148. O. Straniero et al., Radiative  $^{13}\text{C}$  burning in Asymptotic Giant Branch stars and  $s$ -processing. *Astrophys. J. Lett.* **440**, 85 (1995). <https://doi.org/10.1086/187767>
149. R. Gallino et al., Evolution and nucleosynthesis in low-mass Asymptotic Giant Branch stars. II. Neutron capture and the  $s$ -process. *Astrophys. J.* **497**(1), 388–403 (1998). <https://doi.org/10.1086/305437>
150. O. Straniero, R. Gallino, S. Cristallo,  $s$  process in low-mass Asymptotic Giant Branch stars. *Nucl. Phys. A* **777**, 311–339 (2006). <https://doi.org/10.1016/j.nuclphysa.2005.01.011>
151. A. Tumino et al., An increase in the  $^{12}\text{C} + ^{12}\text{C}$  fusion rate from resonances at astrophysical energies. *Nature* **557**, 687–690 (2018). <https://doi.org/10.1038/s41586-018-0149-4>
152. C.L. Jiang, K.E. Rehm, B.B. Back, R.V.F. Janssens, Expectations for  $^{12}\text{C}$  and  $^{16}\text{O}$  induced fusion cross sections at energies of astrophysical interest. *Phys. Rev. C* **75**, 015803 (2007). <https://doi.org/10.1103/PhysRevC.75.015803>
153. A. Chieffi et al., Impact of the new measurement of the  $^{12}\text{C} + ^{12}\text{C}$  fusion cross section on the final compactness of massive stars. *Astrophys. J.* **916**(2), 79 (2021). <https://doi.org/10.3847/1538-4357/ac06ca>
154. E. Bravo et al., Type Ia supernovae and the  $^{12}\text{C} + ^{12}\text{C}$  reaction rate. *Astron. Astrophys.* **535**, 114 (2011). <https://doi.org/10.1051/0004-6361/201117814>
155. O. Straniero, L. Piersanti, I. Dominguez, A. Tumino, On the mass of supernova progenitors: the role of the  $^{12}\text{C} + ^{12}\text{C}$  reaction, in *Nuclei in the Cosmos XV*, vol. 219 (2019), pp. 7–11. [https://doi.org/10.1007/978-3-030-13876-9\\_2](https://doi.org/10.1007/978-3-030-13876-9_2)
156. L. Piersanti et al., Pre-explosive accretion and simmering phases of SNe Ia. *Astrophys. J.* **926**(1), 103 (2022). <https://doi.org/10.3847/1538-4357/ac403b>
157. E. Bravo,  $^{16}\text{O}(p,\alpha)^{13}\text{N}$  makes explosive oxygen burning sensitive to the metallicity of the progenitors of type Ia supernovae. *Astron. Astrophys.* **627**, 146 (2019). <https://doi.org/10.1051/0004-6361/201936024>
158. M. Lugaro et al., Origin of meteoritic stardust unveiled by a revised proton-capture rate of  $^{17}\text{O}$ . *Nat. Astron.* **1**, 0027 (2017). <https://doi.org/10.1038/s41550-016-0027>
159. F. Ferraro et al., Direct capture cross section and the  $E_p = 71$  and 105 keV resonances in the  $^{22}\text{Ne}(p, \gamma)^{23}\text{Na}$  reaction. *Phys. Rev. Lett.* **121**, 172701 (2018). <https://doi.org/10.1103/PhysRevLett.121.172701>
160. A. Boeltzig et al., Direct measurements of low-energy resonance strengths of the  $^{23}\text{Na}(p, \gamma)^{24}\text{Mg}$  reaction for astrophysics. *Phys. Lett. B* **795**, 122–128 (2019). <https://doi.org/10.1016/j.physletb.2019.05.044>
161. V. Mossa et al., The baryon density of the universe from an improved rate of deuterium burning. *Nature* **587**, 210 (2020). <https://doi.org/10.1038/s41586-020-2878-4>
162. G.F. Ciani et al., Direct Measurement of the  $^{13}\text{C}(\alpha, n)^{16}\text{O}$  Cross Section into the  $s$ -Process Gamow Peak. *Phys. Rev. Lett.* **127**, 152701 (2021). <https://doi.org/10.1103/PhysRevLett.127.152701>
163. L. Gialanella et al., Absolute cross section of  $p(^7\text{Be}, \gamma)^8\text{B}$  using a novel approach. *Eur. Phys. J. A* **7**(3), 303–305 (2000). <https://doi.org/10.1007/PL00013599>
164. D. Rogalla et al., Recoil separator ERNA: acceptances in angle and energy. *Nucl. Instrum. Methods Phys. Res. A* **513**(3), 573–578 (2003). <https://doi.org/10.1016/j.nima.2003.07.001>
165. L. Gialanella et al., Recoil separator ERNA: gas target and beam suppression. *Nucl. Instrum. Methods Phys. Res. A* **522**(3), 432–438 (2004). <https://doi.org/10.1016/j.nima.2003.11.386>
166. D. Schürmann et al., Recoil separator ERNA: charge state distribution, target density, beam heating, and longitudinal acceptance. *Nucl. Instrum. Methods Phys. Res. A* **531**(3), 428–434 (2004). <https://doi.org/10.1016/j.nima.2004.05.131>
167. D. Schürmann et al., First direct measurement of the total cross-section of  $^{12}\text{C}(\alpha, \gamma)^{16}\text{O}$ . *Eur. Phys. J. A* **26**(2), 301–305 (2005). <https://doi.org/10.1140/epja/i2005-10175-2>
168. C. Matei et al., Measurement of the cascade transition via the first excited state of  $^{16}\text{O}$  in the  $^{12}\text{C}(\alpha, \gamma)^{16}\text{O}$  reaction, and its  $S$  factor in stellar helium burning. *Phys. Rev. Lett.* **97**(24), 242503 (2006). <https://doi.org/10.1103/PhysRevLett.97.242503>
169. D. Schürmann et al., Study of the 6.05 MeV cascade transition in  $^{12}\text{C}(\alpha, \gamma)^{16}\text{O}$ . *Phys. Lett. B* **703**(5), 557–561 (2011). <https://doi.org/10.1016/j.physletb.2011.08.061>
170. A. Di Leva et al., Recoil separator ERNA: measurement of  $^3\text{He}(\alpha, \gamma)^7\text{Be}$ . *Nucl. Instrum. Methods Phys. Res. A* **595**(2), 381–390 (2008). <https://doi.org/10.1016/j.nima.2008.07.082>
171. A. Di Leva et al.,  $^{14,15}\text{N}$  beam from cyanide compounds. *Nucl. Instrum. Methods Phys. Res. A* **689**, 98–101 (2012). <https://doi.org/10.1016/j.nima.2012.06.037>



172. A. Di Leva et al., Measurement of 1323 and 1487 keV resonances in  $^{15}\text{N}(\alpha, \gamma)^{19}\text{F}$  with the recoil separator ERNA. *Phys. Rev. C* **95**(4), 045803 (2017). <https://doi.org/10.1103/PhysRevC.95.045803>
173. R. Buompane et al., Test measurement of  $^7\text{Be}(\text{p}, \gamma)^8\text{B}$  with the recoil mass separator ERNA. *Eur. Phys. J. A* **54**(6), 92 (2018). <https://doi.org/10.1140/epja/i2018-12522-6>
174. R. Buompane et al., Determination of the  $^7\text{Be}(\text{p}, \gamma)^8\text{B}$  cross section at astrophysical energies using a radioactive  $^7\text{Be}$  ion beam. *Phys. Lett. B* **824**, 136819 (2021). <https://doi.org/10.1016/j.physletb.2021.136819>
175. L. Morales-Gallegos et al., Reduction of deuterium content in carbon targets for  $^{12}\text{C} + ^{12}\text{C}$  reaction studies of astrophysical interest. *Eur. Phys. J. A* **54**(8), 132 (2018). <https://doi.org/10.1140/epja/i2018-12564-8>
176. R.J. Cooke, M. Pettini, C.C. Steidel, One percent determination of the primordial deuterium abundance. *Astrophys. J.* **855**(2), 102 (2018). <https://doi.org/10.3847/1538-4357/aaab53>
177. C. Pitrou, A. Coc, J.-P. Uzan, E. Vangioni, Precision big bang nucleosynthesis with improved Helium-4 predictions. *Phys. Rep.* **754**, 1–66 (2018). <https://doi.org/10.1016/j.physrep.2018.04.005>
178. A. Coc et al., New reaction rates for improved primordial D / H calculation and the cosmic evolution of deuterium. *Phys. Rev. D* **92**, 123526 (2015). <https://doi.org/10.1103/PhysRevD.92.123526>
179. V. Mossa et al., Setup commissioning for an improved measurement of the  $\text{D}(\text{p}, \gamma)^3\text{He}$  cross section at Big Bang Nucleosynthesis energies. *Eur. Phys. J. A* **56**, 144 (2020). <https://doi.org/10.1140/epja/s10050-020-00149-1>
180. M. Viviani et al., Photodisintegration and electrodisintegration of  $^3\text{He}$  at threshold and  $\text{p d}$  radiative capture. *Phys. Rev. C* **61**, 064001 (2000). <https://doi.org/10.1103/PhysRevC.61.064001>
181. L.E. Marcucci et al., Electromagnetic structure of  $A = 2$  and 3 nuclei and the nuclear current operator. *Phys. Rev. C* **72**, 014001 (2005). <https://doi.org/10.1103/PhysRevC.72.014001>
182. L.E. Marcucci, G. Mangano, A. Kievsky, M. Viviani, Implication of the proton-deuteron radiative capture for Big Bang Nucleosynthesis. *Phys. Rev. Lett.* **116**(10), 102501 (2016). <https://doi.org/10.1103/PhysRevLett.116.102501>. [Erratum: *Phys. Rev. Lett.* **117**, 049901 (2016)]
183. M. Anders et al., First direct measurement of the  $^2\text{H}(\alpha, \gamma)^6\text{Li}$  cross section at Big Bang energies and the primordial lithium problem. *Phys. Rev. Lett.* **113**, 042501 (2014). <https://doi.org/10.1103/PhysRevLett.113.042501>
184. D. Trezzi et al., Big Bang  $^6\text{Li}$  nucleosynthesis studied deep underground. *Astropart. Phys.* **89**, 57–65 (2017). <https://doi.org/10.1016/j.astropartphys.2017.01.007>
185. J. Kiener et al., Measurements of the coulomb dissociation cross section of 156 MeV  $^6\text{Li}$  projectiles at extremely low relative fragment energies of astrophysical interest. *Phys. Rev. C* **44**, 2195–2208 (1991). <https://doi.org/10.1103/PhysRevC.44.2195>
186. F. Hammache et al., High-energy breakup of  $^6\text{Li}$  as a tool to study the big bang nucleosynthesis reaction  $^2\text{H}(\alpha, \gamma)^6\text{Li}$ . *Phys. Rev. C* **82**, 065803 (2010). <https://doi.org/10.1103/PhysRevC.82.065803>
187. X. Zhang, K.M. Nollett, D.R. Phillips,  $s$ -factor and scattering-parameter extractions from  $^3\text{He} + ^4\text{He} \rightarrow ^7\text{Be} + \gamma$ . *J. Phys. G Nucl. Part. Phys.* **47**(5), 054002 (2020). <https://doi.org/10.1088/1361-6471/ab6a71>
188. A. Di Leva et al., Stellar and primordial nucleosynthesis of  $^7\text{Be}$ : Measurement of  $^3\text{He}(\alpha, \gamma)^7\text{Be}$ . *Phys. Rev. Lett.* **102**(23), 232502 (2009). <https://doi.org/10.1103/PhysRevLett.102.232502>. Erratum: [*Phys. Rev. Lett.* **103**, 159903 (2009)]
189. F. Cavanna et al., Three new low-energy resonances in the  $^{22}\text{Ne}(\text{p}, \gamma)^{23}\text{Na}$  reaction. *Phys. Rev. Lett.* **115**, 252501 (2015). <https://doi.org/10.1103/PhysRevLett.115.252501>
190. A. Coc, E. Vangioni-Flam, P. Descouvemont, A. Adahchour, C. Angulo, Updated big bang nucleosynthesis compared with Wilkinson Microwave Anisotropy Probe observations and the abundance of light elements. *Astrophys. J.* **600**(2), 544 (2004). <https://doi.org/10.1086/380121>
191. B.D. Fields, The primordial lithium problem. *Annu. Rev. Nucl. Part. Sci.* **61**(1), 47–68 (2011). <https://doi.org/10.1146/annurev-nucl-102010-130445>
192. R.H. Cyburt, B.D. Fields, K.A. Olive, T.-H. Yeh, Big bang nucleosynthesis: present status. *Rev. Mod. Phys.* **88**, 015004 (2016). <https://doi.org/10.1103/RevModPhys.88.015004>
193. L. Sbordone et al., The metal-poor end of the spite plateau. I. Stellar parameters, metallicities, and lithium abundances. *Astron. Astrophys.* **522**, 26 (2010). <https://doi.org/10.1051/0004-6361/200913282>
194. A. Tumino et al., The Trojan Horse Method: a nuclear physics tool for astrophysics. *Annu. Rev. Nucl. Part. Sci.* **71**(1), 345–376 (2021). <https://doi.org/10.1146/annurev-nucl-102419-033642>
195. L. Lamia et al., On the determination of the  $^7\text{Be}(\text{n}, \alpha)^4\text{He}$  reaction cross section at BBN energies. *Astrophys. J.* **850**(2), 175 (2017). <https://doi.org/10.3847/1538-4357/aa965c>
196. L. Lamia et al., Cross-section measurement of the cosmologically relevant  $^7\text{Be}(\text{n}, \alpha)^4\text{He}$  reaction over a broad energy range in a single experiment. *Astrophys. J.* **879**(1), 23 (2019). <https://doi.org/10.3847/1538-4357/ab2234>
197. F. Farinon et al., Commissioning of the EXOTIC beam line. *Nucl. Instrum. Methods Phys. Res. B* **266**(19–20), 4097–4102 (2008). <https://doi.org/10.1016/j.nimb.2008.05.128>
198. S. Hayakawa et al., Constraining the primordial lithium abundance: New cross section measurement of the  $^7\text{Be} + \text{n}$  reactions updates the total  $^7\text{Be}$  destruction rate. *Astrophys. J. Lett.* **915**(1), 13 (2021). <https://doi.org/10.3847/2041-8213/ac061f>
199. S.M. Ali et al., Resonance excitations in  $^7\text{Be}(\text{d}, \text{p})^8\text{Be}^*$  to address the cosmological lithium problem. *Phys. Rev. Lett.* **128**(25), 252701 (2022). <https://doi.org/10.1103/PhysRevLett.128.252701>
200. E.G. Adelberger et al., Solar fusion cross sections. II. The pp chain and CNO cycles. *Rev. Mod. Phys.* **83**, 195–246 (2011). <https://doi.org/10.1103/RevModPhys.83.195>
201. R.H. Cyburt, B. Davids, B.K. Jennings, Determination of  $S_{17}(0)$  from published data. *Phys. Rev. C* **70**, 045801 (2004). <https://doi.org/10.1103/PhysRevC.70.045801>
202. M. Wiescher et al., The cold and hot CNO cycles. *Annu. Rev. Nucl. Part. Sci.* **60**(1), 381–404 (2010). <https://doi.org/10.1146/annurev.nucl.012809.104505>
203. Q. Li et al., Cross section measurement of  $^{14}\text{N}(\text{p}, \gamma)^{15}\text{O}$  in the CNO cycle. *Phys. Rev. C* **93**, 055806 (2016). <https://doi.org/10.1103/PhysRevC.93.055806>
204. L. Wagner et al., Astrophysical  $S$  factor of the  $^{14}\text{N}(\text{p}, \gamma)^{15}\text{O}$  reaction at 0.4–1.3 MeV. *Phys. Rev. C* **97**, 015801 (2018). <https://doi.org/10.1103/PhysRevC.97.015801>
205. G. Gyürky et al., Activation cross section measurement of the  $^{14}\text{N}(\text{p}, \gamma)^{15}\text{O}$  astrophysical key reaction. *Phys. Rev. C* **105**, 022801 (2022). <https://doi.org/10.1103/PhysRevC.105.L022801>
206. B. Frentz et al., Investigation of the  $^{14}\text{N}(\text{p}, \gamma)^{15}\text{O}$  reaction and its impact on the CNO cycle. *Phys. Rev. C* **106**(6), 065803 (2022). <https://doi.org/10.1103/PhysRevC.106.065803>
207. M. Marta et al., Resonance strengths in the  $^{14}\text{N}(\text{p}, \gamma)^{15}\text{O}$  and  $^{15}\text{N}(\text{p}, \alpha\gamma)^{12}\text{C}$  reactions. *Phys. Rev. C* **81**, 055807 (2010). <https://doi.org/10.1103/PhysRevC.81.055807>

208. A. Formicola et al., Astrophysical S-factor of  $^{14}\text{N}(p,\gamma)^{15}\text{O}$ . Phys. Lett. B **591**, 61–68 (2004). <https://doi.org/10.1016/j.physletb.2004.03.092>
209. I. Lombardo et al., Toward a reassessment of the  $^{19}\text{F}(p,\alpha)^{16}\text{O}$  reaction rate at astrophysical temperatures. Phys. Lett. B **748**, 178–182 (2015). <https://doi.org/10.1016/j.physletb.2015.06.073>
210. I. Indelicato et al., New improved indirect measurement of the  $^{19}\text{F}(p,\alpha)^{16}\text{O}$  reaction at energies of astrophysical relevance. Astrophys. J. **845**(1), 19 (2017). <https://doi.org/10.3847/1538-4357/aa7de7>
211. R.J. deBoer et al.,  $^{19}\text{F}(p,\gamma)^{20}\text{Ne}$  and  $^{19}\text{F}(p,\alpha)^{16}\text{O}$  reaction rates and their effect on calcium production in Population III stars from hot CNO breakout. Phys. Rev. C **103**, 055815 (2021). <https://doi.org/10.1103/PhysRevC.103.055815>
212. H. Herndl et al., Direct reaction analysis of  $^{19}\text{F}(p,\alpha)^{16}\text{O}$  below the Coulomb barrier. Phys. Rev. C **44**(3), 952–955 (1991). <https://doi.org/10.1103/PhysRevC.44.R952>
213. I. Lombardo et al., New analysis of  $p+^{19}\text{F}$  reactions at low energies and the spectroscopy of natural-parity states in  $^{20}\text{Ne}$ . Phys. Rev. C **100**, 044307 (2019). <https://doi.org/10.1103/PhysRevC.100.044307>
214. L.Y. Zhang et al., Direct measurement of the astrophysical  $^{19}\text{F}(p,\alpha\gamma)^{16}\text{O}$  reaction in the deepest operational underground laboratory. Phys. Rev. Lett. **127**(15), 152702 (2021). <https://doi.org/10.1103/PhysRevLett.127.152702>
215. L. Zhang et al., Measurement of  $^{19}\text{F}(p,\gamma)^{20}\text{Ne}$  reaction suggests CNO breakout in first stars. Nature **610**(7933), 656–660 (2022). <https://doi.org/10.1038/s41586-022-05230-x>
216. O. Clarkson, F. Herwig, Convective H-He interactions in massive population III stellar evolution models. Mon. Not. R. Astron. Soc. **500**(2), 2685–2703 (2021). <https://doi.org/10.1093/mnras/staa3328>
217. J.M. Cesaratto et al., Measurement of the  $E_r^{\text{c.m.}} = 138$  keV resonance in the  $^{23}\text{Na}(p,\gamma)^{24}\text{Mg}$  reaction and the abundance of sodium in AGB stars. Phys. Rev. C **88**(6), 065806 (2013). <https://doi.org/10.1103/PhysRevC.88.065806>
218. E. Carretta, A. Bragaglia, R. Gratton, S. Lucatello, Na-O anticorrelation and HB. VIII. Proton-capture elements and metallicities in 17 globular clusters from UVES spectra. Astron. Astrophys. **505**(1), 139–155 (2009). <https://doi.org/10.1051/0004-6361/200912097>
219. A. Slemer et al.,  $^{22}\text{Ne}$  and  $^{23}\text{Na}$  ejecta from intermediate-mass stars: the impact of the new LUNA rate for  $^{22}\text{Ne}(p,\gamma)^{23}\text{Na}$ . Mon. Not. R. Astron. Soc. **465**(4), 4817–4837 (2017). <https://doi.org/10.1093/mnras/stw3029>
220. F. D'Antona et al., A single model for the variety of multiple-population formation(s) in globular clusters: a temporal sequence. Mon. Not. R. Astron. Soc. **458**(2), 2122–2139 (2016). <https://doi.org/10.1093/mnras/stw387>
221. A. Renzini, Origin of multiple stellar populations in globular clusters and their helium enrichment. Mon. Not. R. Astron. Soc. **391**(1), 354–362 (2008). <https://doi.org/10.1111/j.1365-2966.2008.13892.x>
222. C. Iliadis et al., Proton-induced thermonuclear reaction rates for  $A = 20 - 40$  nuclei. Astrophys. J. Suppl. Ser. **134**(1), 151–171 (2001). <https://doi.org/10.1086/320364>
223. M. La Cognata et al., Exploring the astrophysical energy range of the  $^{27}\text{Al}(p,\alpha)^{24}\text{Mg}$  reaction: a new recommended reaction rate. Phys. Lett. B **826**, 136917 (2022). <https://doi.org/10.1016/j.physletb.2022.136917>
224. M. Assié et al., Characterization of light particles ( $Z \leq 2$ ) discrimination performances by pulse shape analysis techniques with high-granularity silicon detector. Eur. Phys. J. A **51**, 11 (2015). <https://doi.org/10.1140/epja/i2015-15011-6>
225. G. Hardie et al., Resonant alpha capture by  $^7\text{Be}$  and  $^7\text{Li}$ . Phys. Rev. C **29**, 1199–1206 (1984). <https://doi.org/10.1103/PhysRevC.29.1199>
226. A. Psaltis et al., Direct measurement of resonances in  $^7\text{Be}(\alpha,\gamma)^{11}\text{C}$  relevant to  $\nu p$ -process nucleosynthesis. Phys. Rev. Lett. **129**, 162701 (2022). <https://doi.org/10.1103/PhysRevLett.129.162701>
227. A. Psaltis et al., First inverse kinematics measurement of resonances in  $^7\text{Be}(\alpha,\gamma)^{11}\text{C}$  relevant to neutrino-driven wind nucleosynthesis using dragon. Phys. Rev. C **106**, 045805 (2022). <https://doi.org/10.1103/PhysRevC.106.045805>
228. Y. Xu et al., NACRE II: an update of the NACRE compilation of charged-particle-induced thermonuclear reaction rates for nuclei with mass number  $A < 16$ . Nucl. Phys. A **918**, 61–169 (2013). <https://doi.org/10.1016/j.nuclphysa.2013.09.007>
229. B. Vande Kolk et al., Investigation of the  $^{10}\text{B}(p,\alpha)^7\text{Be}$  reaction from 0.8 to 2.0 MeV. Phys. Rev. C **105**, 055802 (2022). <https://doi.org/10.1103/PhysRevC.105.055802>
230. E.M. Burbidge, G.R. Burbidge, W.A. Fowler, F. Hoyle, Synthesis of the elements in stars. Rev. Mod. Phys. **29**, 547–650 (1957). <https://doi.org/10.1103/RevModPhys.29.547>
231. R.J. Jaszczak, J.H. Gibbons, R.L. Macklin,  $^{12}\text{C}(\alpha,\gamma)^{16}\text{O}$  capture cross section below 3.2 MeV. Phys. Rev. C **2**, 63–69 (1970). <https://doi.org/10.1103/PhysRevC.2.63>
232. H. Makii et al., Measurement system of the  $\gamma$ -ray angular distributions of the reactions of the  $^{12}\text{C}(\alpha,\gamma)^{16}\text{O}$  reaction. Nucl. Instrum. Methods Phys. Res. A **547**(2–3), 411–423 (2005). <https://doi.org/10.1016/j.nima.2005.03.164>
233. H. Makii et al.,  $E1$  and  $E2$  cross sections of the  $^{12}\text{C}(\alpha,\gamma)^{16}\text{O}$  reaction using pulsed  $\alpha$  beams. Phys. Rev. C **80**, 065802 (2009). <https://doi.org/10.1103/PhysRevC.80.065802>
234. R. Plag et al.,  $^{12}\text{C}(\alpha,\gamma)^{16}\text{O}$  studied with the Karlsruhe  $4\pi$  BaF<sub>2</sub> detector. Phys. Rev. C **86**, 015805 (2012). <https://doi.org/10.1103/PhysRevC.86.015805>
235. P. Dyer, C.A. Barnes, The  $^{12}\text{C}(\alpha,\gamma)^{16}\text{O}$  reaction and stellar helium burning. Nucl. Phys. A **233**(2), 495–520 (1974). [https://doi.org/10.1016/0375-9474\(74\)90470-9](https://doi.org/10.1016/0375-9474(74)90470-9)
236. D. Schürmann, L. Gialanella, R. Kunz, F. Strieder, The astrophysical S factor of  $^{12}\text{C}(\alpha,\gamma)^{16}\text{O}$  at stellar energy. Phys. Lett. B **711**(1), 35–40 (2012). <https://doi.org/10.1016/j.physletb.2012.03.064>
237. R. Smith et al., Precision measurements on oxygen formation in stellar helium burning with gamma-ray beams and a Time Projection Chamber. Nat. Commun. **12**, 5920 (2021). <https://doi.org/10.1038/s41467-021-26179-x>
238. Y.P. Shen et al., Constraining the external capture to the  $^{16}\text{O}$  ground state and the  $E2S$  factor of the  $^{12}\text{C}(\alpha,\gamma)^{16}\text{O}$  reaction. Phys. Rev. Lett. **124**, 162701 (2020). <https://doi.org/10.1103/PhysRevLett.124.162701>
239. C. Iliadis, R. Longland, A.E. Champagne, A. Coc, R. Fitzgerald, Charged-particle thermonuclear reaction rates: II. Tables and graphs of reaction rates and probability density functions. Nucl. Phys. A **841**(1–4), 31–250 (2010). <https://doi.org/10.1016/j.nuclphysa.2010.04.009>
240. J. Görres et al., Low-energy resonances in  $^{14}\text{N}(\alpha,\gamma)^{18}\text{F}$  and their astrophysical implications. Phys. Rev. C **62**, 055801 (2000). <https://doi.org/10.1103/PhysRevC.62.055801>
241. F. de Oliveira et al., Determination of  $\alpha$ -widths in  $^{19}\text{F}$  relevant to fluorine nucleosynthesis. Nucl. Phys. A **597**(2), 231–252 (1996). [https://doi.org/10.1016/0375-9474\(95\)00455-6](https://doi.org/10.1016/0375-9474(95)00455-6)
242. A.C. Dombos et al., Measurement of low-energy resonance strengths in the  $^{18}\text{O}(\alpha,\gamma)^{22}\text{Ne}$  reaction. Phys. Rev. Lett. **128**, 162701 (2022). <https://doi.org/10.1103/PhysRevLett.128.162701>
243. A. Di Leva et al., Underground study of the  $^{17}\text{O}(p,\gamma)^{18}\text{F}$  reaction relevant for explosive hydrogen burning. Phys. Rev. C **89**, 015803 (2014). <https://doi.org/10.1103/PhysRevC.89.015803>

244. P. Adsley et al., Reevaluation of the  $^{22}\text{Ne}(\alpha, p)^{26}\text{Mg}$  and  $^{22}\text{Ne}(\alpha, n)^{25}\text{Mg}$  reaction rates. *Phys. Rev. C* **103**(1), 015805 (2021). <https://doi.org/10.1103/PhysRevC.103.015805>
245. M. Jaeger, R. Kunz, A. Mayer, J.W. Hammer, G. Staudt, K.L. Kratz, B. Pfeiffer,  $^{22}\text{Ne}(\alpha, n)^{25}\text{Mg}$ : the key neutron source in massive stars. *Phys. Rev. Lett.* **87**, 202501 (2001). <https://doi.org/10.1103/PhysRevLett.87.202501>
246. B. Gao et al., deep underground laboratory measurement of  $^{13}\text{C}(\alpha, n)^{16}\text{O}$  in the Gamow windows of the *s* and *i* processes. *Phys. Rev. Lett.* **129**, 132701 (2022). <https://doi.org/10.1103/PhysRevLett.129.132701>
247. G.F. Ciani et al., A new approach to monitor  $^{13}\text{C}$   $\alpha$ -targets degradation in situ for  $^{13}\text{C}(\alpha, n)^{16}\text{O}$  cross-section measurements at LUNA. *Eur. Phys. J. A* **56**(3), 75 (2020). <https://doi.org/10.1140/epja/s10050-020-00077-0>
248. M. Heil et al., The  $^{13}\text{C}(\alpha, n)$  reaction and its role as a neutron source for the *s* process. *Phys. Rev. C* **78**, 025803 (2008). <https://doi.org/10.1103/PhysRevC.78.025803>
249. S. Harissopoulos et al., Cross section of the  $^{13}\text{C}(\alpha, n)^{16}\text{O}$  reaction: a background for the measurement of geo-neutrinos. *Phys. Rev. C* **72**, 062801 (2005). <https://doi.org/10.1103/PhysRevC.72.062801>
250. R.J. deBoer et al., Sensitivity of the  $^{13}\text{C}(\alpha, n)^{16}\text{O}$  *S* factor to the uncertainty in the level parameters of the near-threshold state. *Phys. Rev. C* **101**, 045802 (2020). <https://doi.org/10.1103/PhysRevC.101.045802>
251. H.W. Becker, K.U. Kettner, C. Rolfs, H.P. Trautvetter, The  $^{12}\text{C} + ^{12}\text{C}$  reaction at subcoulomb energies (II)\*. *Z. Phys. A* **303**, 305–312 (1981). <https://doi.org/10.1007/BF01421528>
252. J. Zickefoose et al., Measurement of the  $^{12}\text{C} + ^{12}\text{C}, p)^{23}\text{Na}$  cross section near the Gamow energy. *Phys. Rev. C* **97**, 065806 (2018). <https://doi.org/10.1103/PhysRevC.97.065806>
253. J.T. Suhonen, Value of the axial-vector coupling strength in  $\beta$  and  $\beta\beta$  decays: a review. *Front. Phys.* (2017). <https://doi.org/10.3389/fphy.2017.00055>
254. P. Das, A. Ray, Terrestrial  $^7\text{Be}$  decay rate and  $^8\text{B}$  solar neutrino flux. *Phys. Rev. C* **71**, 025801 (2005). <https://doi.org/10.1103/PhysRevC.71.025801>
255. D. Vescovi et al., Effects of a revised  $^7\text{Be}$  *e*-capture rate on solar neutrino fluxes. *Astron. Astrophys.* **623**, 126 (2019). <https://doi.org/10.1051/0004-6361/201834993>
256. C. Santonastaso, Change in the  $^7\text{Be}$  half life in different environments. Master thesis, Università degli Studi di Salerno (2019)
257. C. Santonastaso et al., Change in the  $^7\text{Be}$  half-life in different environments. *Il Nuovo Cimento C* (2021). <https://doi.org/10.1393/ncc/i2021-21075-8>
258. G. D'Agata et al., The  $^{19}\text{F}(\alpha, p)^{22}\text{Ne}$  and  $^{23}\text{Na}(p, \alpha)^{20}\text{Ne}$  reaction in AGB nucleosynthesis via THM. *Eur. Phys. J. Web Conf.* **184**, 02003 (2018). <https://doi.org/10.1051/epjconf/2018184h02003>
259. M. La Cognata et al., On the measurement of the  $^{13}\text{C}(\alpha, n)^{16}\text{O}$  *S*-factor at negative energies and its influence on the *s*-process. *Astrophys. J.* **777**, 143 (2013). <https://doi.org/10.1088/0004-637X/777/2/143>
260. O. Trippella, M. La Cognata, Concurrent application of ANC and THM to assess the  $^{13}\text{C}(\alpha, n)^{16}\text{O}$  absolute cross section at astrophysical energies and possible consequences for neutron production in low-mass AGB stars. *Astrophys. J.* **837**, 41 (2017). <https://doi.org/10.3847/1538-4357/aa5eb5>
261. M. Freer, H.O.U. Fynbo, The Hoyle state in  $^{12}\text{C}$ . *Prog. Part. Nucl. Phys.* **78**, 1–23 (2014). <https://doi.org/10.1016/j.pnpnp.2014.06.001>
262. H.-B. Mak et al., Radiative decay of the second excited state of  $^{12}\text{C}$ . *Phys. Rev. C* **12**(4), 1158–1166 (1975). <https://doi.org/10.1103/PhysRevC.12.1158>
263. W.M. White, *Isotope Geochemistry* (John Wiley & Sons, Hoboken, 2023)
264. S. Becker, *Inorganic Mass Spectrometry* (John Wiley & Sons, Hoboken, 2008)
265. A. Wallner et al., Potential of AMS for quantifying long-lived reaction products, in *AIP Conference Proceedings*, vol. 769 (2005), pp. 621–624. <https://doi.org/10.1063/1.1945086>
266. W. Kutschera, Progress in isotope analysis at ultra-trace level by AMS. *Int. J. Mass Spectrom.* **242**(2), 145–160 (2005). <https://doi.org/10.1016/j.ijms.2004.10.029>
267. R.A. Muller, Radioisotope dating with a cyclotron. *Science* **196**(4289), 489–494 (1977). <https://doi.org/10.1126/science.196.4289.489>
268. K.H. Purser et al., An attempt to detect stable N<sup>-</sup> ions from a sputter ion source and some implications of the results for the design of tandems for ultra-sensitive carbon analysis. *Rev. Phys. Appl.* **12**(10), 1487–1492 (1977). <https://doi.org/10.1051/rphysap:0197700120100148700>
269. S.H. Sie, D.A. Sims, G.F. Suter, T.R. Niklaus, A fast bouncing system for the high-energy end of AMS. *Nucl. Instrum. Methods Phys. Res. B* **172**(1), 268–273 (2000). [https://doi.org/10.1016/S0168-583X\(00\)00126-9](https://doi.org/10.1016/S0168-583X(00)00126-9)
270. F. Marzaioli et al., Forensic applications of  $^{14}\text{C}$  at CIRCE. *Nucl. Instrum. Methods Phys. Res. B* **269**(24), 3171–3175 (2011). <https://doi.org/10.1016/j.nimb.2011.04.025>
271. D.M. Fernandes et al., A genetic history of the pre-contact Caribbean. *Nature* **590**(7844), 103–110 (2021). <https://doi.org/10.1038/s41586-020-03053-2>
272. F. Marzaioli et al., Mortar radiocarbon dating: preliminary accuracy evaluation of a novel methodology. *Anal. Chem.* **83**(6), 2038–2045 (2011). <https://doi.org/10.1021/ac1027462>
273. G. Ricci et al., Integrated multi-analytical screening approach for reliable radiocarbon dating of ancient mortars. *Sci. Rep.* **12**(1), 3339 (2022). <https://doi.org/10.1038/s41598-022-07406-x>
274. A. Petraglia et al., Ultrasensitive radionuclide analysis in water and sediments for environmental radiological assessment near the decommissioning Garigliano Nuclear Power Plant (Italy). *Appl. Sci.* (2022). <https://doi.org/10.3390/app12168033>
275. R. Buompane et al., Isotopic techniques for environmental monitoring and nuclear waste management at CIRCE. *Il Nuovo Cimento C* (2023). <https://doi.org/10.1393/ncc/i2023-23049-2>
276. F. Miyake, K. Masuda, T. Nakamura, Another rapid event in the carbon-14 content of tree rings. *Nat. Commun.* **4**(1), 1748 (2013). <https://doi.org/10.1038/ncomms2783>
277. F. Miyake, K. Nagaya, K. Masuda, T. Nakamura, A signature of cosmic-ray increase in ad 774–775 from tree rings in Japan. *Nature* **486**(7402), 240–242 (2012). <https://doi.org/10.1038/nature11123>
278. J. Uusitalo et al., Solar superstorm of AD 774 recorded subannually by Arctic tree rings. *Nat. Commun.* **9**(1), 3495 (2018). <https://doi.org/10.1038/s41467-018-05883-1>
279. F. Terrasi et al., Can the  $^{14}\text{C}$  production in 1055 CE be affected by SN1054? *Radiocarbon* **62**(5), 1403–1418 (2020). <https://doi.org/10.1017/RDC.2020.58>
280. X. Wang et al., *r*-process radioisotopes from near-Earth supernovae and kilonovae. *Astrophys. J.* **923**(2), 219 (2021). <https://doi.org/10.3847/1538-4357/ac2d90>
281. B.N. Limata et al., New experimental study of low-energy ( $p, \gamma$ ) resonances in magnesium isotopes. *Phys. Rev. C* **82**(1), 015801 (2010). <https://doi.org/10.1103/PhysRevC.82.015801>
282. Z. Solti, J. Magill, R. Dreher, Karlsruhe Nuclide Chart—new 10th edition 2018. *Eur. Phys. J. Nucl. Sci. Technol.* **5**, 6 (2019). <https://doi.org/10.1051/epjn/2019004>

283. E.G. Johnson, A.O. Nier, Angular aberrations in sector shaped electromagnetic lenses for focusing beams of charged particles. *Phys. Rev.* **91**, 10–17 (1953). <https://doi.org/10.1103/PhysRev.91.10>
284. L. Ricci et al., The achievements of the RockStar Group (Perugia) on astrophysical modelling and Pallasite geochemistry. *Universe* (2022). <https://doi.org/10.3390/universe8030156>
285. A. Zucchini et al., Chemical and mineralogical characterization of the Mineo (Sicily, Italy) pallasite: a unique sample. *Meteorit. Planet. Sci.* **53**(2), 268–283 (2018). <https://doi.org/10.1111/maps.13002>
286. E. Mugnaioli et al., 3D electron diffraction study of terrestrial iron oxide alteration in the Mineo pallasite. *Mineral. Mag.* **86**(2), 272–281 (2022). <https://doi.org/10.1180/mgm.2022.20>
287. M. De Cesare, A. Di Leva, A. Del Vecchio, L. Gialanella, A novel recession rate physics methodology for space applications at CIRA by means of CIRCE radioactive beam tracers. *J. Phys. D Appl. Phys.* **51**(9), 09–01 (2018). <https://doi.org/10.1088/1361-6463/aaa834>
288. M. De Cesare et al., Gamma and infrared novel methodologies in aerospace re-entry:  $\gamma$ -rays crystal efficiency by GEANT4 for TPS material recession assessment and simultaneous dual color infrared temperature determination. *Nucl. Instrum. Methods Phys. Res. B* **479**, 264–271 (2020). <https://doi.org/10.1016/j.nimb.2020.02.005>
289. D. Rapagnani et al., Validation of a novel technique with radioactive implanted ions for recession rate estimate of aerospace material. *J. Phys. D Appl. Phys.* **54**, 32 (2021). <https://doi.org/10.1088/1361-6463/ac006e>
290. D. Rapagnani et al., Ion beam analysis for recession determination and composition estimate of aerospace thermal protection system materials. *Nucl. Instrum. Methods Phys. Res. B* **467**, 53–57 (2020). <https://doi.org/10.1016/j.nimb.2020.01.006>
291. H.J. Assenbaum, K. Langanke, C. Rolfs, Effects of electron screening on low-energy fusion cross sections. *Z. Phys. A* **327**(4), 461–468 (1987). <https://doi.org/10.1007/BF01289572>
292. D. Rapagnani et al., Feasibility study of a compact and multi-gas supersonic plasma jet for nuclear astrophysics and space research. *Nucl. Instrum. Methods Phys. Res. A* **1056**, 168536 (2023). <https://doi.org/10.1016/j.nima.2023.168536>
293. L.C. Feldman, J.W. Mayer, S.T. Picraux, *Materials Analysis by Ion Channeling: Submicron Crystallography* (Academic Press, San Diego, 2012)
294. <https://www.km3net.org>